Design of Continuum Robots, Sensing Modalities, and Situational Awareness Aids with Applications to Surgery and Manufacturing

By

Colette Patricia Abah

Dissertation

Submitted to the Faculty of the

Graduate School of Vanderbilt University

in partial fulfillment of the requirements

for the degree of

DOCTOR OF PHILOSOPHY

in

Mechanical Engineering

January 31, 2022

Nashville, Tennessee

Approved:

Nabil Simaan, Ph.D.

Rohan Chitale, M.D.

Jack Noble, Ph.D.

Eric Barth, Ph.D.

Michael Goldfarb, Ph.D.

ACKNOWLEDGMENTS

Every graduate student knows or eventually finds out that the choice of an academic advisor is the most important decision we make in the Ph.D. journey. As my graduate school journey comes to an end, I feel very fortunate for to have been advised by Dr. Nabil Simaan. Nabil is dedicated to the growth of every student who steps foot in his lab, from high school interns to graduate research assistants. I have grown tremendously over the last 5.5 years, both as a person and as a professional, and I owe this transformation to Nabil's mentorship. Nabil, thank you for everything you have taught me, from technical skills to core values. Your commitment to research integrity and constant push towards excellence are two of your qualities I admire the most, and which I aim to emulate in my career.

I thank Dr. Chitale for being my clinical mentor and providing much needed insight about the clinical impact of our research. Thank you for unlimited access to the operating room, and for your patience during all our experiments. Shadowing you and witnessing different neuro-surgery cases was one of the highlights of my graduate experience.

Dr. Noble, Dr. Goldfarb, and Dr. Barth, thank you for contributing to my training through the classes you taught and thank you for serving on my dissertation committee. This dissertation would not have been possible without the generous funding from the National Institute of Health - NIH (NIBIB-T32EB021937) and the National Science Foundation - NSF (NRI CMMI-1734461 and NRI IIS-1327566). I am thankful to the Vanderbilt Institute for Surgery and Engineering (VISE) for my training fellowship, and the fellowship that sponsored some Dr. Chitale's time to work with us on Chapters 4 and 5.

I thank my ARMA labmates: Long Wang, Nima Sarli, Rashid Yasin, Giuseppe Del Giudice, Andrew Orekhov, Garrison Johnston, Neel Shihora, Elan Ahronovich, and Jared Lawson. I cannot think of a better group of people to be in the "trenches" with. You guys have been amazing research collaborators and even better friends to me over the years. I will always cherish all the memories we shared, from the coffee breaks and lab lunches, to road trips and deep conversations. One day, I might even look fondly on the late nights spent stressing out about upcoming deadlines... one day.

I thank my support system in Nashville. My roommate Ela Joshi became one of my closest friends in Nashville. Thank you for all the "life" conversations and the laughter we shared in 4141 Woodlawn Drive. Katy Riojas, I am so thankful that ICRA 2018 (Australia yay!) jump-started our friendship. Thank you for all our adventures and for all the care packages you spoil me with. I also thank the "Women of VISE", especially the writers' group: Roza Bayrak, Nhung Hoang, Haley Adams, and Neda Sardaripour. Getting to know you ladies has been the highlight of my last year at Vanderbilt. Thank you for all the fun camaraderie!

I am thankful for the many friends (my MIT crew, my UWC crew, and my JT crew) who provided a much needed escape from Nashville. In particular, Sheila Namirembe and Christine Ajinjeru understand my singular journey better than anyone. I thank them for walking along side me and reassuring me at every step of the way!

Finally, I thank my family (papa, maman, Alain et Divine) for their love and support. I appreciate the many sacrifices that contributed to getting me here. In particular, I thank my dad who has always been my biggest supporter in everything, especially the academic pursuit. Whenever I told him I was anxious/scared that I might miss a deadline or fail an exam, he replied: "Je te fais confiance. Tout va tres bien se passer!" His unwavering confidence in my ability to achieve anything and everything has been a beacon of light at every step of this journey.

TABLE OF CONTENTS

LIST OF TABLES

LIST OF FIGURES

CHAPTER 1
INTRODUCTION

1.1 Dissertation Overview

Conventional rigid-link robots have become ubiquitous in many industries, including manufacturing [4, 5], defense [6], space exploration [7], and medicine [8, 9]. These robots have expanded and, in some cases, surpassed human capabilities in terms precision, repeatability, and endurance. However, for applications that require navigation of complex curvilinear pathways, deep reach within a confined space, and/or interaction with human anatomy in close quarters, rigid-link robots are not ideal due to safety considerations and their limited robustness to geometric uncertainty of the environment.

Continuum robots are a newer class of robots that mimic soft biological actuators (e.g. snakes, elephant trunk, octopus limbs) [10] and are able to meet the aforementioned functional requirements. Thanks to their distal actuation and high dexterity, continuum robots are able to perform navigation and manipulation tasks that are impossible or too complex for conventional robots [11]. In addition, their inherent structural compliance allows for safe interactions with humans in the context of surgical robotics [12, 13] and human-robot interactions [14, 11].

Figure 1.1 presents an overview of the research areas covered in this dissertation. In this dissertation, we explore the use of continuum robots in two applications: "*in situ collaborative manufacturing*" and "*neuro-endovascular surgery*". These applications span a wide range of size requirements from the macro scale (meters) to the small (millimetric or sub-millimetric) scale and share the need for continuum robots augmented with robot perception, situational awareness, and adaptable behaviors.

Industrial workers often perform manufacturing, assembly, and maintenance tasks in

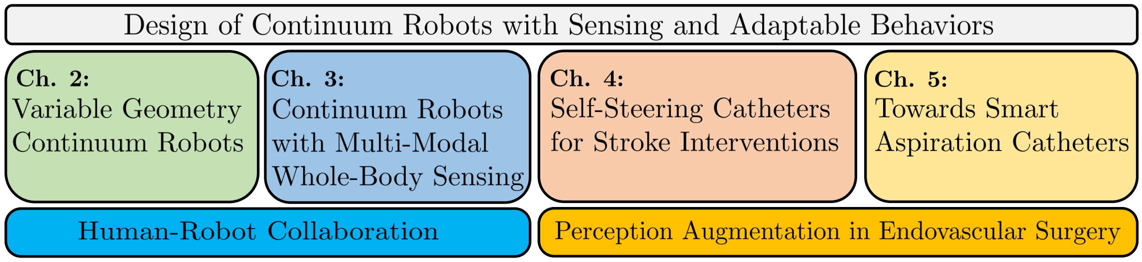

Figure 1.1: Overview of the research areas covered in this dissertation.

confined spaces, putting them at risk for work-related musculoskeletal disorders due to sustained non-ergonomic postures [15]. The deployment of continuum robots in confined spaces for collaborative manufacturing (with a co-located human) can alleviate the physiological burden on workers. This application demands levels of dexterity, sensing, and safety that exceed the capabilities of existing robotic systems.

To address these limitations, our research efforts focus on the design and evaluation of *in-situ collaborative robots* (ISCRs). Our research for enabling safe human-robot collaboration is shown in the left side of Fig. 1.1. We address the associated sensing and robot situational awareness challenges, with two approaches for distributive sensing along the length of continuum robots. In chapter 2, we present a variable diameter continuum robot that utilizes its kinematic redundancy for task-dependent geometric adaptation. In Chapter 3, we present a continuum robot with integrated multi-modal whole-body sensing capabilities, including contact detection, contact localization, force sensing, proximity sensing, and mapping.

The right side of Fig. 1.1 depicts the research focus areas for enabling perception augmentation for endoluminal and endovascular surgery. These research focus areas comprise the second half of this dissertation aiming at addressing navigation and situational awareness challenges in neuro-endovascular surgery.

Standard neuro-endovascular procedures require surgeons to navigate from the femoral artery, select the appropriate branch of the aortic arch, and traverse the tortuous carotid syphon in order to reach the target vasculature in the brain. Currently, this complex navigation is performed with concentrically stacked passive guidewires and passive catheters. Reaching the target vasculature can take several trials and errors, even for experienced neuro-interventionalists, which can negatively impact the outcome of time-sensitive interventions (e.g. clot retrieval for stroke care, coil embolization of aneurysms). Furthermore, the lack of distal control of catheter increases the technical complexity and cognitive load required to perform these surgeries. As a result, only dedicated stroke centers in large metropolitan areas are equipped to perform these surgeries. For time-sensitive diseases such as ischemic stroke, the need for interhospital transfers (from local hospital to stroke center) results in delayed endovascular treatment and increased risk of disability or death [16]. There is a need for actively steerable catheters that are capable of semi-automated navigation and branch selection in narrow and tortuous vasculature [17], but most current steerable catheters are not suitable for neuronavigation due to their size and design parameters.

To address this challenge, we present in Chapter 4, a novel multi-articulated robotic catheter that integrates preoperative path planning, intraoperative image-based pose tracking, and active compliance for self-steering. We also propose a multi-mode controller for intuitive switching between passive compliance, active compliance, and user-guided navigation modes.

In addition to the navigation challenges, neuro-interventionalists are hampered by the limited sensory awareness of the microcatheters as they move through small, fragile, mobile vessels. While navigating a long (more than 1 meter) catheter, they lack haptic feedback and this critical situational awareness barrier is further compounded by the lack of quality visualization of the catheter tip relative to vascular anatomy and the lack of perception regarding catheter tip interaction with clots and aneurysms. These perception deficits increase cognitive burden and diminish patient outcome.

To address this need, we investigate a novel concept for intraoperative sensing during endovascular procedures. The proposed technology uses an indirect approach to provide two unprecedented capabilities: 1) estimate the distance between the catheter tip and a blood clot, 2) inform the surgeon about the quality of the engagement of the catheter tip with a blood clot. The proposed technology has the potential to offer a low-cost rapidly deployable sensory solution, which is compatible with existing catheter technology.

1.2 Motivation, Technical Gaps, and Contributions

The next section expands on the motivating technical and/or clinical needs for continuum robots with (1) situational awareness and (2) adaptable behaviors in collaborative manufacturing and neuro-endovascular surgery applications. We also highlight the contributions of this doctoral work relative to prior art.

1.2.1 Situational Awareness and Adaptable Behaviors for Human-Robot Collaboration

Work related musculoskeletal disorders (WMSDs) can result from the handling of heavy loads or the repetitive handling of light-weight objects [15]. The risk of WMSDs is further exacerbated when industrial workers operate in non-ergonomic positions, as is the case for confined space applications (e.g. the wing of an airplane, house-hold crawl spaces, pipes) as illustrated in Fig. 1.2(a). Robotic assistance can alleviate this burden with one or a combination of these three control approaches: a) full autonomy, b) telemanipulation or ex-situ collaboration, and c) in-situ human-robot collaboration. Full autonomy requires precise knowledge of the environment and reduces the repertoire available tasks to simple, pre-planned tasks. Telemanipulation enables the user to control the robot from outside the confine space, but may not be suitable for applications that require complex manipulation tasks or human sensory presence for quality control. In-situ human-robot collaboration, on the other hand, provides robotic assistance for load-bearing, while keeping the human on site to perform complex or manual customizations. Fig. 1.2(b) illustrates in-situ human-robot collaboration.

Multi-backbone continuum robots (MBCRs) [18] are well suited for deep reach within

(a) (b)

Figure 1.2: (a) Examples of industrial workers in confined spaces. (b) Concept of in-situ collaborative robots (ISCR) for robotic assistance in confined spaces

confined spaces with a co-located human, thanks to their distal actuation and inherent compliance (passive safety). For increased safety, these robots must be augmented with the ability to map their environment, sense neighboring objects, detect and localize contact along their lengths, and adapt their behaviors accordingly.

Works on continuum robot with adaptable geometry have mostly focused on backbone extensibility using magnetized disks [19] and springs [20] as to update the separation between the disks of the continuum robots. Backbone extensibility has also been considered in pneumatic bellows [21, 22] and McKibben actuators [23]. Variable diameter designs have not previously been considered in the context of multi-backbone continuum robots. Allowing the diameter of a MCBRs to vary adds an additional degree of freedom, that can be used to optimize dexterity or payload for a given task. This kinematic redundancy can also be utilized for contact detection along the length of the robot.

The literature on sensing methods for continuum robots is extensive. Most works have focused on estimation of the wrench at the end effector by measuring load on actuation lines [24], measuring deflection from equilibrium position [25, 26, 27], or using helical Fiber Bragg Gratings sensors [28]. Bajo et al. [29] investigated kinematics-based contact detection and localization along a multi-segment MBCR. External wrenches can be detected and localized when occurring on separate segments, but multiple contacts along a single segment can be detected but not localized. Chen et al. [30] also expanded and adapted this kinematics-based approach and demonstrated its efficacy for contact detection when using pneumatic bending bellow actuators. The proposed application requires contact detection and localization along the full body of the robot, as well as additional sensing modalities such as proximity sensing.

Multi-modal robotic skins have been explored in the context of rigid link robots [31, 32, 33] and soft robots [34, 35, 35] and have included various combinations of proximity sensing, contact detection, and normal force sensing. However, the integration of multi-modal sensing within the structure of a MBCR has not been considered. We build on these works and add additional sensing modalities to imbue continuum robots with whole body sensing and mapping capabilities.

This thesis proposed the following contributions for safe human-robot collaboration:

1) Variable Diameter Continuum Robots: We present the design and kinematic analysis of continuum robots with the ability to actively control their diameter to adapt their performance to a given tasks or to external stimuli.

2) Continuum disks with multi-modal sensing: We present the design, characterization, and evaluation of multi-modal sensing modules integrated within the structure of a multi-backbone continuum robots. These modules endow continuum robots with proximity sensing, mapping, contact detection and localization, and force sensing.

1.2.2 Navigation and Situational Awareness Challenges in Neuro-endovascular Surgery

In the United States, someone has a stroke every 40 seconds and someone dies from a stroke every 4 minutes [36]. Of all strokes, 87% are ischemic (caused by a blood clot), and 10% of all ischemic strokes are caused by large vessel occlusions (LVO), i.e. the blockage of the intracranial internal carotid artery (ICA) or the proximal middle cerebral artery (MCA). Although relatively low in percentage, strokes caused by LVO have a disproportionately high burden: 80% of LVO stroke patients suffer death or functional disability [37]. There are currently two main treatment options for the management of patients with acute ischemic stroke: intravenous thrombolysis (with r-tPA) and mechanical thrombectomy. Mechanical thrombectomy (MT) is the endovascular retrieval of blood clots using stent retrievers and/or aspiration catheters. This therapy was recently added to the AHA guidelines for treatment of acute stroke, after a series of randomized multicenter clinical trials (in 2015) demonstrated that LVO stroke patients achieve superior clinical outcome when treated with MT, compared to r-tPA alone [38, 39, 40, 41, 42, 43]. Patients treated with MT achieved revascularization rates up to 88% and had reduced disability rates at 90 days (Rankin score improved by up to 50%). Furthermore, MT eliminates the high risk of symptomatic intracerebral hemorrhage associated with the use of r-tPA.

The rise in awareness of the importance of MT stands in contrast to the availability of this type of intervention in large portions of the U.S. geography. The standard MT procedure involves navigating and steering through a long, thin, tortuous, and branched vascular network, using stacked passive (no distal control) guidewires and catheters. Due to the complexity of this procedure, only expert neuro-interventionalists at large trauma centers are currently capable of performing MT. Even for these experts, manual navigation and steering can take several attempts. Unfortunately, the United States has a shortage of neurologists in general, and neuro-interventionalists in particular [44]. Thus, upon diagnosis, patients with LVO strokes are either transferred from local hospitals to larger trauma centers with neuro-interventionalists or treated with the less effective intravenous thrombolysis. Interhospital transfers are associated with significant increases in ischemic time (additional 100 minutes on average [16, 45, 46]), and thus results in significantly lower patient outcome (increases risks of permanent brain damage, disability, death).

There is a need for dexterous and actively steerable microcatheters for assisted neuro-endovascular navigation [17]. Such technology has the potential to increase the speed of neuronavigation by reducing the trials and errors associated with manual navigation. In addition, smart assistive catheters can lower the MT skill barrier and expand the workforce available to perform these procedures, thus reducing the need for interhospital transfers.

In the past two decades, the use of steerable catheters and robotic assistance for endovascular navigation and vascular surgery has gathered significant research interest, especially in the fields of cardiac electrophysiology [47, 48, 49, 50, 51] and lung biopsy (e.g. Monarch Platform, Auris Health). Most commercially available robotic catheter systems have been FDA approved for cardiology and peripheral vasculature (e.g. Niobe from Stereotaxis [52], Sensei [53] and Magellan [54] from Hansen Medical, Amigo from Catheter Precision [55], Corpath from Corindus [56]), and do not meet the size and articulation requirements for navigating to common site of LVO (ICA and MCA). Bendit (Bendit Technologies) and SwiffNinja (Merit Medical [57]) are system that meet the size constraints for neuronavigation, but are not suited for neurovascular navigation because they have a single planar degree of articulation.

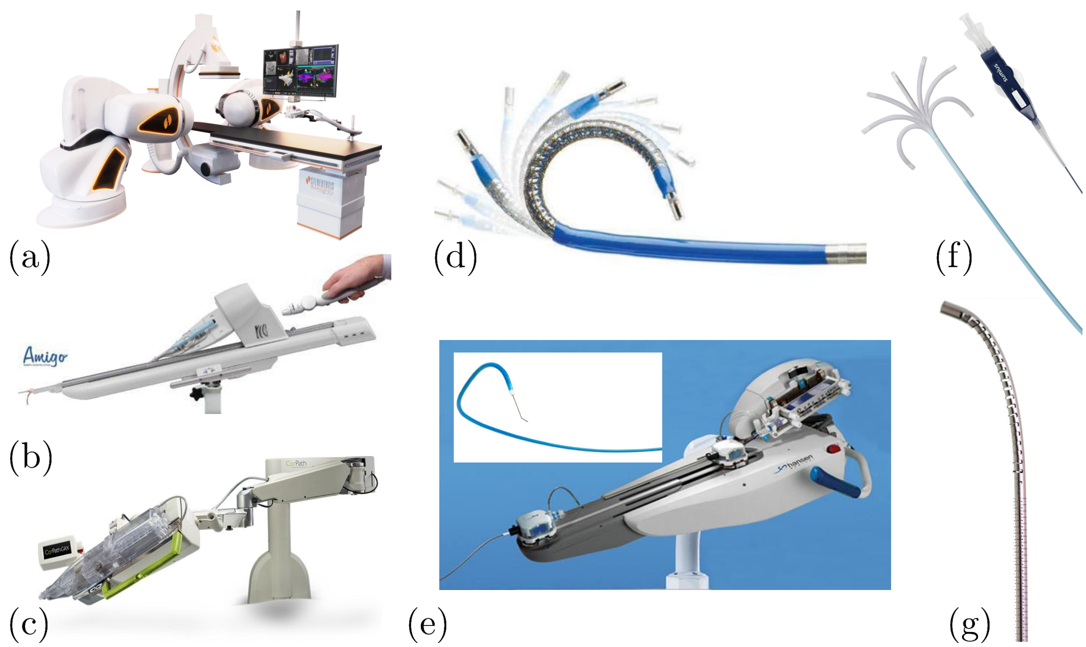

Figure 1.3: Commercially available catheters: (a) Niobe - Stereotaxis, (b) Amigo - Catheter Precision, (c) Corpath - Corindus, (d) Sensei Hansen Medical, (e) Magellan - Hansen Medical, (f) SwitfNinja - Merit Medical, (g) Bendit - Bendit Technologies

In addition to commercial devices, a few steerable catheter prototypes have emerged from research labs [58, 59, 60, 61, 62, 63, 64, 65, 66, 67], but to the best of our knowledge, none of these systems meet the simultaneous requirements of small outer diameter (≤ 2 mm [68]) and sufficient degrees of articulation (≥ 2 DOFs), while maintaining an open bore for clot aspiration or stent retriever deployment.

In addition to navigation challenges, surgeons lack sensory feedback about interaction forces at the tip of the catheter. The force sensed by their hands as they advance the catheter is largely masked by cumulative friction over the catheter's course. This challenge leads to intentional design of flimsy passive guidewires and micro-catheters, which can suffer from large torsional windup, making their navigation difficult. Sensing of catheter tip forces has received extensive attention in the literature [27, 69, 70, 71, 72, 73, 74, 75] and point force sensing exists commercially for larger cardiac catheters (e.g. [71, 73]). However, no sensing solutions currently can be used at the scale needed for MT. Ultrasonic sensing for flow velocimetry has been developed and explored for the past two decades [76]. The presence of the ultrasonic piezoelectric elements at the catheter tip prevents miniaturization while retaining a hollow and flexible tip. Such catheters have been used for cardiac applications [77][78]. Miniature IVUS ablation and imaging catheters (e.g. Boston Scientific's Ultra-ICETM) lack the necessary tip flexibility and a working bore. Furthermore, active compliance control of continuum robots has been sparsely addressed for larger designs (e.g. [79]) and no commercial or research systems have demonstrated active compliance of miniature intravascular catheters.

The speed and extent of recanalization are the strongest predictors of good clinical outcome after ischemic stroke treatment. Each 10 minutes of ischemic time correlates with 40 additional patient disability days and $10,000 increase in economic burden [80]. Complete revascularization from a single thrombectomy device pass, known as the "first pass effect", has been associated with significantly higher rates of good clinical outcome [81]. With current techniques, first pass clot retrieval is achieved only in 25% of cases [81]. These inefficiencies are partly linked to sensory deficiencies hampering the surgeons' perception. The two key perception barriers are 1) lack of real-time simultaneous visualization of clot location and catheter tip, and 2) lack of sensory feedback about the quality of clot engagement with the catheter tip. Surgeons currently rely on subjective measures (e.g. lack of blood return in the aspiration catheter [82]) to guess when they can attempt pulling the aspiration catheter. In the case of pre-mature catheter retrieval, the full process of endovascular navigation, x-ray imaging, and aspiration has to be repeated. Studies have shown that repeated passes with thrombectomy devices significantly reduce the likelihood of a good functional outcome for the patients [83]. As previously mentioned, none of the catheters or prior works address sensing at the scale needed for neurointervention while preserving a working bore and a very flexible tip as required for safe intracranial navigation. The most relevant work in the literature is [84], which investigated the force applied on the catheter tip as a function of clot proximity using computational fluid mechanics. We build on the reported results and propose a stochastic model based on experimental data in order to relate measured vacuum to proximity for a known flow rate.

In light of these clinical needs and technical gaps, this thesis proposes the following contributions for neuro-endovascular surgery:

3) <u>A multi-articulated, actively steerable catheter system</u>: We present the design, fabrication, and kinematic modelling of steerable microcatheter that meets the size and articulation requirements for neuro-endovascular navigation, while maintaining an open bore for suction or stent deployment. A custom 4-DoF actuation unit was designed with series-elastic elements to allow for fault-tolerance, increase safety, and enable force sensing at the catheter tip.

4) <u>Self-steering for intelligent neuronavigation</u>: We propose the use of preoperative CT scan of the target vasculature to create a nominal path plan, by optimizing the catheter shape to match the local section of vasculature. We also present a method for intra-operative catheter pose tracking and filtering from bi-plane fluoroscopy images.

5) <u>Catheter Parameter Optimization for Patient-Specific Interventions</u>: We present an approach for electing the optimal catheter design parameters to navigate a given vasculature anatomy with minimal shape deviations.

6) <u>Multi-mode assistive control and user interface</u>: We implemented and experimentally validated a multi-mode controller for real-time control of the robotic catheter. We also designed graphic user interfaces to enable the user to interface with the system intuitively.

7) <u>Clot proximity and engagement metrics</u>: We present a preliminary exploration the effect of pulsatile pressure excitation on catheter-clot proximity and engagement. We present a custom apparatus that replicates the setup for aspiration thrombectomy (with mock phantom vasculature and thrombus models) and integrates pressure and distance sensing modalities. The results obtain through this preliminary work suggest that there may be a path forward but more work is needed to establish the expected accuracy of this approach.

CHAPTER 2
VARIABLE GEOMETRY CONTINUUM ROBOTS

This chapter is adapted from "Design Considerations and Redundancy Resolution for Variable Geometry Continuum Robots" published in "2018 IEEE International Conference on Robotics and Automation (ICRA)" and has been reproduced with the permission of the publisher and my co-authors Andrew Orekhov and Nabil Simaan © 2018 IEEE.

2.1 Introduction

Continuum robots have been and are still being explored for potential use in many applications, including surgical robotics [85, 86, 87], field robotics [88] and manufacturing [22]. Multi-backbone continuum robots (MBCRs) are a subset of continuum robots, which were introduced in [18] as a design variation over wire-actuated single backbone designs from Gravagne and Walker [89]. In lieu of a wire-actuated single backbone, a MBCR uses several push-pull backbones both as load-bearing structural elements and as actuation lines. The design presented in [18] can be configured as non-extensible or extensible (e.g. [19]) by simply allowing all backbones to extend and having a means for maintaining separation between disk elements to keep all the backbones at a fixed radial distance from each other. In [19] such separation was achieved using the repelling forces between magnetized disks, while in [20], springs were used between the disks of a single-backbone wire-actuated design. Other non-MBCR designs offering backbone extensibility include pneumatic bellows [21, 22] and McKibben muscles [23].

Allowing the diameter of a continuum robot to vary is potentially advantageous in terms of workspace and the ability to use kinematic redundancy to optimize dexterity. In [90], active diameter control is utilized to vary the bending radius and stiffness of a non-MBCR continuum robot. Still, there is a need to explore the ability of a MBCR to adapt its kinematic dexterity and load-bearing capabilities to optimize its performance for a set of tasks or for a given workspace.

To address this need, this chapter highlights a preliminary design exploration of continuum robots with the ability to control their diameter. A design using the angulated scissor linkage (ASL) as a means for controlling the diameter of the continuum robot is presented and analyzed. An exploration of the design space for continuum robot segments having adjustable diameter disks is coupled to an exploration of possible design parameters for the circular scissor mechanism. Finally, a simplified statics model for variable diameter continuum robots is presented. The kinematic coupling between the diameter change and the joint-level kinematics is derived. A redundancy resolution scheme that aims to reduce the load on the secondary backbones while maximizing the workspace is presented as a simulation case study.

2.2 Design Concept of Variable Diameter Continuum Robots

Figure 2.1 shows the conceptual design of a variable diameter MBCR. The design includes multiple serially stacked segments, but for clarity, the figure shows only a single segment. Four backbones are circumferentially equidistantly distributed and the distance between them is controlled by several spacer disks. These spacer disks control their diameter by using an angulated scissor mechanism as shown in Fig. 2.1(a). The distal spacer disk (called the end disk) is fixed to the backbones, while all other spacer disks allow the backbones to slide through holes in their hinges. The distance between the disks is maintained through the use of compression springs wrapped around the backbones. Linear actuators are attached to the base spacer disk through a mechanical coupling not shown in the figure. These actuators control the length of the backbones and move radially when the spacer disks expand. By pulling and pushing on these backbones in a synchronous manner, the continuum segment may be bent in two controllable degrees of freedom.

The angulated scissor mechanism can be actuated by passing a wire loop within the walls of the scissor mechanism. Referring to Fig. 2.1(a), the wire loop passes over small pulleys connected at the outer circumference points **b** and loops back over similar pulleys on the inner circumference points **a**[1]. By shortening this loop, points a-b are pulled together, causing the diameter to expand. When the wire loop is released, the diameter of the disk shrinks due to circumferential springs attached as shown in Fig. 2.1(a).

The angulated scissor mechanism has been described in [91] where a review of its potential architectural applications and basic position analysis were presented. When choosing the design concept, we chose the angulated scissor mechanism because of several advantages over other design alternatives resulting in a variable diameter. The key advantage of this design compared to other designs (e.g. [92], [93, 94]) is that it allows a large working channel within the structure of the continuum robot and achieves radial expansion without additional torsion to the backbones.

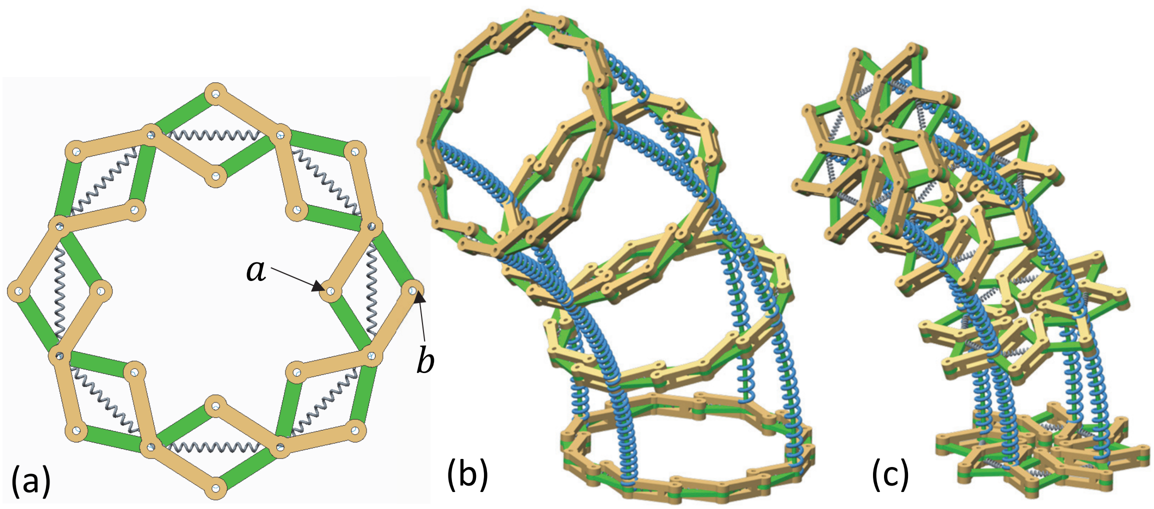

Figure 2.1: A variable diameter MBCR: (a) Angulated scissor mechanism showing the actuation points **a** and **b**, (b, c) A single segment MBCR at two diameter extremes.

2.3 Position Analysis of the Circular Angulated Scissor Linkage

To inform the design of a variable diameter MBCR, the kinematic analysis of the ASL is formulated. Table 2.1 and Fig. 2.2 present the key nomenclature used in this

[1]Though points **a** and **b** are shown at only one disk, the assumption is that all disks are identical and equipped with similar pulleys - hence the reference to circumference points.

analysis. Following the categorization in Table 2.1, the vertices of an ASL can be grouped into: innermost hinges (placed at radius a), middle-radius hinges (placed at radius r), and outermost hinges (placed at radius b). Furthermore, for the purposes of facilitating the analysis, Table 2.2 presents the independent (input) and dependent (output) variables of the ASL. The hinges associated with these radii will be henceforth referred to as points **a**, **r** and **b**, respectively.

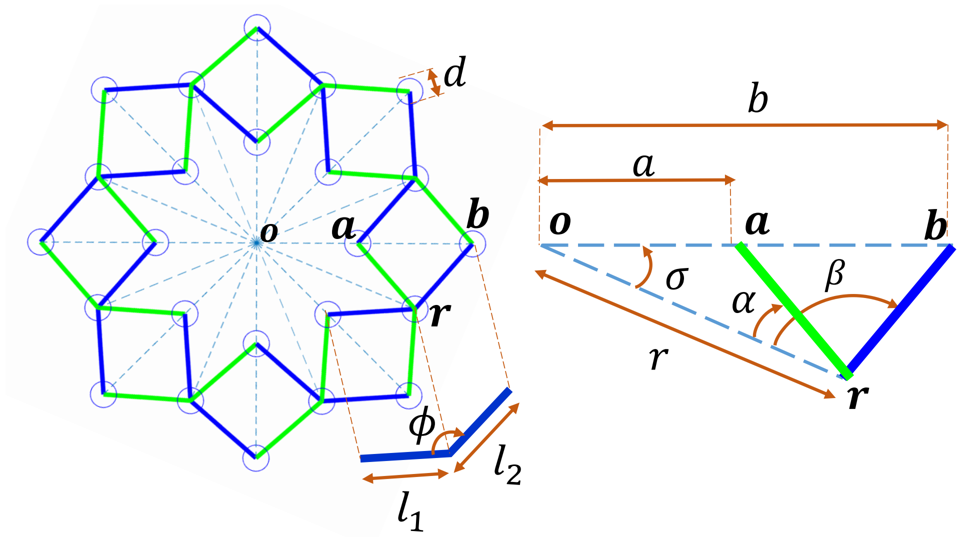

Figure 2.2: Annotated geometric diagram of the ASL.

The radius r is chosen as the independent variable describing the configuration of the linkage. For a given configuration radius (r) and linkage parameters (l_1, l_2, n), we seek to calculate the corresponding radii a and b. In addition, the constraint on the elbow angle ϕ for a physically realizable system is investigated.

2.3.1 Position Analysis

Referring to Fig. 2.2, the radii a and b are calculated by applying the cosine rules to triangles $\triangle$**oar** and $\triangle$**obr**. Note that the relationship between the central angle 2σ and the number of rhombuses n in the ASL is $\sigma = \pi/n$.

$$a = r\cos\left(\frac{\pi}{n}\right) - \sqrt{l_1^2 - r^2\sin^2\left(\frac{\pi}{n}\right)} \tag{2.1}$$

Table 2.1: Angulated Scissor Linkage Nomenclature

n	Number of rhombuses ($n > 2$)
r	Radial distance of mid-range vertices: configuration radius
a	Radial distance of the innermost vertices of the linkage
b	Radial distance of the outermost vertices of the linkage
d	Joint diameter
l_1	Linkage inner arm length
l_2	Linkage outer arm length
2σ	Central angle
α	Angle between a ray and the inner arm of an angulated link
β	Angle between a ray and the outer arm of an angulated link
ϕ	Elbow angle

Table 2.2: Parameters and Variables Classification

	Parameters	Variables
Independent	n, l_1, l_2	r
Dependent	d, σ, ϕ	a, b, α, β

$$b = r\cos\left(\frac{\pi}{n}\right) + \sqrt{l_2^2 - r^2\sin^2\left(\frac{\pi}{n}\right)} \tag{2.2}$$

These solutions correspond to the elbow in and elbow out configuration, respectively, and are only valid for:

$$r < \frac{l_1}{\sin\left(\frac{\pi}{n}\right)} \qquad r < \frac{l_2}{\sin\left(\frac{\pi}{n}\right)} \tag{2.3}$$

2.3.2 Geometric Constraints

For a circular ASL to be radially expandable, it must not violate the structural constraint of a fixed elbow angle ϕ . This angle is calculated as a function of the independent linkage parameters l_1, l_2, and n. As shown in Fig. 2.2, the relationship between the angles ϕ, α, and β is:

$$\phi = \alpha + \beta \tag{2.4}$$

where α is solved for by substituting the solution for a into the cosine law for $\triangle$**oar** and β is solved for by substituting the solution for b into the cosine law for $\triangle$**orb**.

$$\alpha = \cos^{-1}\left(\frac{r}{l_1}s_\sigma^2 + c_\sigma\sqrt{1-\left(\frac{r}{l_1}\right)^2 s_\sigma^2}\right) \tag{2.5}$$

$$\beta = \cos^{-1}\left(\frac{r}{l_2}s_\sigma^2 - c_\sigma\sqrt{1-\left(\frac{r}{l_2}\right)^2 s_\sigma^2}\right) \tag{2.6}$$

where $c_\sigma = \cos(\pi/n)$ and $s_\sigma = \sin(\pi/n)$.

Figure 2.3 is a plot of the elbow angle ϕ, as a function of the dimensionless linkage radius r/l_1, for different arm length ratios (l_2/l_1). It is apparent that ϕ only remains constant for the length ratio $l_2/l_1 = 1$. Therefore, for a physically realizable system, both arms of the elbow-shape links must have the same lengths ($l_2 = l_1$).

The choice of ϕ is dependent on the number of rhombuses (n) used to assemble the linkage, and thus on the central angle (2σ). The relations $\phi(n)$ and $\phi(2\sigma)$ are illustrated in

Fig. 2.4.

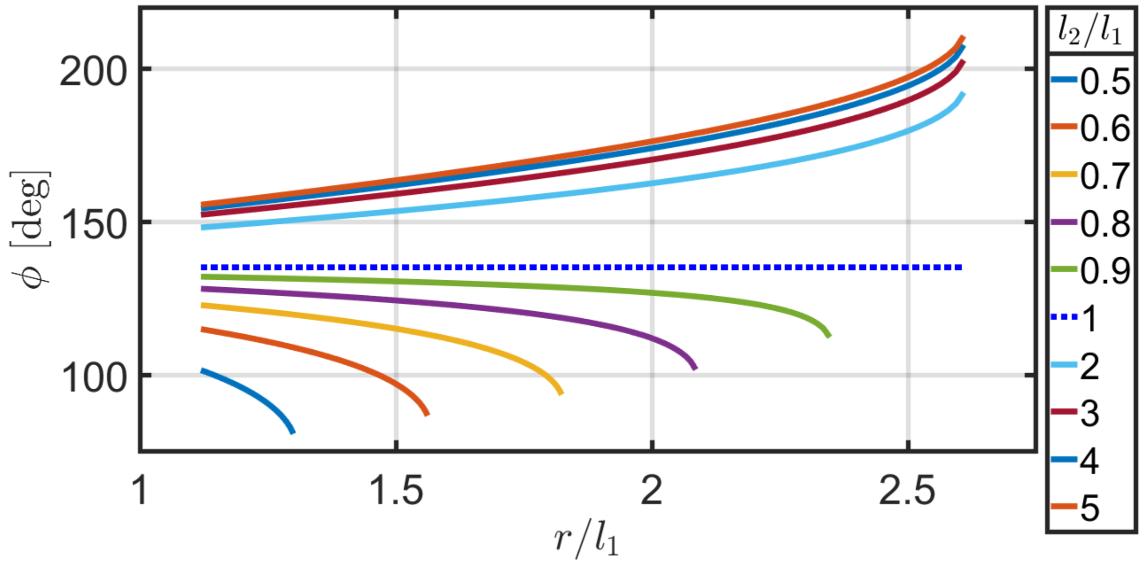

Figure 2.3: Plot of the elbow angle (ϕ) vs. (r/l_1) for various arm length ratios (l_2/l_1).

2.3.3 Local and Global Extrema of Linkage Vertices

Here, we investigate the range of achievable radii for vertices **a**, **r** and **b**. This range depends on the linkage parameters (l_1, n), and the diameter (d) of the physical joints. Fig. 2.5 shows the boundary configurations of the linkage. In the folded configuration (r_{min}), the joints of the innermost vertices collide and become tangent to each other as seen in Fig. 2.5(a). The governing equation is:

$$a = \frac{d}{2\sin(\frac{\pi}{n})} \tag{2.7}$$

Solving the cosine law for $\triangle$**oar**, we express the radius r as a function of a:

$$r = a\cos\left(\frac{\pi}{n}\right) + \sqrt{l_1^2 - a^2\sin^2\left(\frac{\pi}{n}\right)} \tag{2.8}$$

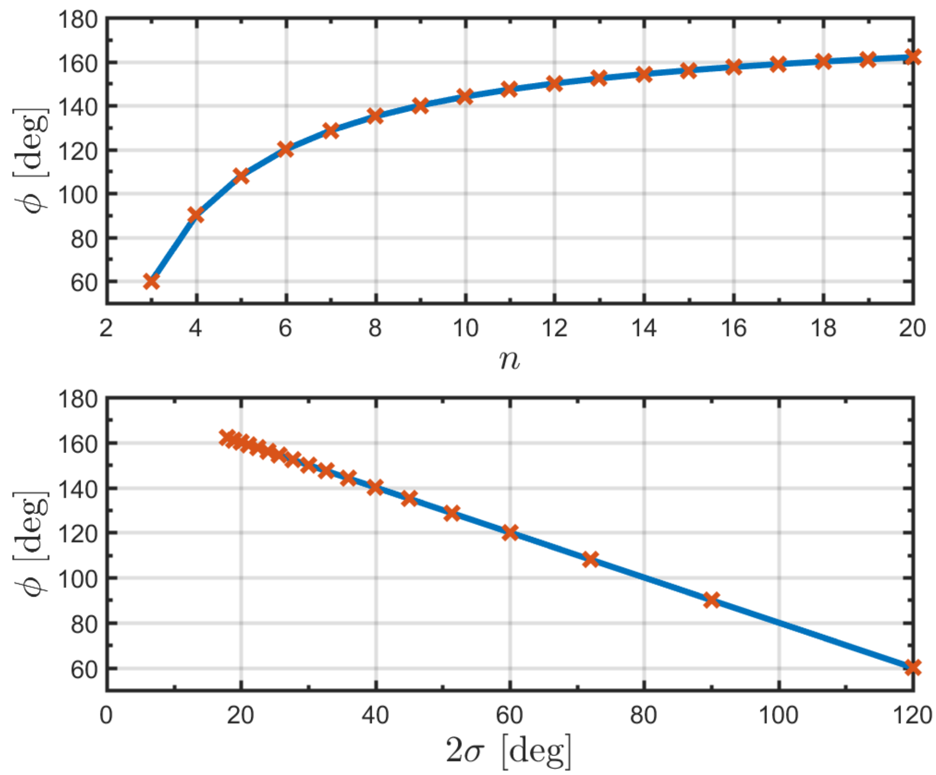

Figure 2.4: Elbow angle ϕ as a function of number of rhombuses n and interior angle 2σ.

By substituting (2.7) into (2.8), the minimum linkage radius is formulated:

$$r_{min} = \frac{d}{2\tan\left(\frac{\pi}{n}\right)} + \sqrt{l_1^2 - \left(\frac{d}{2}\right)^2} \tag{2.9}$$

The linkage at its expanded configuration (r_{max}) is illustrated in Fig. 2.5(b). At this configuration, the innermost joints are tangent to the outermost joints (i.e. $b - a = d$). Substituting (2.1) and (2.2) into this tangency constraint and solving for r, the maximum linkage radius is calculated:

$$r_{max} = \frac{1}{\sin\left(\frac{\pi}{n}\right)} \sqrt{l_1^2 - \left(\frac{d}{2}\right)^2} \tag{2.10}$$

Note that r_{max} satisfies the constraint set in (2.3).

Next, the ranges of motion of the innermost and outermost vertices are investigated and

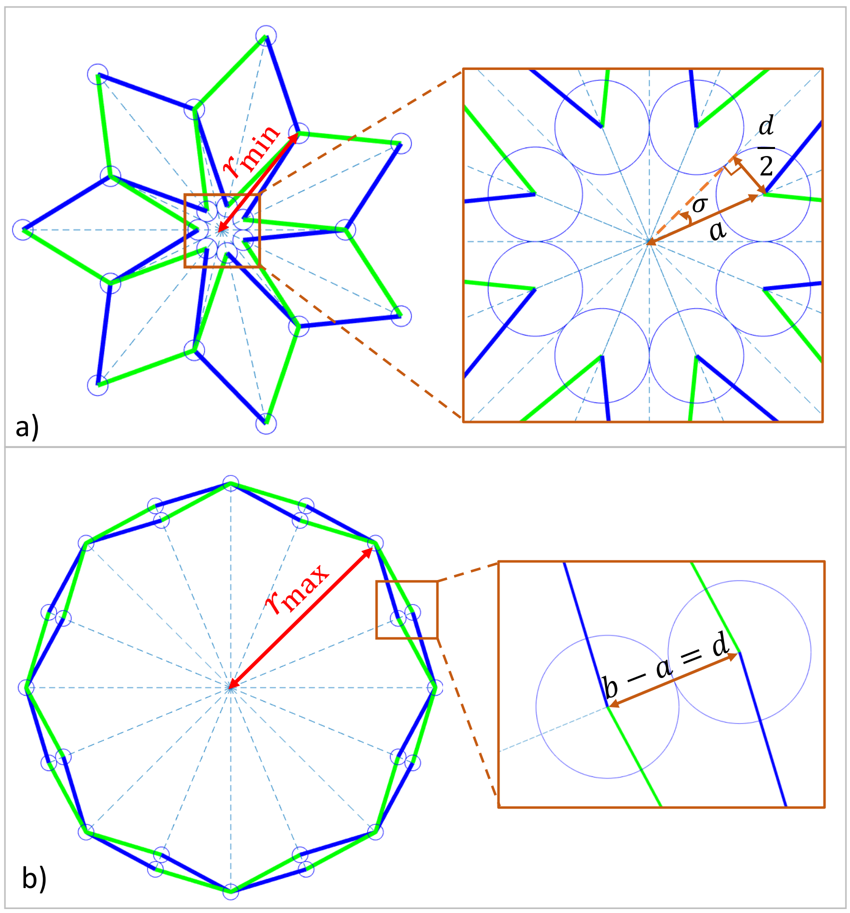

Figure 2.5: ASL at its boundary configurations: (a) folded (r_{min}) and (b) expanded (r_{max})

compared to determine the optimal positioning of the secondary backbones and linkage actuation. The derivatives of (2.1) and (2.2) with respect to radius r are calculated to determine local extrema of a and b, respectively.

$$\frac{da}{dr} = \cos\left(\frac{\pi}{n}\right) + \frac{r\sin^2\left(\frac{\pi}{n}\right)}{\sqrt{l_1^2 - r^2\sin^2\left(\frac{\pi}{n}\right)}}$$

$$\frac{db}{dr} = \cos\left(\frac{\pi}{n}\right) - \frac{r\sin^2\left(\frac{\pi}{n}\right)}{\sqrt{l_1^2 - r^2\sin^2\left(\frac{\pi}{n}\right)}} \tag{2.11}$$

Given that $n > 2$, da/dr is positive for all physically admissible values of r, meaning that the radius a has no local extremum. The radius b, on the other hand, has a local maximum which is calculated by setting db/dr to zero and substituting the corresponding radius r into (2.2):

$$\frac{db}{dr} = 0 \Rightarrow r = \frac{l_1}{\tan\left(\frac{\pi}{n}\right)} \tag{2.12}$$

$$b_{max} = \frac{l_1}{\sin\left(\frac{\pi}{n}\right)} \tag{2.13}$$

The relations (2.1) and (2.2) linking the radii a and b to the input radius r are normalized and plotted for different values of number of rhombuses n in Fig. 2.6. For each value of n, the range of r is such that $r\,\varepsilon\,[r_{min}, r_{max}]$.

As predicted, the radius a has no local extremum while the radius b has a local maximum at $r/l_1 = 1/\tan(\pi/n)$. The global extremum a_{min} and a_{max} are functions of r_{min} and r_{max}, respectively:

$$a_{min} = f_a(r_{min}) \qquad a_{max} = f_a(r_{max}) \tag{2.14}$$

where f_a is the relation defined in (2.1).

The trend in the global minimum (b_{min}) is noteworthy; for $n < 6$, b_{min} occurs at the expanded linkage configuration(r_{max}), and for $n \geq 6$, b_{min} occurs at the folded configuration

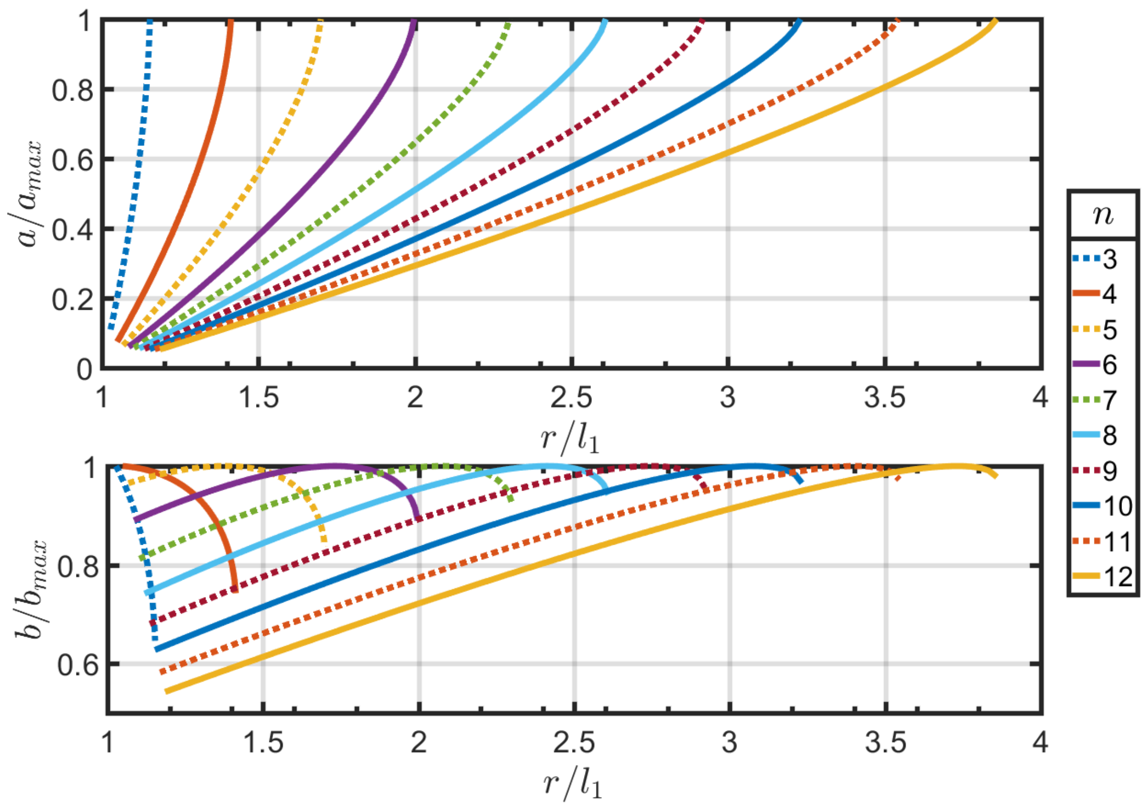

Figure 2.6: Normalized relation between the radii a vs r (top), and b vs r (bottom) for different number of rhombuses n. The radius a has no local extremum, while radius b has a local maximum at $r/l_1 = 1/\tan(\pi/n)$.

(r_{min}).

$$b_{min} = \begin{cases} f_b(r_{max}), & \text{if } 2 < n < 6 \\ f_b(r_{min}), & \text{otherwise.} \end{cases}$$

where f_b is the relation defined in (2.2).

2.3.4 Range of Motion of Linkage Vertices

Figure 2.7 compares the normalized radial change of points **a**, **r** and **b** as a function of the number of rhombuses n. For all values of n, the innermost vertices (points **a**) of the linkage achieve the widest range of radial change. For $n < 6$, the normalized radial change of the outermost vertices (points **b**) is inversely proportional to the radial change of points **r** and **a**. For $n \geq 6$, this trend is reversed, and all three vertices move in the same radial direction. This behavior is shown in part 2 of the multimedia extension.

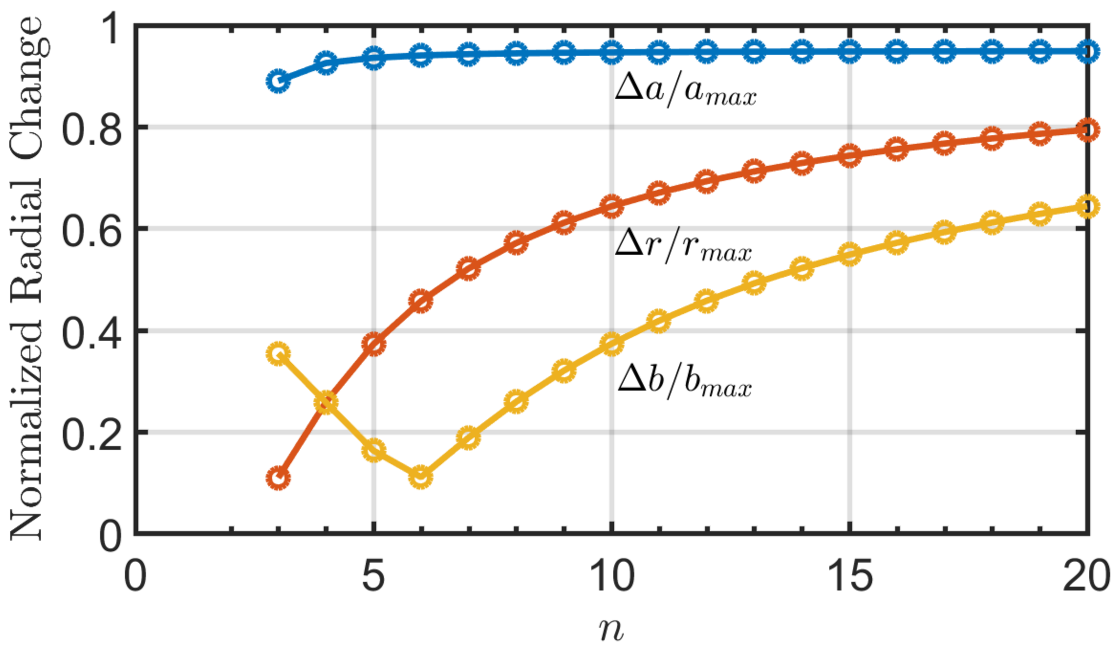

Figure 2.7: Comparison of the dimensionless ranges of motion achieved by innermost, mid-range, and outermost vertices of a linkage (a, r, and b, respectively) as a function of the number of rhombuses n.

Given that the radii a and r are proportional for all values of n, we made the design choice of placing the four secondary backbones of the continuum robot at the mid-range vertices (radius r). The linkage can then be actuated using either torque tubes coupled to a screw drive or the wire-pulley design described above to bring points **a** and **b** closer to each other. In order to keep the secondary backbones radially symmetric, the linkage was designed with $n = 8$ rhombuses, which corresponds to a 26% change of the outer diameter (points **b**).

2.4 Constraints on Radial Expansion

Section 2.3 explored the allowable radial expansion and contraction, as a function of the linkage parameters l_1, n, and d. In this section, interference between the disks of continuum segment is investigated as an additional constraint on the diameter expansion.

Consider a continuum segment of length L, with n_d identical disks of height h_d. The pitch radius and outer radius of the segment are the dimensions r and b of the circular ASL, respectively. Fig. 2.8 shows a case of disk interference; the trigonometry of the hashed triangle is such that:

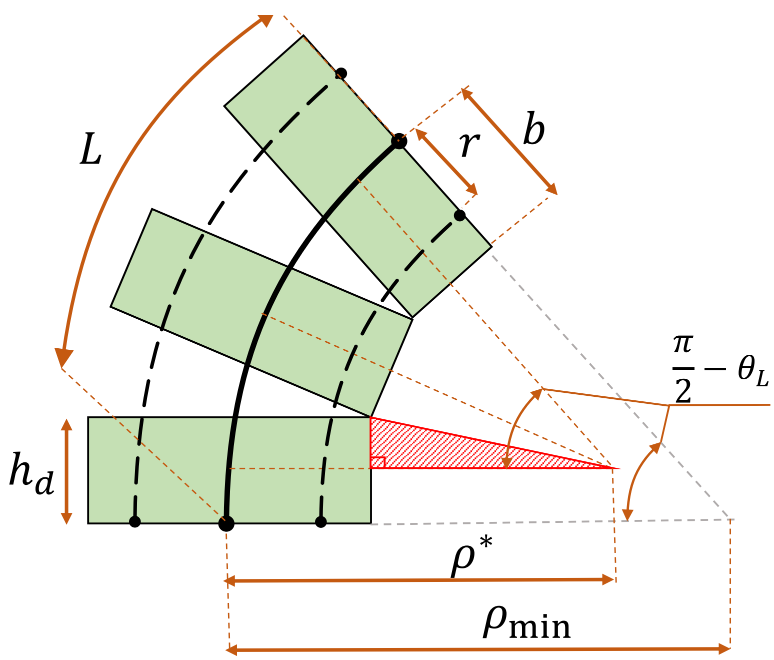

Figure 2.8: MBCR disk interference. The maximal outer diameter b is a function of θ_L and the packing fraction (PF).

$$\tan\left(\frac{\pi/2-\theta_L}{2(n_d-1)}\right)=\frac{h_d/2}{\rho^*-b} \tag{2.15}$$

where $\rho^*=(L-h_d)/(\pi/2-\theta_L)$.

Solving (2.15) for b and substituting ρ^*, the following relation is obtained:

$$b=h_d\left(\frac{1}{\Theta}-\frac{1}{2\tan\left(\frac{\Theta}{2(1-n_d)}\right)}\right)-\frac{L}{\Theta} \tag{2.16}$$

where $\Theta=\theta_L-\frac{\pi}{2}$.

The packing fraction of a continuum robot ($PF\,\varepsilon\,[0,1]$) was defined in [95] as a dimensionless parameter that describes the fraction of a segment backbone that is occupied by spacer disks:

$$PF\triangleq\frac{n_d h_d}{L} \tag{2.17}$$

Rewriting (2.16) to be independent of the segment length L, and dependent on the packing fraction PF, we obtain the dimensionless maximum allowable outer radius b/L, as a function of the configuration variable Θ:

$$\frac{b}{L}=\frac{PF}{n_d}\left(\frac{1}{\Theta}-\frac{1}{2\tan\left(\frac{\Theta}{2(1-n_d)}\right)}\right)-\frac{1}{\Theta} \tag{2.18}$$

This equation signifies that the maximum allowed radial expansion b/L is proportional to the packing fraction, and inversely proportional to the bending of the continuum segment. Indeed, higher packing fraction corresponds to reduced bending of the segment, which decreases the probability of disk interference during radial expansion.

2.5 Instantaneous Kinematics of a Variable Diameter Continuum Robot

Referencing [96], the motion of MBCRs can be represented in three main subspaces. a) The configuration space, $\psi=[\theta_L,\delta]^{\mathrm{T}}$, describes two degrees of freedom of a continuum segment, namely the in-plane bending angle θ_L, and the orientation angle of the bending plane δ. b) The joint space $\boldsymbol{q} = [q_1, ..., q_4]^{\mathrm{T}}$ describes the displacement of the secondary backbones used for actuation. c) The task space $\boldsymbol{x}$ describes the pose of the end effector, expressed in cartesian coordinates. The Jacobian $\mathbf{J}_{\boldsymbol{q}\boldsymbol{\psi}}$ links the joint space to configuration space, and $\mathbf{J}_{\boldsymbol{x}\boldsymbol{\psi}}$ links the task space to configuration space. Both were derived previously in [97]. The variable diameter feature creates an additional joint variable: the linkage actuation radius a. Thus, an *augmented joint space* vector is defined as $\widetilde{\boldsymbol{q}} = [\boldsymbol{q}^{\mathrm{T}}, a]^{\mathrm{T}}$. The Jacobian $\mathbf{J}_{\tilde{\boldsymbol{q}}\boldsymbol{\psi}}$ linking this new joint space vector $\widetilde{\boldsymbol{q}}$ to the configuration vector $\boldsymbol{\psi}$ is derived in this section.

The length of the i^{th} secondary backbone L_i is a function f_i of the pitch radius r, and the configuration variables θ_L and δ (see [96]):

$$L_i = f_i\left(r(a), \theta_L, \delta\right) = L + r\Theta\cos(\delta_i) \tag{2.19}$$

where $\delta_i = \delta + (i-1)\frac{\pi}{2}$. Differentiating L_i with respect to time yields:

$$\frac{dL_i}{dt} = \dot{q}_i = \frac{\partial f_i}{\partial r}\dot{r} + \frac{\partial f_i}{\partial \theta_L}\dot{\theta}_L + \frac{\partial f_i}{\partial \delta}\dot{\delta} \tag{2.20}$$

Writing (2.20) in terms of a and separating the configuration variables from the joint variables, we obtain:

$$\dot{q}_i - \frac{\partial f_i}{\partial r}\left(\frac{dr}{da}\right)\dot{a} = \frac{\partial f_i}{\partial \theta_L}\dot{\theta}_L + \frac{\partial f_i}{\partial \delta}\dot{\delta} \tag{2.21}$$

where dr/da is obtained from taking inverse of da/dr, calculated in (2.11). Combining the instantaneous velocities of all four backbones into matrix form yields:

$$\underbrace{\begin{bmatrix} \boldsymbol{I}_{4\times 4} & -\Theta\frac{dr}{da}\begin{bmatrix} \cos\delta_1 \\ \vdots \\ \cos\delta_4 \end{bmatrix} \end{bmatrix}}_{\mathbf{A}} \dot{\widetilde{\boldsymbol{q}}} = \mathbf{J}_{\boldsymbol{q}\boldsymbol{\psi}}\dot{\boldsymbol{\psi}} \tag{2.22}$$

The augmented Jacobian $\mathbf{J}_{\tilde{q}\psi}$ linking the augmented joint space $\dot{\tilde{\boldsymbol{q}}}$ to the configuration space $\dot{\boldsymbol{\psi}}$ is then given by:

$$\mathbf{J}_{\tilde{q}\psi} = \mathbf{A}^{+}\mathbf{J}_{q\psi} \tag{2.23}$$

where $\mathbf{A}^{+}$ is the pseudo inverse of the 4×5 matrix $\mathbf{A}$.

2.6 Statics Modeling

2.6.1 Statics Using Virtual Work

The statics of this variable diameter continuum robot are derived using the virtual work principle similar to the steps in [96]. Here, the case where the robot is actuated by torque tubes is considered, so the actuating force that changes the diameter does not act against the secondary backbone forces. For this actuation scheme, the springs within the mechanism are not used. Gravitational energy and the energy of the coaxial springs (on the secondary backbones) can be considered negligible compared to the bending energy of the backbones, so the elastic energy of the robot is given by the sum of the circular bending energy in each of the secondary backbones:

$$U = f(\Theta, \delta, r) = \sum_{i=1}^{4} \left(\frac{EI\Theta^2}{2L_i} \right) \tag{2.24}$$

where E is the Young's modulus of the backbones and I is the area moment inertia of the backbone's cross section.

An external wrench $\mathbf{W}_e$ applied to the end disk produces a virtual displacement $\Delta\boldsymbol{x}$ as well as a corresponding displacement of the joint positions $\Delta\widetilde{\boldsymbol{q}}$. If the actuator forces required to maintain equilibrium are given by $\widetilde{\boldsymbol{\tau}}$, the total change in energy of the manipulator is given as:

$$\mathbf{W}_e^{\mathrm{T}}\Delta\boldsymbol{x} + \widetilde{\boldsymbol{\tau}}^{\mathrm{T}}\Delta\widetilde{\boldsymbol{q}} - \nabla U_r \Delta r - \nabla \boldsymbol{U}_{\psi}^{\mathrm{T}}\Delta\boldsymbol{\psi} = 0 \tag{2.25}$$

where the scalar ∇U_r is the gradient of (2.24) with respect to the kinematic radius r and the vector $\nabla \boldsymbol{U}_{\psi}$ is the gradient of (2.24) with respect to the configuration vector $\boldsymbol{\psi}$:

$$\nabla U_r = -\frac{EI\Theta^3}{2}\sum_{i=1}^{4}\left(\frac{\cos(\delta_i)}{L_i}\right) \tag{2.26}$$

$$\nabla \boldsymbol{U}_{\psi} = EI\begin{bmatrix} \sum_{i=1}^{4}\frac{\Theta}{L_i} - \frac{r\Theta^2}{2}\sum_{i=1}^{4}\frac{\cos(\delta_i)}{L_i^2} \\ \\ \frac{r\Theta^3}{2}\sum_{i=1}^{4}\frac{\sin(\delta_i)}{L_i^2} \end{bmatrix} \tag{2.27}$$

Taking note of the following definitions:

$$\Delta\boldsymbol{x} = \mathbf{J}_{\boldsymbol{x}\psi}\Delta\psi, \quad \Delta\widetilde{\boldsymbol{q}} = \mathbf{J}_{\tilde{\boldsymbol{q}}\psi}\Delta\psi, \quad \Delta r = \mathbf{J}_{r\psi}\Delta\psi \tag{2.28}$$

the virtual work expression in (2.25) can be written as:

$$\mathbf{J}_{\tilde{\boldsymbol{q}}\psi}^{\mathrm{T}}\widetilde{\boldsymbol{\tau}} = \mathbf{J}_{r\psi}^{\mathrm{T}}\nabla U_r + \nabla \boldsymbol{U}_{\psi} - \mathbf{J}_{\boldsymbol{x}\psi}^{\mathrm{T}}\mathbf{W}_e \tag{2.29}$$

The minimum-norm joint forces are then given by:

$$\widetilde{\boldsymbol{\tau}} = (\mathbf{J}_{\tilde{\boldsymbol{q}}\psi}^{\mathrm{T}})^{+}\left[\mathbf{J}_{r\psi}^{\mathrm{T}}\nabla U_r + \nabla \boldsymbol{U}_{\psi} - \mathbf{J}_{\boldsymbol{x}\psi}^{\mathrm{T}}\mathbf{W}_e\right] \tag{2.30}$$

2.6.2 Reducing Actuation Loads by Varying the Diameter

To investigate the effect of variable diameter on the actuator loads, the workspace of a single 2-DoF continuum segment was scanned for $-\frac{\pi}{2} \le \theta_L \le \frac{\pi}{2}$ and $0 \le \delta \le 2\pi$. At each point, the maximum and minimum allowable radii were calculated using the criteria in Sections 2.3 and 2.4. Then, the actuation loads from (2.30) were determined for both $r = r_{max}$ and $r = r_{min}$. During this simulation, it was assumed that the backbones can support a specific payload ratio p_r, defined as the ratio of the magnitude of a load on the end disk to the maximal load that a single backbone can carry (300 N). At each configuration, the direction of the end-effector force was sampled in all directions, with

30° steps in yaw and pitch. Any pose was considered within the segment's workspace if all actuation loads resulted in p_r smaller than an allowable payload ratio. The surface area of a Delaunay triangulation of the resulting point cloud was then used for comparing the workspaces. Figure 2.9 shows the point cloud results of this simulation for $p_r = 0.4$. When the diameter is maximized, the robot is able to reach 50% of the commanded poses. However, when the diameter is minimized, the robot is only able to reach the poses near the straight configuration (18% of the workspace). The achievable workspace increases by 64% by varying the diameter from minimal to maximal radius. Finally, Fig. 2.10 shows the achievable workspace for various allowable payload ratios.

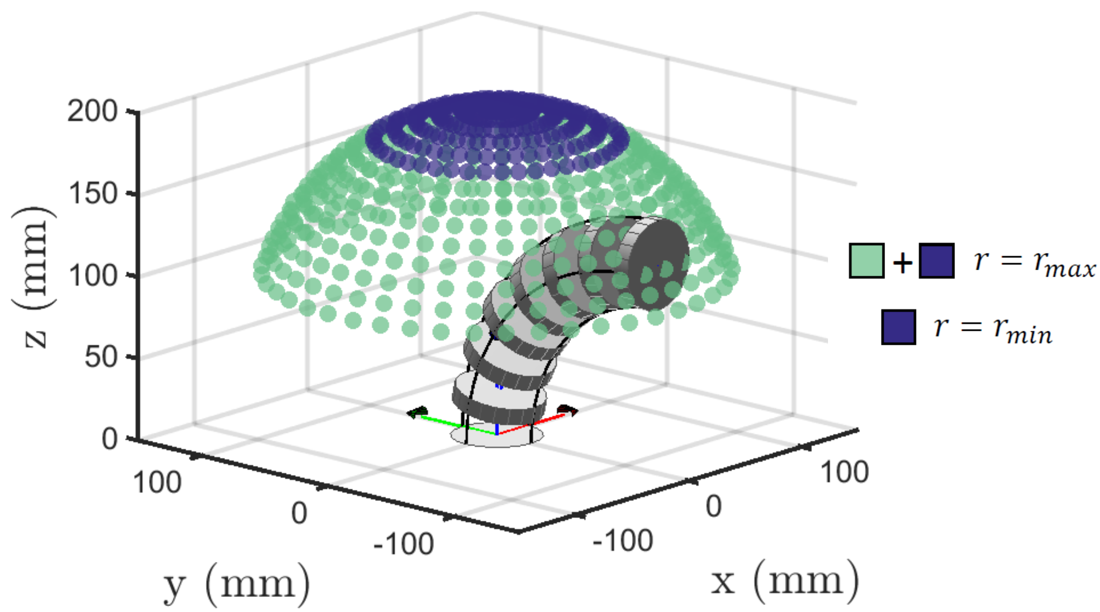

Figure 2.9: Workspace satisfying payload ratio $p_r = 0.4$. When the diameter is minimized, only the poses near the straight configuration (dark blue) are achieved.

2.7 Redundancy Resolution for Optimizing Actuator Forces and Workspace

2.7.1 Gradient Projection Formulation

Here, a redundancy resolution scheme is presented that utilizes the kinematic redundancy provided by the variable diameter mechanism to reduce the required actuator forces. In the above sections, the kinematics of a single 2-DoF segment was presented. Now

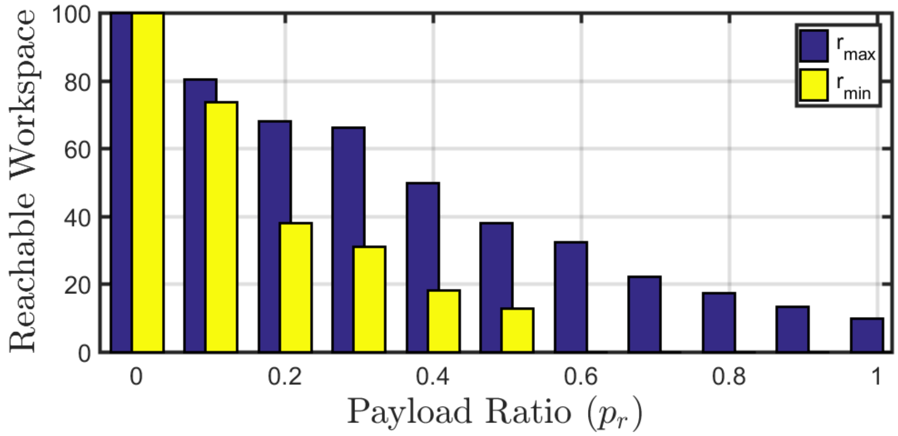

Figure 2.10: Reachable workspace vs. allowable payload ratio.

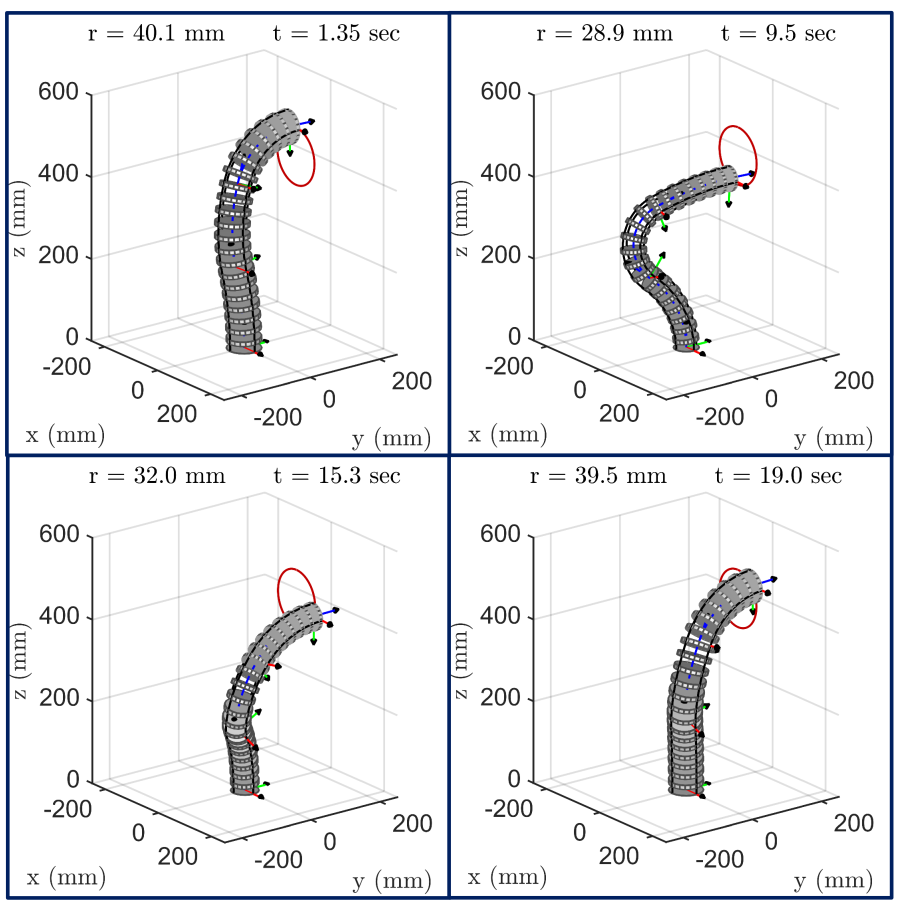

Figure 2.11: Four poses of the manipulator are shown for a trajectory tracking task. The robot uses its variable diameter to reduce actuation forces while avoiding joint limits and preventing disk interference.

consider a 6-DoF multi-segment continuum robot consisting of three stacked segments and four secondary backbones per segment. The segments are assumed to be stacked such that the secondary backbone curves for adjacent segments are aligned. It is also assumed that all segments have the same diameter, which is changed via a single actuation input a. Furthermore, the actuation is assumed to be designed such that the motion of the secondary backbones for each segment is decoupled (see [98] for one such implementation). In the following simulations, the vector of joint variables $\widetilde{\boldsymbol{q}} = [q_1, \cdots, q_6, a]$ includes only two backbones per segment since two of the four backbones are redundant. The instantaneous kinematics of the three-segment robot then takes the following form:

$$\mathbf{A}_s \dot{\widetilde{\boldsymbol{q}}} = \mathbf{J}_{\boldsymbol{q}\psi_s} \dot{\boldsymbol{\psi}}_s \tag{2.31}$$

$$\mathbf{J}_{\boldsymbol{q}\psi_s} = \begin{bmatrix} \mathbf{J}_{\boldsymbol{q}_1\psi_1} & \mathbf{0} & \mathbf{0} \\ \mathbf{0} & \mathbf{J}_{\boldsymbol{q}_2\psi_2} & \mathbf{0} \\ \mathbf{0} & \mathbf{0} & \mathbf{J}_{\boldsymbol{q}_3\psi_3} \end{bmatrix} \tag{2.32}$$

$$\mathbf{A}_s = \begin{bmatrix} & \mathbf{A}_1 \\ \boldsymbol{I}_{6\times 6} & \mathbf{A}_2 \\ & \mathbf{A}_3 \end{bmatrix} \tag{2.33}$$

Referencing (2.22), $\mathbf{A}_i$ is the top-right 2×1 submatrix of $\mathbf{A}$, and $\mathbf{J}_{\boldsymbol{q}_i\psi_i}$ contains the first two rows of Jacobian $\mathbf{J}_{\boldsymbol{q}\psi}$ for the ith segment. The spatial configuration vector is defined as $\boldsymbol{\psi}_s = [\boldsymbol{\psi}_1, \boldsymbol{\psi}_2, \boldsymbol{\psi}_3]^{\mathrm{T}}$. The generalized solution for the inverse kinematics is given by:

$$\dot{\widetilde{\boldsymbol{q}}} = \mathbf{A}_s^{+} \mathbf{J}_{\boldsymbol{q}\psi_s} \dot{\boldsymbol{\psi}}_s + (\mathbf{I} - \mathbf{A}_s^{+} \mathbf{A}_s)\boldsymbol{\eta} \tag{2.34}$$

where $\boldsymbol{\eta}$ is a vector of optimal joint velocities that is projected into the null-space of $\mathbf{A}_s$. The gradient projection method of redundancy resolution gives $\boldsymbol{\eta}$ as:

$$\boldsymbol{\eta} = \lambda \nabla g(\widetilde{\boldsymbol{q}}) \tag{2.35}$$

where $g(\widetilde{\boldsymbol{q}})$ is an objective function that should be locally optimized, and λ is a scalar defining the step size taken along the gradient. To minimize the actuator forces, the objective function can be defined as the weighted sum of the Euclidian norm of the actuator forces and a term associated with the distance from the joint limits [99]:

$$g(\widetilde{\boldsymbol{q}}) = -w_1 \|\widetilde{\boldsymbol{\tau}}_s\| - w_2 \underbrace{\sum_{i=1}^{7} \frac{(q_{max,i} - q_{min,i})}{(q_{max,i} - q_i)(q_i - q_{min,i})}}_{H} \tag{2.36}$$

The 13×1 vector $\widetilde{\boldsymbol{\tau}}_s$ is found using (2.30), except twist transformations are applied to the Jacobian $\mathbf{J}_{\boldsymbol{x}\boldsymbol{\psi}}$ for the second and third segments as shown in [100]. The objective function in (2.36) will minimize the norm of actuator forces except when the robot approaches its joint limits, since H approaches infinity as the joints approach their limits. The joint limits associated with the secondary backbones are constant for a given actuation design. The joint limit for a is updated at each control loop before evaluating (2.34) to account for the possibility of disk interference (see Section 2.3). The gradient of H with respect to the joint variables is simple to derive. For the results below, the gradient of $\|\widetilde{\boldsymbol{\tau}}_s\|$ is computed numerically via finite differences.

2.7.2 Simulation Results

The above redundancy resolution scheme was simulated for the task of tracking a moving target along a circular trajectory in the *x*-*z* plane while keeping the end disk parallel to the *x*-*z* plane, as shown in Fig. 2.11. The circular trajectory was centered at $[0, 150, 435]$ mm, with a radius of 70 mm. The desired $\dot{\boldsymbol{\psi}}_s$ in (2.34) was generated using a singularity-

Table 2.3: Geometric Parameters of the Robot

Backbone OD	L	n_d	PF	l_1	ϕ	n
1 mm	200 mm	8	0.4	20 mm	135°	8

robust inverse of the Jacobian in the instantaneous kinematics expression $\dot{\psi}_s = \mathbf{J}_{x\psi_s}^{-1}\dot{\boldsymbol{x}}$. The three-segment Jacobian $\mathbf{J}_{x\psi_s}$ was found by applying twist transformations to the single-segment Jacobians [100]. The geometric parameters used in the simulations are given in Table 2.3. In addition, the Young's Modulus of the backbone is E = 74 MPa.

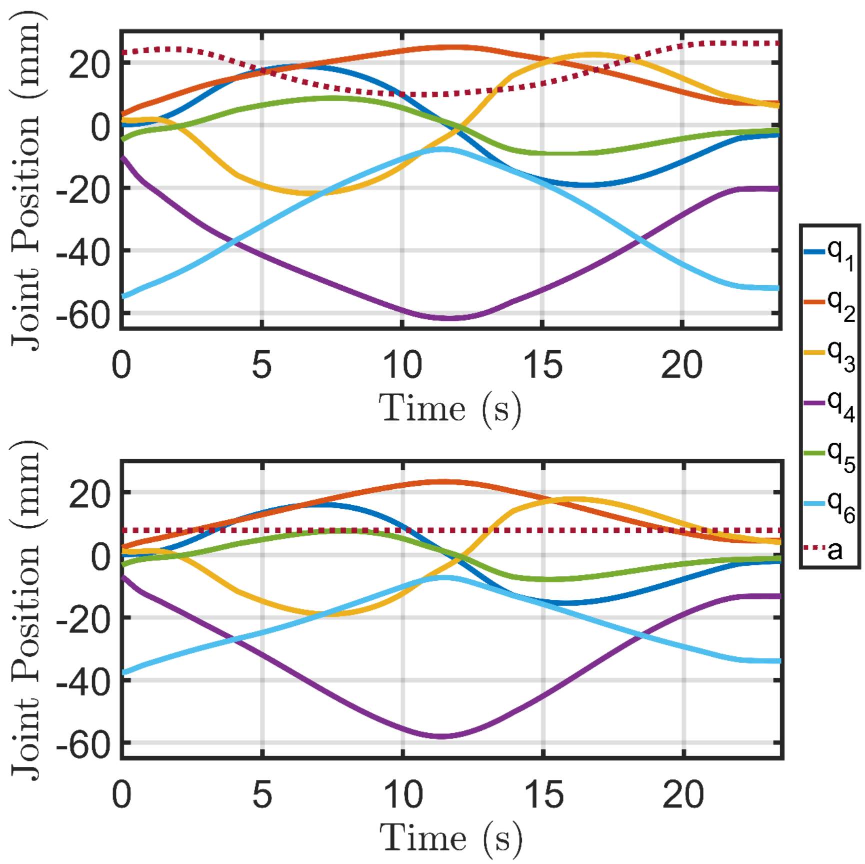

Figure 2.12: (Top): Joint values when the diameter was allowed for vary to reduce actuation forces. (Bottom): Joint values when the diameter is fixed.

The robot was first simulated moving along the circular trajectory while keeping its diameter at a minimum, i.e. $a = a_{min}$. We used $a = a_{min}$ because this provides the largest possible workspace corresponding with onset of collision between the spacer disks. A small diameter does however increase the required actuator forces, so there is generally a trade-off between workspace volume and actuation forces.

The robot was then simulated following the same trajectory while allowing the diameter to vary according to the gradient projection formulation in (2.34). The redundancy resolution parameters were $w_1 = 1$ and $w_2 = 1$ and $\lambda = 0.05$. The simulation sample time was 0.001 seconds. The minimum and maximum values of $\boldsymbol{q}$ associated with the secondary backbones were set to -200 mm and 200 mm, respectively. The minimum and maximum values of a were updated for each time step using the results in Sections 2.3 and 2.4. Both simulations also included a load of 2 kg in the negative z direction, i.e. $\mathbf{W}_e = [0,0,-19.62,0,0,0]^{\mathrm{T}}$, to simulate a payload being carried by the manipulator.

Figure 2.12 shows the joint positions for each of the two simulations. When kinematic redundancy is enabled, the diameter first begins to increase to reduce actuator loads. As the manipulator moves to a pose that causes disk interference, the diameter then decreases to avoid the joint limit on a. As the robot moves back to the starting pose, the diameter again increases to reduce the actuation forces. Snapshots of this sequence are shown in Fig. 2.11.

Figure 2.13 shows the Euclidian norm of joint forces for each simulation. When allowing the diameter to vary, the root mean square reduction in the norm of joint-level forces was 48.3 N with a standard deviation of 17.6 N across the trajectory. In the middle of the trajectory, the robot is in an area of the workspace where the diameter cannot be significantly increased due to disk interference, so the actuator force reduction is more pronounced at the beginning and end of the trajectory. By varying its diameter, the robot benefits from reduced actuator forces while preserving the expanded range of motion provided by a smaller diameter continuum robot.

2.8 Conclusions

In this chapter, we presented a preliminary design exploration of continuum robots with the ability to actively control their diameter by using circular angular scissor linkages (ASL) as spacer disks. To inform this design, we analyzed and compared the motion of

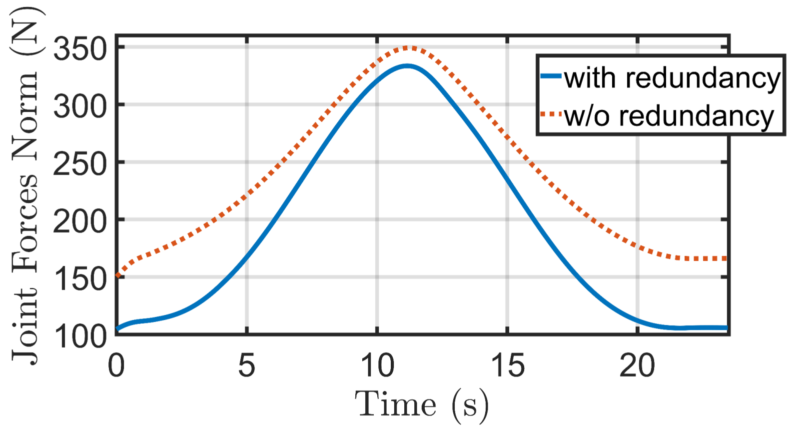

Figure 2.13: Varying the diameter of the manipulator introduces kinematic redundancy that can be used to significantly reduce the required actuator forces.

the innermost, middle-radius, and outermost hinges of the ASL for different numbers of rhombuses. We also investigated the constraints on radial expansion due to hinge collision within the ASL and interference between the spacer disks of the continuum robot. The instantaneous kinematics and statics of a variable diameter MBCR are derived. A redundancy resolution scheme is utilized to compare the performance of a MBCR with and without variable diameter in simulation. The results from this study show that the redundancy introduced by varying the diameter of a MBCR significantly reduces the actuation forces while preserving the workspace and avoiding joint limits. For this reason, we believe that the ability for a continuum robot to adapt its geometric parameters is advantageous in optimizing its performance.

This work is a step towards continuum robots with situational awareness that will use their sensing capabilities to adapt their structure in order to optimize task execution performance.

CHAPTER 3
A MULTI-MODAL SENSOR ARRAY FOR HUMAN-ROBOT INTERACTION AND CONFINED SPACES EXPLORATION USING CONTINUUM ROBOTS

This chapter is adapted from "A Multi-Modal Sensor Array for Human-Robot Interaction and Confined Spaces Exploration Using Continuum Robots" published in "IEEE Sensors Journal" and has been reproduced with the permission of the publisher and my co-authors Andrew Orekhov, Garrison Johnston, and Nabil Simaan © 2021 IEEE.

3.1 Introduction

Industrial workers often perform manufacturing, assembly, and maintenance tasks in confined spaces. For example, construction professionals sometimes explore and repair structural, electrical and pipe systems in crawl spaces of homes. Airplane mechanics have to crawl into the wing space to inspect and repair hydraulic leaks or fuel tanks. Pipeline workers have to inspect and service storage tanks and large pipes from within. These working conditions put them at risk for work-related musculoskeletal disorders due to sustained non-ergonomic postures [15].

Robotic assistance can alleviate this burden by supporting loads and performing repetitive tasks. This working model has become commonplace in open and structured manufacturing environments, where robots are used both autonomously and in close collaboration with workers [101, 102, 103]. However, collaborative manufacturing in confined spaces demands new cooperation modes with levels of dexterity, sensing, and safety that exceed the capabilities of existing robotic systems.

There are three viable approaches for robot deployment in confined spaces: a) full autonomy, b) telemanipulation or *ex situ* collaboration, and c) *in situ* human-robot collaboration. Full autonomy requires precise knowledge of the environment and reduces the repertoire of available tasks to simple, pre-planned tasks. Telemanipulation enables the user to control the robot from outside the confined space, but may not be suitable for applications that require complex manipulation tasks or human sensory presence for quality control. Additionally, most applications that would require robot assistance within a confined space involve operation within semi-structured environments where the basic geometry is known based on the nominal manufacturing plan, but the actual environment differs from this *a priori* plan due to manual customizations (e.g. passing new wire harnesses, pipes and air conditioning ducts). *In situ* human-robot collaboration overcomes the aforementioned limitations by providing robotic assistance for load-bearing and repetitive tasks while keeping the human on site to perform complex tasks or manual customizations.

Thanks to their distal actuation, load bearing capabilities, and inherent compliance (passive safety), continuum robots [18] are well suited for deep reach within confined spaces with a co-located human. These robots include serially-stacked segments with each segment comprised from a base disk, an end disk, spacer disks, a central backbone, and tendons or secondary backbones circumferentially distributed around the central backbone and used for actuation. This robot architecture offers the advantage of reduced moving mass since they can be actuated using cables while maintaining the actuators at the base. To further increase the robot situational awareness, and thus ensure the safety of the collocated human, these robots must be augmented with the ability to a) map their environment, b) sense proximity to neighboring objects, and c) detect and localize contacts along their lengths and circumferences. *In situ* Collaborative Robots (ISCRs) are a novel class of continuum robots that meet these functional requirements.

The literature on sensing methods for continuum robots is extensive. Most works have focused on estimation of the wrench at the end effector by measuring load on actuation lines [24, 104], measuring deflection from equilibrium position [25, 26, 27, 105], or by integrating Fiber-Bragg Gratings sensors [28, 106, 107]. In [108] and [29], a kinematics-based method for contact detection and localization along a multi-segment continuum robot was investigated. One limitation of this work was that while external wrenches applied on separate segments could be detected and localized, multiple contacts along a single segment could be detected but not localized. Chen et al. [30] expanded and adapted this kinematics-based approach for contact detection on pneumatic bellow actuators. Nevertheless, none of these methods are sufficient for *in situ* human robot collaboration, as this application requires contact detection and localization along the full body of the robot. Furthermore, this application requires the integration of additional sensing modalities for force estimation and proximity sensing.

Sensor arrays and robotic skins for whole body sensing have received significant research interest in the past few decades, as surveyed in [109] and [110]. Several works on multi-modal sensing skins, including various combinations of proximity sensing, contact detection, and force sensing, have been published in the context of rigid link robots [31, 32, 33] and soft robots [34, 35, 111]. In [112], the authors present whole-body proximity sensing for human-robot interaction with rigid link robots. However, the integration of multi-modal sensing within the structure of a continuum robot has not previously been considered.

The contribution of this chapter is in presenting the first case of continuum robots capable of environment shape mapping, contact detection, and force sensing, using distributed sensory disk units (SDUs) along their length. A preliminary design of these novel SDUs was presented in [1], but was limited to presenting the design concept of a single SDU and the validation of its potential use on a PUMA560 robot. Relative to our prior work, this work presents a polished and ruggedized redesign of the SDU, along with details of the fabrication process, electronics, communication, integration of these SDUs on a continuum robot segment, and validation of mapping capabilities of a continuum robot using these SDUs. We also present the use of these sensors for contact detection and localization, force sensing, and user interaction using admittance control. All of these new sensory capabilities can open a new horizon for the design and use of continuum robots for human-robot interaction and exploration of unstructured environments.

The rest of this chapter is structured as follows: First, we detail the design specifications and fabrication procedure for the SDU in Section 3.2. Next, we present the characterization and calibration of the different sensing modalities within the SDU in Section 3.3. Finally, in Sections 3.4-3.6, we demonstrate mapping, bracing, and human-robot interaction under compliant motion control using a single SDU mounted on a PUMA robot and an array of SDUs integrated within a continuum robot.

3.2 Design and Fabrication

The overarching goal of this research is to enable safe human-robot collaboration in semi-structured confined spaces. To achieve this goal, the ISCR must be endowed with whole-body situational awareness in order to a) map the confined space to update an *a priori* model of the environment, b) detect approaching objects, c) detect and localize contact along its body, and d) measure applied external force along its body. In addition, these sensing modalities must seamlessly integrate within the structure of the continuum robot without adding bulk or excess cost.

Given these design specifications, we propose an array of multi-modal sensing disk units - SDUs (Fig. 3.1) that serve the dual purpose of sensing elements for whole-body situational awareness and spacer disks for the continuum robot. Spacer disks are passive structural elements on which the central backbone of a continuum robot is mounted and through which tendons slide to achieve controlled bending in different planes [113, 18]. Fig. 3.1-(c) shows an overview of the proposed embodiment: a one-segment continuum robot with an array of five SDUs integrated within its structure and separated by metallic bellows.

Figure 3.2 presents a detailed view of the internal structure and components of an SDU. Each SDU includes eight time-of-flight (ToF) sensors, eight Hall effect sensors, and eight embedded magnets distributed around its circumference.

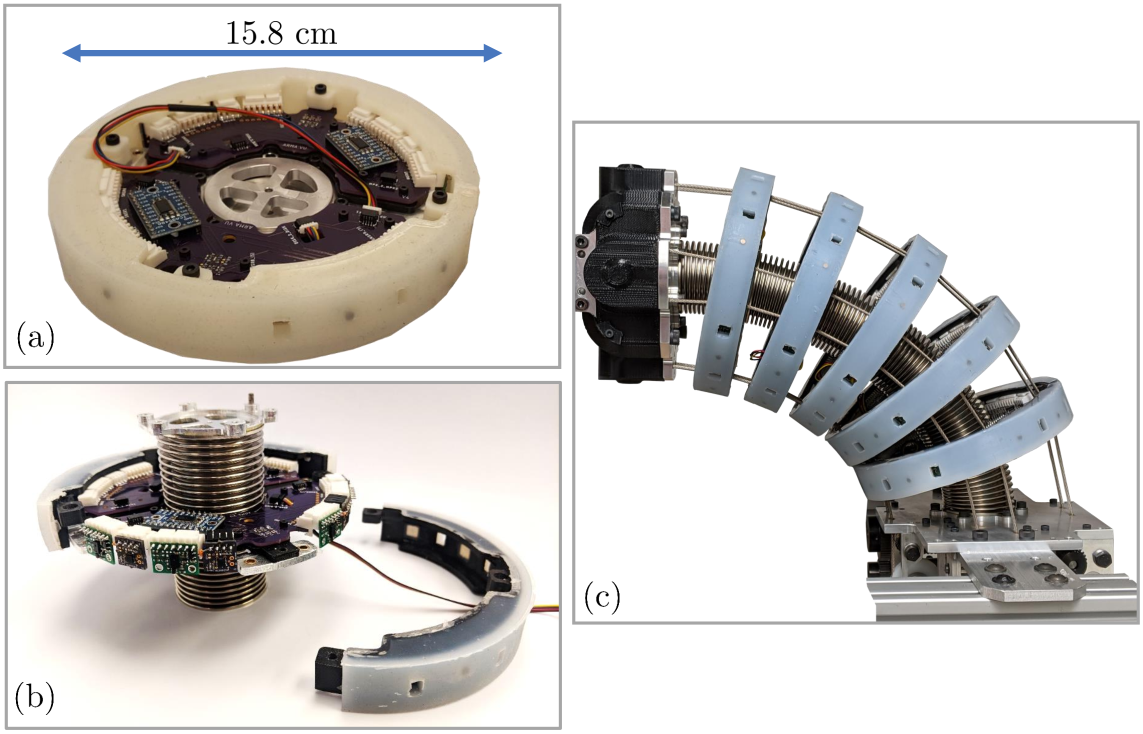

Figure 3.1: (a) Multi-modal sensing disk unit (SDU) with proximity sensing, mapping, localized contact detection, and force sensing capabilities. (b) Section view of the SDU prototype, showing integrated Time-of-flight sensors, Hall effect sensors, and custom multiplexer PCBs. (c) SDUs integrated into the structure of a continuum robot for augmented robot situational awareness.

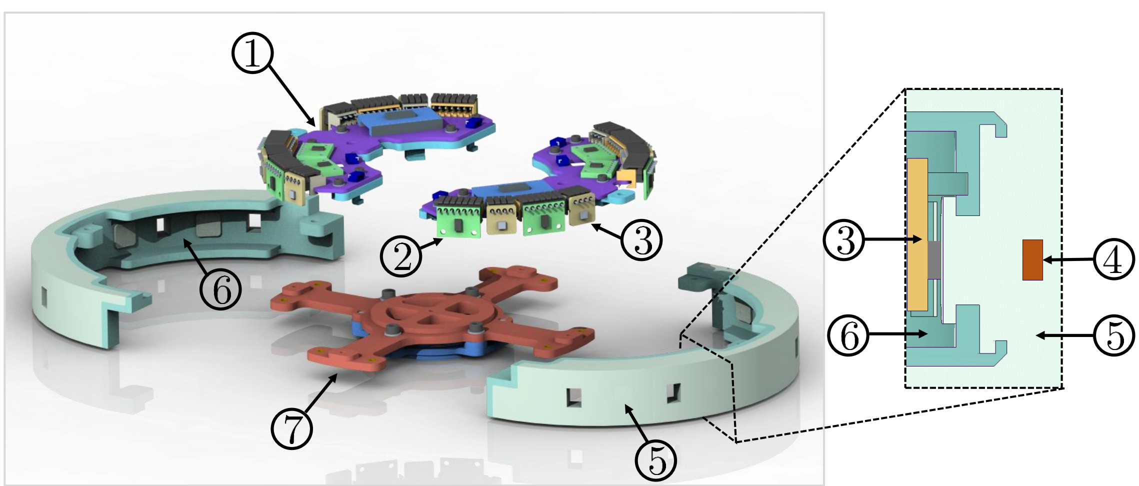

Figure 3.2: The SDU includes two custom PCBs ① for multiplexed I^2C communication between eight time-of-flight (ToF) sensors ②, eight Hall effect sensors ③, and a Teensy microcontroller (not shown). The magnets ④ used for Hall effect sensing are embedded within a silicone sleeve ⑤. This sleeve is overmolded on a 3D-printed half disk cover ⑥ that encases the SDU. These components are mounted onto a core aluminum disk ⑦, for easy integration within a continuum robot.

3.2.1 Time of Flight Sensors

The ToF sensors (STMicroelectronics VL6180X) compute the absolute distance to the nearest object by measuring the time the light takes to travel to the object and reflect back to the sensor. Distributed along the surface of the continuum robot, these sensors enable proximity sensing to detect an approaching object and obtain a point cloud map of the environment. While the density of the map obtained is limited by the physical distribution of the sensors on the robot, a denser map can be obtained by collecting points as the robot is moving or by implementing a control mode in which the continuum robot rotates about its central backbone as presented in [114] . We selected ToF sensors with $0-100$ mm range to be able to accurately predict onset of contact with a human or an object along the body of the continuum robot. Longer range ToF sensors (e.g. VL53L0X) have been considered, but while they increase the range of detectable objects, they are less accurate for short range interactions. Nevertheless, given that their pinout is identical to our current ToF sensors, these sensor models can be easily integrated into the current setup for mixed range proximity sensing and mapping.

3.2.2 Hall Effect Sensors

The Hall effect sensors (Melexis, MLX90393) measure magnetic flux density along their three orthogonal axes of symmetry. To use these sensors for force measurements, we followed the working principle described in [115] and illustrated in the inset of Fig. 3.2. For each Hall effect sensor, there is a radially-offset cylindrical magnet (KJ Magnetics, D21B-N52, 3.175 mm diameter, 1.5875 mm thickness) embedded in a silicone sleeve. Any external contact with the sensor disk displaces the magnet within the silicone, thus causing a change in magnetic flux density, which is detected by the corresponding Hall effect sensor. The uncalibrated measurements can be used as an “on/off" metric for contact detection. Once calibrated with a commercial force sensor, this Hall effect setup can be used as a force sensor. Furthermore, because the sensors are distributed at known locations along the robot, the contact detection and force measurement can be localized. The deformation of the silicone sleeve, caused by the application of an external force, is local and only detectable by the closest Hall sensor. The sensors distribution around the SDU is such that neighboring Hall sensors are separated by at least 30 degrees, i.e. 8.27 cm of arc length.

3.2.3 Silicone Sleeve

In addition to housing the magnets for Hall effect sensing, the silicone sleeve protects the robot from harsh interactions with both the environment and the user. The sleeve is casted directly onto each half disk cover (HDC) shown as ⑥ in Fig. 3.2. Each half disk cover was designed with eight windows that are aligned with each sensor. Four of the windows are dimensioned 6 mm by 8 mm and enable unobstructed ToF sensing. The other four windows are dimensioned 7 mm by 7 mm and are filled with silicone for Hall effect sensing. Furthermore, the HDC has lips (upper and lower) and trapping posts (⑦ in Fig. 3.2) around its edges that ensure permanent adhesion to the silicone sleeve. This fabrication process is an adaptation of “overmolding", which is a type of in injection molding.

This sleeve is fabricated by casting liquid silicone rubber (Advanced Reynolds, Dragon Skin FX Pro) into an assembly that includes the HDC and a custom 3D printed mold, as shown in Fig. 3.3. With a shore 2A hardness, this elastomer is both flexible enough to detect the motion of the embedded magnets, and robust enough to withstand rolling contact with the environment as demonstrated in [1]. The custom mold includes three main subcomponents: a) an outer mold, b) four mold inserts, and c) a magnet holder.

The casting process is as follows: The mold components are sprayed with mold release for easy demolding. The mold inserts are mounted on the HDC such that each rectangular extrusion fits into a ToF window and each rectangular cavity aligns with the Hall sensor window, as shown in Fig. 3.3. This sub-assembly is then mounted into the outer mold. The mold cavity is the semi-circular gap between the outer surface of the HDC and the inner surface of the outer mold. Next, the four cylindrical magnets are mounted onto the claws

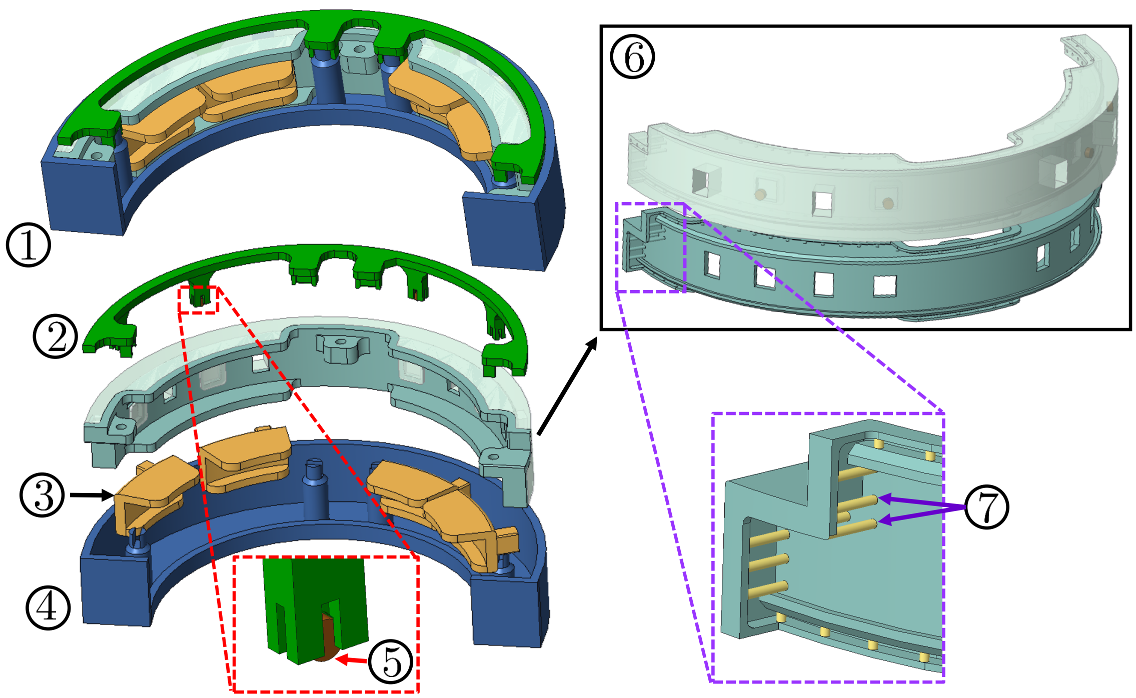

Figure 3.3: Mold design for silicone sleeve fabrication: ① Mold components assembled onto the HDCr, ② magnet holder with claws used for repeatable positioning of the four magnets ⑤. ③ mold inserts (×4) with an extrusion to create windows for time-of-flight sensors and a cavity to create a silicone cushion for the Hall sensor. ④ Outer mold. ⑥ Exploded view of the silicone layer overmolded onto the HDC. Trapping posts ⑦ at the edges of the HDC ensure permanent adhesion of the silicone sleeve.

of the magnet holder, with their orientation matching the inlet in Fig. 3.2. Using the four alignment posts, the magnet holder is assembled onto the outer mold, such that the magnets are suspended within the mold cavity.

The first layer of the two-part liquid silicone (20 g part A, 20 g part B) is mixed, degassed (-30 inHg pressure for three minutes), and poured into the mold cavity until the magnets are fully covered. This layer is then degassed for five additional minutes to remove bubbles formed during the pouring process. The silicone is then left to cure at room temperature for one hour. Once cured, the magnet holder is removed, leaving the magnets trapped in place by the cured silicone.

A second layer of liquid silicone (10 g part A, 10 g part B) is mixed, degassed, and poured to fill the remaining cavity, including the gap left by the magnet holder. Once the second layer is cured, the outer mold and mold inserts are removed, leaving a silicone sleeve overmolded onto the HDC with embedded magnets.

3.2.4 Communication Protocol

For communication between the different sensors and a microcontroller, we use the inter-integrated circuit (I^2C) communication protocol. This protocol enables communication with up to 128 peripheral devices in a bus configuration, as long as each device has a unique 7-bit address. The data transfer between the controller and peripheral devices occurs at up to 100 kbps in Standard Mode.

In our setup, we aim to communicate with 80 sensors (40 ToF and 40 Hall sensors) distributed on five SDUs. The problem is that the ToF sensors all have the same I^2C address (0×29) and the Hall sensors can be hardcoded to one of 16 addresses ($0 \times 0C$ to $0 \times 1B$). To bypass the challenge on non-unique addresses, we use 1-to-8 I^2C multiplexers (Texas Instruments, TCA9548A). This multiplexer includes eight bidirectional switches that can be controlled to enable the selection of any individual channel (0 through 7) or combination of channels at high speed (1 GHz). In addition, these multiplexers can be hardwired to

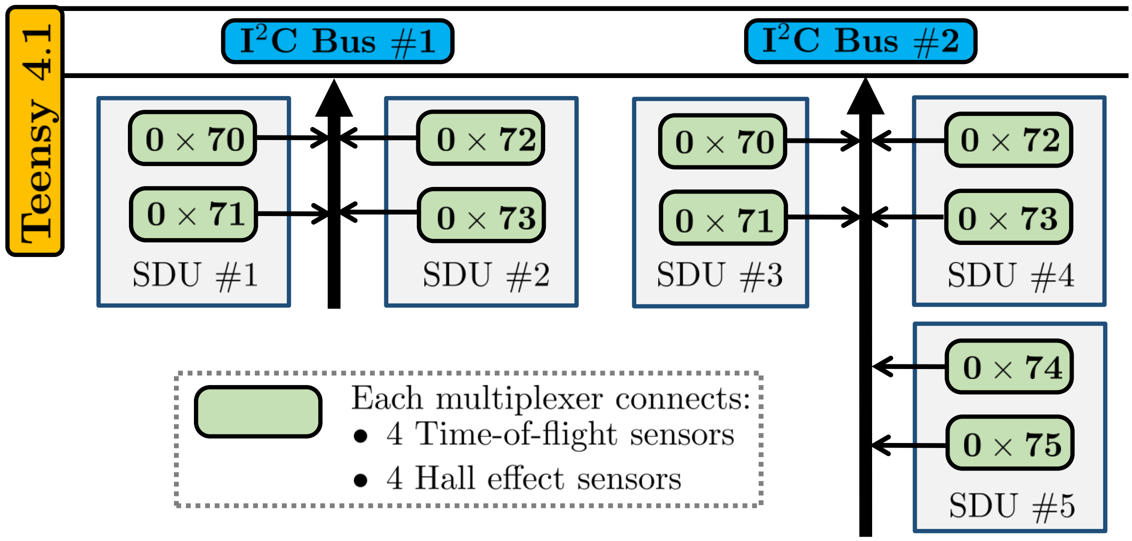

Figure 3.4: Strategy for I^{2}C communication with 40 same-address time-of-flight sensors and 40 same-address Hall sensors, distributed on five disks of a continuum segment.

eight unique addresses (0x70 to 0x77), thus enabling simultaneous communication with 64 sensors, including duplicate addresses.

With the above solution, even when using eight multiplexers, the design falls short of the desired 80-sensors architecture. To overcome this limitation, we selected a microcontroller with multiple I^{2}C buses. Our strategy for interfacing with five SDUs is illustrated in Fig. 3.4. The Teensy 4.1 microcontroller enables the simultaneous use of three I^{2}C buses, which means that up to 192 sensors (64 sensors $\times$ 3 I^{2}C buses) can communicate with a single microcontroller. Even though we could have used all three I^{2}C buses, we reserved the third bus for other sensors we plan to integrate into the segment in the future.

Given this communication architecture, we characterized the speed of sensor data acquisition as a function of the number of active multiplexers (Fig. 3.5). For a single SDU (i.e. two active multiplexers), data can be collected 20.98 Hz. For the full system (five SDUs or ten multiplexers), data be collected at 4.26 Hz. The bottleneck in sensor data acquisition is the convergence time of the ToF sensors. In the worst case (100 mm and 3% reflectance), the convergence time is 10.73 milliseconds for each sensor. This corresponds to 0.43 seconds or 2.33 Hz for all 40 ToF sensors. We were able to increase the speed to 4.26 Hz by decoupling the initialization and reading sequences for the ToF sensors. For deployment in real Human-robot interaction scenarios, we will improve the speed of data acquisition by using faster ToF sensing technology when it becomes available. Theoretically, we can speed up the overall acquisition rate for the 40 ToF sensors by adding more micro-controllers instead of relying on a single Teensy board.

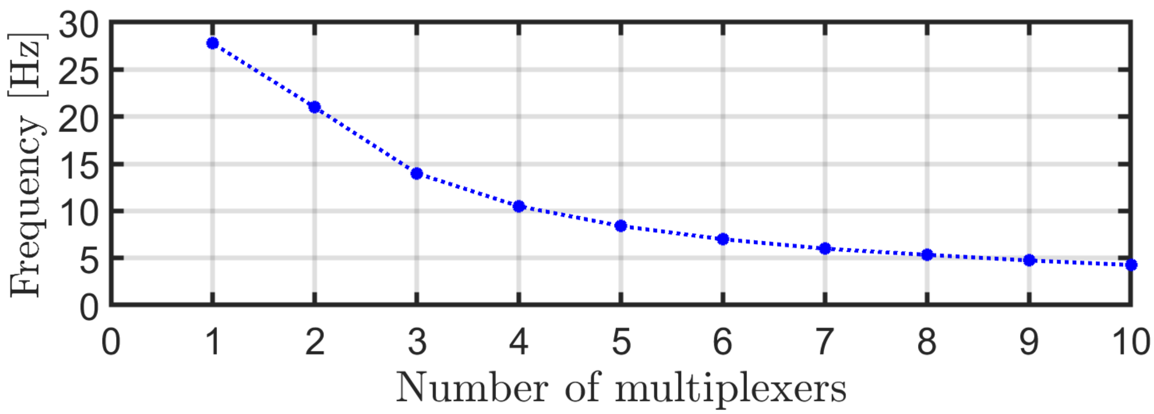

Figure 3.5: Frequency of sensor data acquisition as a function of number of active multiplexers (or half disks)

Each SDU includes two custom “half disk" PCBs that serve as breakout boards for each multiplexer (Fig. 3.6(a)). The sensors are mounted directly on the half disk PCBs using board edge connectors. This architecture facilitates the assembly and troubleshooting of individual sensors, and significantly reduces the number of cables needed. Each half disk PCB includes three QWIIC I^2C connectors (Sparkfun Electronics) that enable daisy-chaining of the half disk PCBs on the same I^2C bus. Each QWIIC connection includes four signals: data (*SDA*), clock (*SCL*), power (V_{in}), and ground (*G*).

A custom “Teensynet" PCB (Fig. 3.6(b)) houses the Teensy 4.1 microcontroller and a WIZ850io ethernet module used for User Datagram Protocol (UDP) communication with the robot’s main controller. This PCB also breaks out the three I^2C buses into individual QWIIC channels with 1 kΩ pull-up resistors on the data and clock lines. The SDU components (ToF sensors, Hall sensors, and multiplexers) and the ethernet module operate at a nominal voltage of 3.3 V, while the microntroller requires 3.6 – 5.5 V input voltage. To reconcile these voltage requirements and enable the use of a single power supply, this

PCB includes a voltage regulator that drops a 5 V input voltage to 3.3 V. Furthermore, the “Teensynet" PCB includes a N-Channel MOSFET that operates as a digital switch to power cycle the SDU sensors.

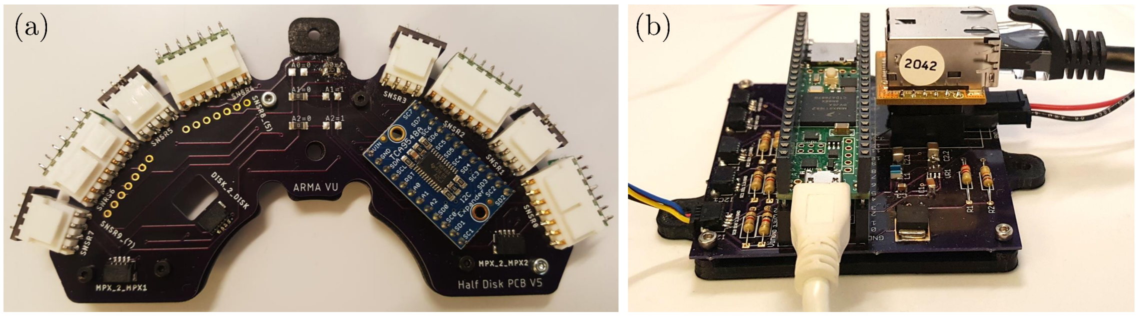

Figure 3.6: (a) Half disk custom PCB. (b) Teensynet custom PCB.

3.3 Characterization and Calibration

The SDU was characterized and calibrated using the experimental setup shown in Fig. 3.7. The SDU was mounted on a manual Sherline™ rotary stage, for precise ($\pm 0.1°$) angular positioning of the sensor of interest. A custom Cartesian Stage Robot was used to control the motion of an end effector relative to the SDU. This Cartesian robot is comprised of ballscrew-driven Parker™ 404XR series linear stages with 200 mm stroke. Each stage was actuated using a 90 Watt brushed DC motor (Maxon™ RE35 #273754) equipped with a 1000 counts per revolution encoder (Avago technologies #HEDM-5540-B11). A computed torque motion controller was tuned and verified to provide motion accuracy of better than 30 μm in each direction.

The SDU and rotary stage are positioned at the corner of the Cartesian robot’s workspace, in order to maximize usable workspace. The planar pose of the SDU relative to the robot frame was determined as follows: a peg was mounted at the end effector of the Cartesian robot and the robot was jogged until the peg aligned into a matching hole on the SDU. This process was repeated for two angles of the rotary stage ($\theta_{rs} = 0°$ and $\theta_{rs} = 90°$), thereby allowing the registration of the center of the SDU.

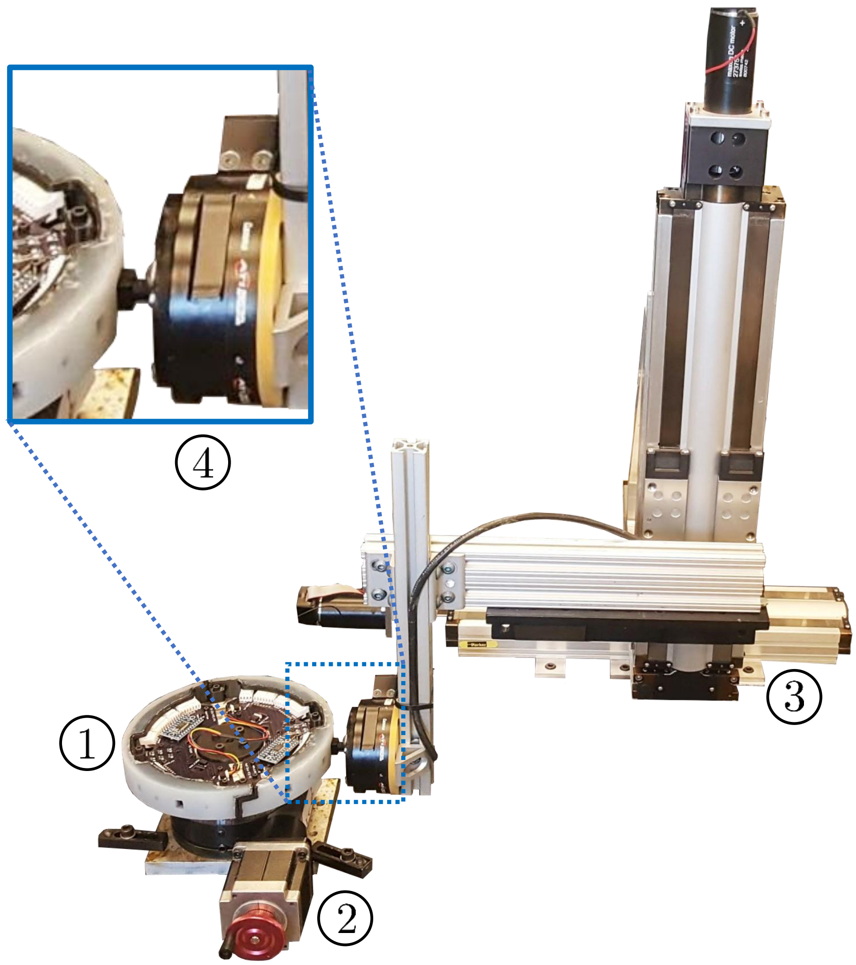

Figure 3.7: Experimental setup for SDU characterization: the SDU ① is mounted on a rotary stage ② that controls the orientation of the sensor of interest, relative to a 3-axis Cartesian stage robot ③. An ATI Gamma force sensor ④ is used to probe the touch sensor and provides a ground truth for force measurements

3.3.1 Hall Effect Sensing and Force Calibration

The goal of this calibration experiment was to identify the relationship between the magnetic flux density measured by a Hall effect sensor and the magnitude of an external force applied to the SDU. To achieve this calibration, a commercial force sensor (ATI Gamma) with a custom square probe (10 mm $\times$ 10 mm) was mounted as the end effector of the Cartesian Stage Robot. We expect that, when the robot contacts the environment, it will have a contact area larger than the Hall effect sensor windows in the HDC. Thus, the probe was designed to achieve uniform (flat) contact with the silicone sleeve and dimensioned to be bigger than the Hall effect windows in the HDC.

This experiment was performed on all eight Hall effect sensors of a single SDU, and the results informed the calibration of the other Hall sensors on the robot. For each sensor, the rotary stage was used to radially align the target sensor with the normal axis of the force sensor. To achieve vertical alignment between the square probe and the Hall sensor, the Cartesian robot was commanded to position the square probe directly above the SDU. The robot was then jogged slowly until contact was established between the bottom surface of the square probe and the top surface of the SDU. Since the vertical position of the Hall sensor relative to the top of the SDU is known from the CAD model, this information is sufficient to vertically align the probe and the Hall sensor.

In its initial configuration, the square probe is aligned (radially and vertically) with the Hall sensor, and positioned at the surface of the SDU. The Cartesian robot then moves the probe into the SDU in increments of 0.1 mm, until a radial force of 10 N was reached. This force level corresponds with 0.1 MPa contact pressure, which roughly translates to 82.25 N contact force between the SDU and a flat surface, with contact area approximating 23.5 mm $\times$ 35 mm. Once the 10 N force threshold is reached, the robot returns to its starting position, using the same incremental motion in the reverse direction. This trajectory was repeated five times for each Hall sensor.

The data collected includes applied force $\mathbf{F}$ in Newtons, end effector position $\mathbf{x}$ in

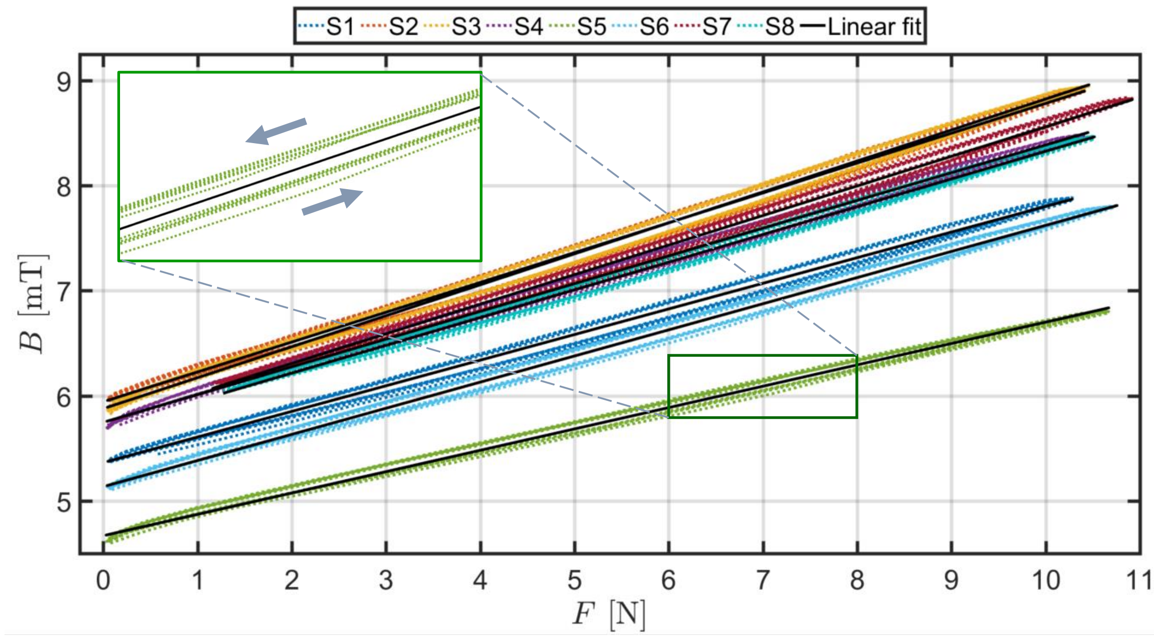

Figure 3.8: Force calibration of eight Hall effect sensors around a single SDU

millimeters, and magnetic flux density **B** in milliTeslas. The magnetic flux density data was acquired using the Teensy 4.1 microcontroller and transferred to Simulink Real Time via UDP using the Teensynet PCB.

Fig. 3.8 shows the force and magnetic flux density raw data, along with the linear fit curves, for eight Hall sensors. The dotted lines show experimental data and solid black lines show the linear fit $\mathbf{B}^* = \alpha \mathbf{F} + B_0$ for each sensor, where B_0 is a magnetic flux bias. These results show a linear and repeatable relationship between the magnetic flux density and the force applied. The average slope for these eight sensors $\bar{\alpha} = 0.26$ mT/N ± 0.03 mT/N. Moving forward, we will unbias all the Hall sensors at startup, and use the average slope α to convert magnetic flux density into force.

The full scale linearity [116] was calculated for each Hall sensor, using (3.1). The average full scale linearity error for the eight Hall sensors was $4.47\% \pm 0.57\%$.

$$\text{B-linearity} = \frac{\max|\mathbf{B} - \mathbf{B}^*|}{\Delta \mathbf{B}} \times 100 \tag{3.1}$$

where $\Delta\mathbf{B}$ is the range of magnetic flux density measurements.

The above linearity data is useful for characterizing the linear model fit to the experimental data. However, if one wishes to use the magnetic flux density $\mathbf{B}$ to sense the force applied, the corresponding model becomes $\mathbf{F}^* = \alpha^{-1}(\mathbf{B} - B_0)$ and the full scale linearity error becomes:

$$\text{F-linearity} = \frac{\max|\mathbf{F} - \mathbf{F}^*|}{\Delta\mathbf{F}} \times 100 \tag{3.2}$$

The force linearity calculation yielded $4.52\% \pm 0.56\%$. While this is a relatively large force error, these sensors can still be practical and useful to measure force interactions with the user.

3.3.2 Proximity Sensing Characterization

In this characterization experiment, our aim was to determine the dimensions of the ToF detection cones, the distance sensing error, the sensitivity to change in object colors and reflectivity, and the repeatability of measurements across different ToF sensors on the SDU. We utilized the setup shown in Fig. 3.7, with a Delrin® rod of diameter 50.8 mm mounted as the Cartesian robot's end effector, replacing the force sensor assembly. The rod diameter was chosen to approximate the size of a human wrist, which is the narrowest portion of the human anatomy likely to interact with the robot during a collaborative task. While a finger is narrower than the wrist, it is unlikely that a single finger is detected in isolation, without the rest of the palm.

The Cartesian robot's trajectory was chosen such that the Delrin rod sweeps through the detection cone of the target ToF sensor, in increments of 5 mm arch length and 1 mm radius. The VL6180X datasheet reports the ToF detection cone dimensions as $\pm 12.5°$ angle and 100 mm height. In its initial configuration, the rod touches the SDU outside the range of the ToF sensor of interest. The rod then sweeps for $\pm 15°$ about the central plane of the target ToF sensors, with the radius increasing until the rod is at a radius of 135 mm away from the ToF sensor of interest. At each waypoint along the path, the robot pauses until 20 sensor readings are collected. A top view of this setup is illustrated in Fig. 3.9.

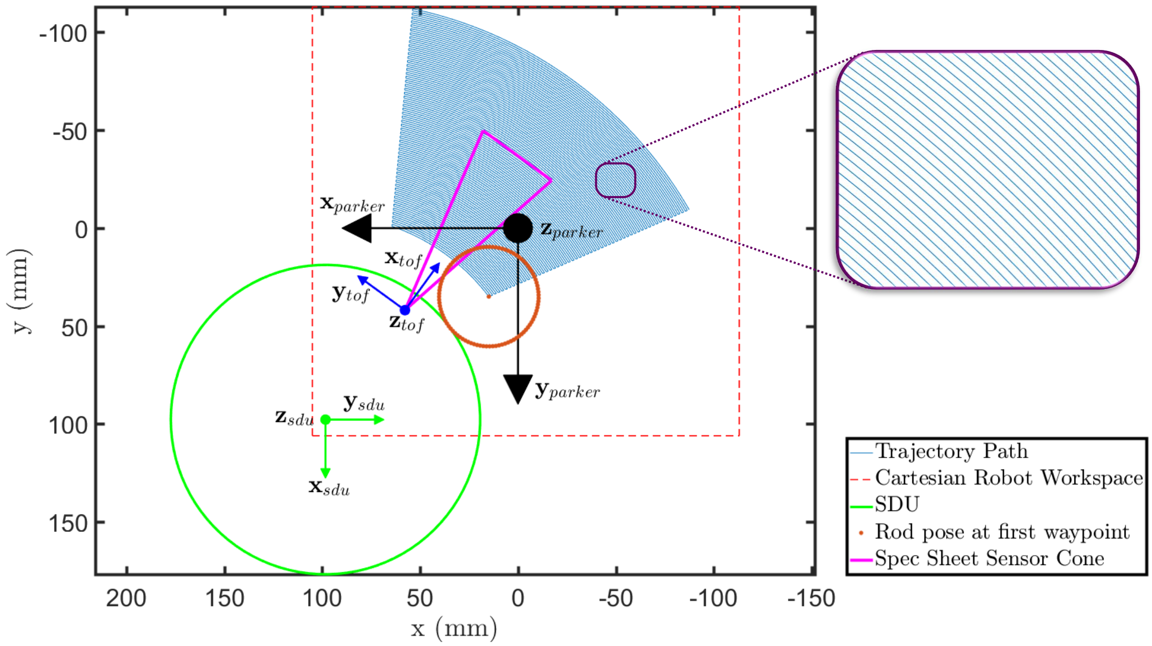

Figure 3.9: Trajectory of the Cartesian stage robot during the ToF sensor characterization experiment.

To determine the sensitivity of the readings to changes in color and reflectivity, the experiment was repeated with three types of Delrin rods: a bare glossy black rod, a rod covered with matte black tape, and a rod covered with a matte light-blue tape. These three tests were performed on two different sensors to validate repeatability of the results across sensors. For each waypoint, the mean sensor ranging error, e was calculated using (3.3).

$$e = \left(\|\mathbf{p}_{tof} - \mathbf{p}_{rod}\| - r_{rod} \right) - \bar{d} \tag{3.3}$$

where $\mathbf{p}_{tof}$ and $\mathbf{p}_{rod}$ are the positions of the sensor and rod in robot frame, r_{rod} is the radius of the rod, and $\bar{d}$ is the mean ranging measurement at the given pose.

Figure 3.10 reports the results of these experiments in the frame of the ToF sensor (blue frame in Fig. 3.9). Figure 3.10(a) and (b) show the ranging error in a 3D and side views, respectively. The figures show that, within the detection cone of the matte black rod, the errors were bounded between 0.01 mm (axis of the cone) and 12.5 mm (edge of the cone). For the glossy black rod, the errors were bounded between 0.019 mm and 15.6 mm. It

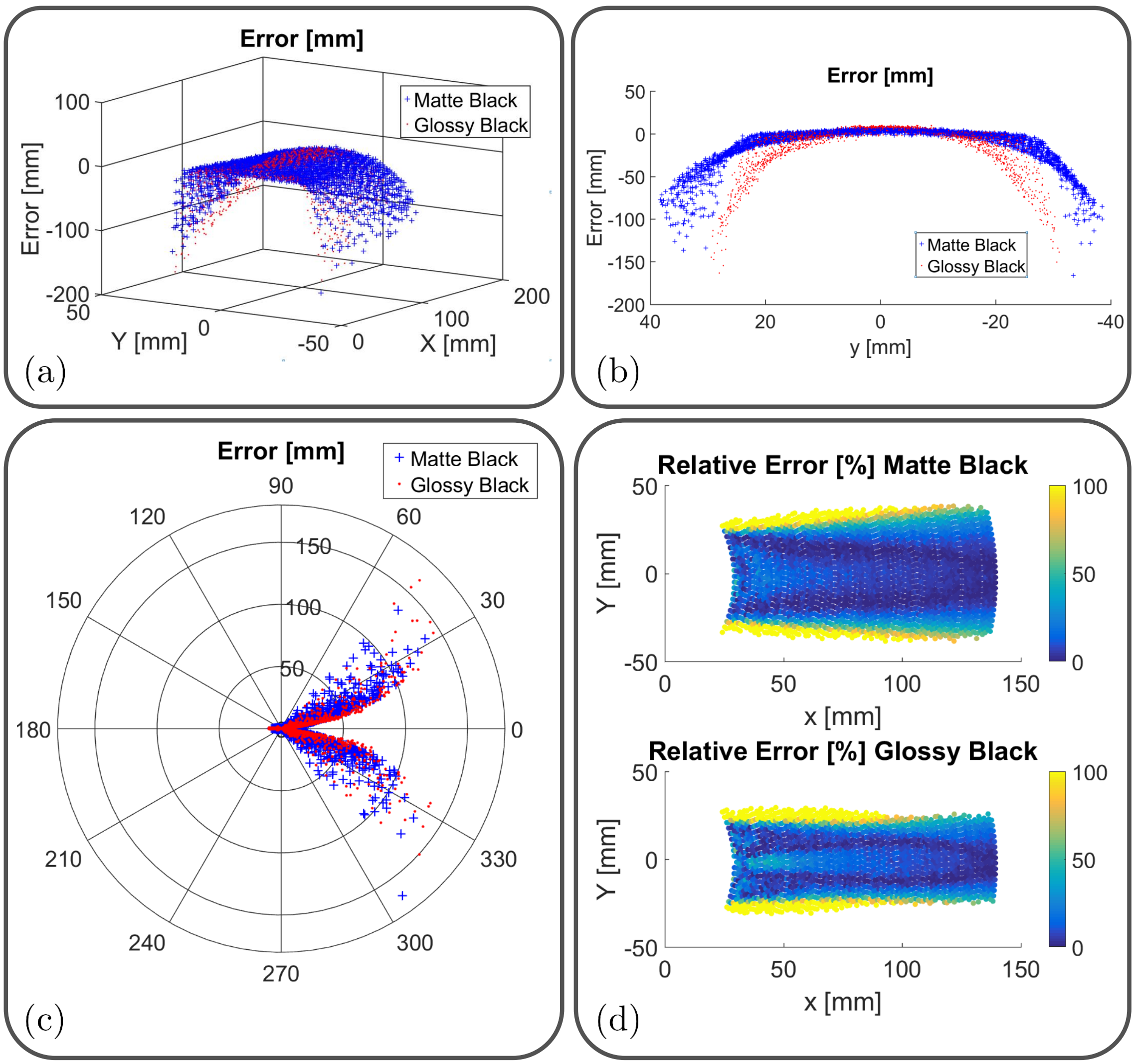

Figure 3.10: ToF sensor characterization results: (a) 3D plot of sensor error for matte and glossy rods, (b) side view of 3D sensor error, (c) polar plot of absolute error as a function of line of sight angle of the detected object, (d) relative error colormap. Figure reproduced from [1].

is also noticeable that the ToF sensors exhibited less error when detecting the matte black surface. Figure 3.10(c) illustrates the ranging errors on a polar plot. From this figure, the detection cone angle was found to be $\pm 11.9°$ for the glossy black rod and $\pm 16.5°$ for the matte black rod. Figure 3.10(d) shows the colorbar plots for the relative error in the ranging value on top. This figure shows that the ToF sensors can detect the rods accurately up to 130 mm, even though their nominal range is 100 mm. These plots also show qualitatively the effects of surface reflectivity on the error. It can be seen the glossy reflecting surface decreased the width of the detection cone. The results reported in Fig. 3.10 are that of one sensor and one rod color. The experiments with the Delrin rod covered with matte blue tape showed similar results and were omitted for space considerations.

3.4 Mapping and Bracing with a single SDU

The performance of the SDU was evaluated on a PUMA 560 industrial robot using a custom real-time controller running on Simulink Real-time. This robot was used for the tasks of mapping an environment and bracing against a surface. The SDU was mounted on the output flange of the manipulator, while the microcontroller/ethernet board reading the sensor ring data was mounted on the robot's "forearm" link. The SDU data, which includes the ToF ranges and the magnetic sensor readings, was sent via user datagram protocol (UDP) to a MATLAB script that generated desired end-effector poses or twists depending on the task. A computer running MATLAB Simulink Real-Time received the desired end-effector poses/twists and commanded motor voltages in real-time at 1 kHz using computed torque control.

3.4.1 Finding Admissible Bracing Surfaces

In an unstructured environment, the ToF sensors on the sensor ring can be used to identify suitable surfaces for bracing. To this end, we show an experiment where the ToF sensor were used to identify planes of interest. The PUMA was controlled in task space using a resolved-rates algorithm to move slowly along a straight line while twisting the end-effector $\pm$ 90°and recording range data from all ToF sensors. In the future, continuum robots equipped with SDUs will be able to achieve this rotation using coordinated control of their backbones to achieve rotation about their backbone as was demonstrated in miniature continuum robots [114, 117].

The scanned geometry was a wooden planar surface with a small wooden block placed as shown in Fig. 3.11 (a) and (c). The resulting point cloud is shown in Fig. 3.11 (b). We applied a random sample consensus (RANSAC) based plane-extraction method as implemented in MATLAB's pcfitplane function, which is an iterative method to estimate the parameters of a potential geometry model in the generated point-cloud data. With prior knowledge that the geometry being scanned was horizontally placed, we fit the surface onto a plane with a plane-normal vector of $\boldsymbol{v} = [0,0,1]$. We then ignore the points already assigned to a plane and continue to fit other planes with the remaining points.

Figure 3.11(c) shows green data points that were assigned to one plane and red data points that were assigned to a second plane. As part of our experiment, our goal was to identify a surface with a continuous planar area of at least 150 mm $\times$ 150 mm. This criterion was defined as a safety measure to protect the SDU's from resting on small corners/thin beams that may be present in a semi-structured environment. Using this criterion, the green surface was identified as a suitable surface for bracing while the red surface was inadmissible.

3.4.2 Utilizing Multi-modal Sensing for Bracing

The PUMA 560 (with the SDU attached) was also used to demonstrate the utility of the proposed SDU for robotic bracing against an environment. In addition to using the Hall effect touch sensors to stop the robot's motion when contact was detected, the proximity sensors were used to reduce the robot's velocity as the bracing surface was being approached. This multi-modal sensing capability can reduce risk to the environment and

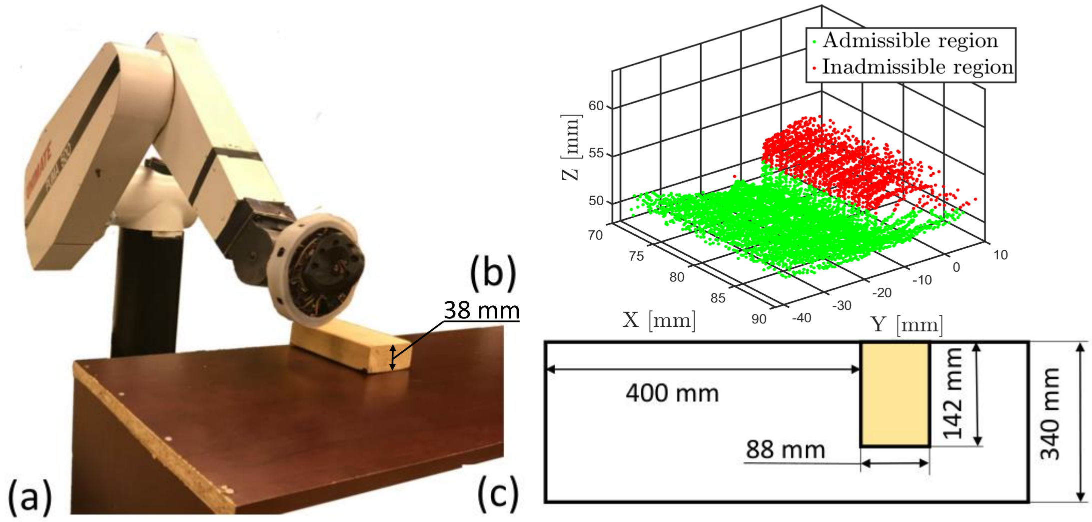

Figure 3.11: Scanning experiment: (a) the PUMA robot scanning with the sensor disk, (b) point cloud results after scanning, and (c) dimensions of geometry being scanned.

humans when there is significant uncertainty in the environment.

The bracing surface was the same flat surface used in the mapping experiments above, but without the additional wooden block. The end effector was first initialized to a pose above the surface with the disk aligned to be normal to the surface (Fig. 3.12 (a)). The robot was then commanded to move downward while using the ToF sensors to regulate its velocity according to:

$$\|\boldsymbol{v}\| = \begin{cases} \frac{d_e}{d_{max}}(v_{max} - v_{min}) + v_{min} & d_e < d_{max} \\ v_{max} & d_e \geq d_{max} \end{cases} \tag{3.4}$$

$$d_e = d\cos(\theta) \tag{3.5}$$

where $\|\boldsymbol{v}\|$ is the norm of the velocity vector, d_e is the estimated distance to the surface, d is the measured distance from the ToF sensor nearest to the surface, θ is the angle of the ToF sensor relative to the surface normal, and d_{max} is the absolute maximum distance the sensor can detect. By reducing the velocity as d_e approaches zero, the touch sensors are able to more precisely detect the instance of contact. In the experiment, we set $v_{max} = 50$ mm/s and $v_{min} = 0.25$ mm/s. Once contact was detected on a magnetic sensor, the motion was stopped (Fig. 3.12(b)). At this instant, the constrained instantaneous kinematics becomes:

$$\dot{q} = \mathbf{J} \begin{bmatrix} [\mathbf{r}_c]^{\times} \hat{z} \\ \hat{z} \end{bmatrix} \omega_z \tag{3.6}$$

where $\dot{q}$ is the vector of joint speeds, $\mathbf{J}$ is the robot's geometric Jacobian, $[\mathbf{r}_c]^{\times}$ is the skew-symmetric form of the vector from the center of the sensor ring to the point of contact, $\hat{z}$ is the unit vector normal to the SDU, and ω_z is a scalar angular velocity about $\hat{z}$. The kinematics in (3.6) reduces the manipulator's task space to a one degree-of-freedom no-slip roll motion. After making contact, we commanded the robot to move back and forth along the surface according to the kinematics in (3.6). Video snapshots from the multimedia extension showing this experiment are shown in Fig. 3.12.

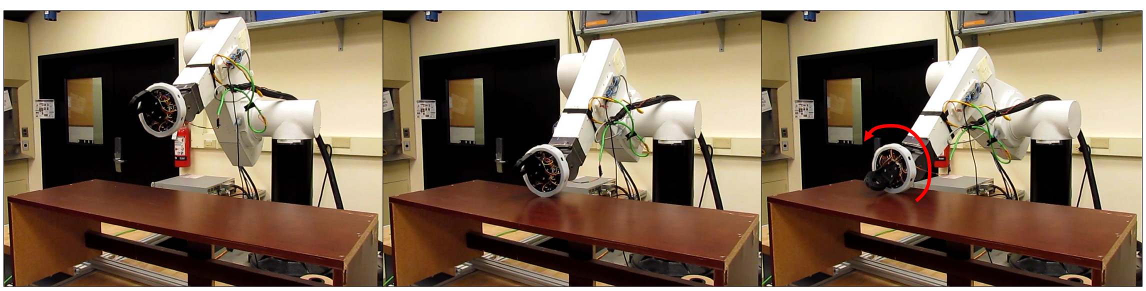

(a) (b) (c)

Figure 3.12: Video snapshots showing (a) approaching the bracing surface, (b) detecting contact using magnetic sensors, and (c) no-slip rolling along the surface.

3.5 Mapping with Continuum Robots

To illustrate the utility of the SDUs for enabling active mapping using continuum robots, we carried out an experiment using the setup shown in Fig. 3.13. While a stationary SDU has blind spots due to the spatial allocation of the sensors, the motion SDUs along a continuum robot enables a full sweep of target objects within the workspace of the robot. The experimental setup includes a custom continuum segment with a length of

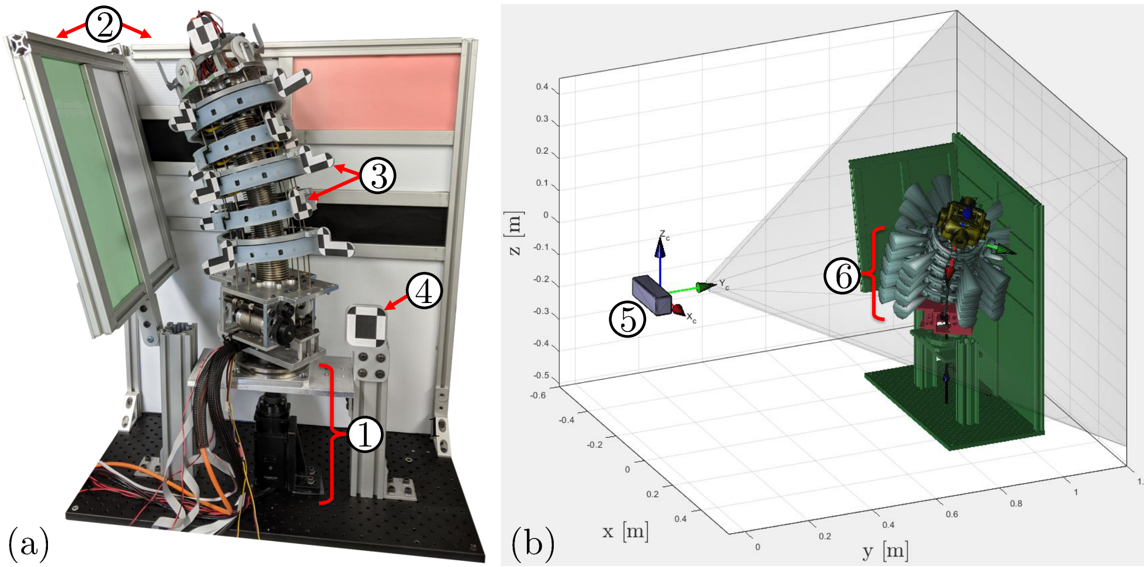

Figure 3.13: Mapping experiment: a continuum robot with integrated SDUs is mounted on rotary stage ① and commanded to roll and bend in different configurations in order to obtain a map of a mock confined space ② using the distributed ToF sensors. Custom markers are mounted on each SDU ③ and at the base of the robot ④, and tracked by a ClaronHD^{TM} optical tracker ⑤. The detection cones of the ToF sensors are shown in ⑥.

370 mm and an outside diameter determined by the diameter of the SDUs (158 mm). This continuum segment is meant to be part of a multi-segment continuum robot that will operate in confined spaces. Each continuum segment achieves bending in two distinct planes, using an actuation unit at its base. Using coordinated pulling and relaxation of wire ropes, the central backbone is bent to achieve an approximately circular bending shape. To endow the setup with more motion capability for the mapping task, we mounted the continuum segment on a revolute joint that is coaxial with the continuum segment's central backbone. This architecture allows the continuum segment to roll about its central backbone while bending in different planes by using synchronized actuation of its wires, according to the constant-curvature kinematic model presented in [18]. The control code for this trajectory was executed at 100 Hz.

Three markers were affixed around the circumference of each SDU to ensure that at least one marker frame is always detected by the ClaronHD^{TM} H3-50 optical tracker. This tracker allows frame detection with an rms error of 0.2 mm within its workspace. For this experiment, the optical tracker collected frame information at 8.08 Hz.

The robot was placed inside a mock confined space comprised from $80/20$ Aluminum extrusions and poster boards partially covered with felt and colored paper. To span the confined space, the robot was commanded to simultaneously bend in a given plane (± 0.02 rad/s), spin to update the orientation of its bending plane (± 0.1 rad/s), and roll about its central backbone (± 0.1 rad/s). During this motion, sensor data from the SDUs is read by the microcontroller, sent to a Robot Operating System (ROS) interface via UDP, published as *rostopics*, and stored using the *rosbag* functionality. The motion rates of the robot during the data collection potentially have some effect on the geometry mapping using ToF sensors, because communication with the sensors is executed at 4.26 Hz. The effect of these motions on the resulting map geometry and means to rectify the mapped model will be a subject of future work, and will remain outside the scope of this contribution.

The proximity data is recorded with respect to a frame $\{s\}$ located at the top surface of each ToF sensor and the MicronTracker information is used to calculate the transformation between the sensor frame $\{s\}$ and the world coordinate frame $\{0\}$ at the base of the continuum robot (④ in Fig. 3.13). This transformation is given by:

$$^{0}\mathbf{H}_{s} = \left({}^{c}\mathbf{H}_{0}\right)^{-1}\,{}^{c}\mathbf{H}_{m}\,{}^{m}\mathbf{H}_{d}\,{}^{d}\mathbf{H}_{s} \tag{3.7}$$

where $\{c\}$ is the frame of MicronTracker camera ⑤, $\{m\}$ is the frame of the marker on an SDU ③, and $\{d\}$ is the frame at the center of an SDU. Note that ${}^{c}\mathbf{H}_{0}$ and ${}^{c}\mathbf{H}_{m}$ are obtained from MicronTracker data, while ${}^{m}\mathbf{H}_{d}$ and ${}^{d}\mathbf{H}_{s}$ are extracted from the CAD model.

3.5.1 Ground Truth Map of the Confined Space

A Faro Fusion arm was utilized to obtain the ground truth map of the confined space. First, the Faro hard probe was used to digitize three intersecting planes at the top right corner of the base marker (④ in Fig. 3.13). The reference frame defined by these three

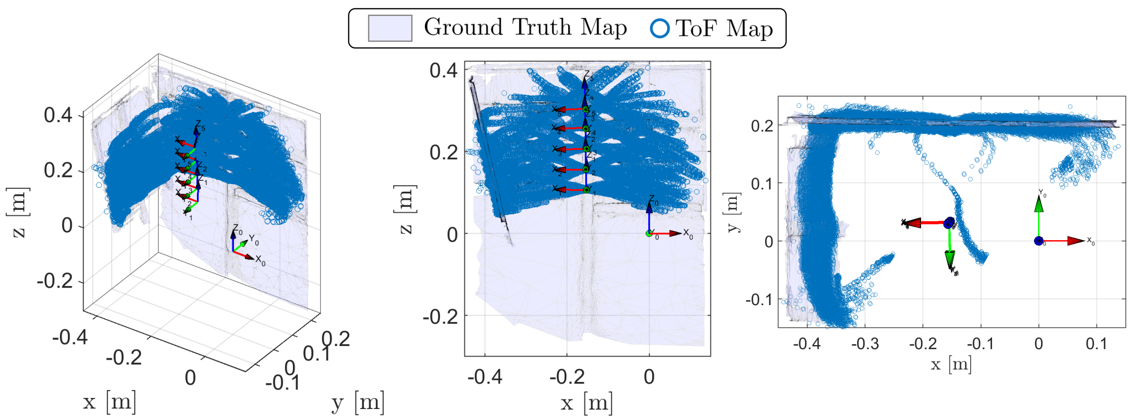

Figure 3.14: Mapping results -(a) isometric, (b) front, and (c) top views - showing the ToF map obtained using the SDUs along the continuum robot, along with the ground truth map scanned using a Faro Arm.

planes served to register the Faro arm to the base frame $\{0\}$ of the continuum robot. Next, the Faro's laser scan feature was used to digitize the inner surface of the fabricated confined space. The resulting STL model is shown in Fig. 3.14.

The Faro map consists of four main planes Aluminum Vertical - ALV, poster board vertical - PBV, Aluminum slanted - ALS, and poster board slanted - PBS, with a 9.25 mm offset between the aluminum and poster board surfaces. The normal vectors to these planes were measured from the STL of the Faro scan, relative to the base frame $\{0\}$: $\hat{\mathbf{n}}_1 = [0,1,0]^T$ for the vertical planes and $\hat{\mathbf{n}}_2 = [0.98,0,0.22]^T$ for slanted planes. These four ground truth planes (as shown in Fig. 3.15) are used to evaluate the mapping performance of the ToF sensors.

3.5.2 ToF Map of the Confined Space

The proximity data captured by the ToF sensors during the motion of the continuum robot resulted in an experimental map of the confined space. This map, which we refer to as "ToF map", is illustrated in Fig. 3.14. We compared the ToF map to the ground truth planes described in the previous section. To do so, we split the raw ToF map into four regions, corresponding to the four ground truth planes. First, we split the ToF map into a vertical set and a slanted set, using MATLAB's *pcfitplane*, which is a random sample consensus (RANSAC) algorithm that estimates the parameters of the plane for a given point cloud. Additional inputs to this function are the maximum distance from an inlier point to the plane and a reference orientation constraint. We set the maximum allowable distance to be 40 mm and used the normals of confined space walls ($\hat{\mathbf{n}}_1$ and $\hat{\mathbf{n}}_2$) as reference vectors. Next, the resulting two ToF sets are further split into the poster board set and the Aluminum set by projecting onto both planes and electing the closest plane as the parent plane. The resulting four ToF map sets are shown in Fig. 3.15, along with the parent ground truth planes.

This classification was used to calculate the RMS error, such that the residuals are the orthogonal projection of each point to its parent ground truth plane. The resulting ToF mapping error was 9.73 mm. While a more thorough methodology for quantifying the mapping error could be used by borrowing from the literature of point cloud to rigid body registration, we believe that such analysis should be carried out after the mapping model rectification has been implemented to counteract the mapping artifacts included by the kinematics of the motion of the SDUs while collecting the ToF data. In addition, the use of the MicronTracker to track the shape of the continuum robot introduces tracking artifacts, due to lighting conditions and the reflectivity of the markers. The video extension shows that in some instances, one of reconstructed SDU frames deviates from the spline of the central backbone. This source of error will be eliminated once the kinematics of the continuum robots are calibrated using integrated shape sensing elements, which will be the subject of future studies with this continuum robot.

3.6 Human-Robot Interaction

3.6.1 Single SDU on PUMA

Using the same programmed motion described in Section 3.4, we also demonstrated the use of the SDU to detect human contact. Figure 3.16 shows video snapshots of this experiment taken from a multimedia extension, showing the robot moving with constant

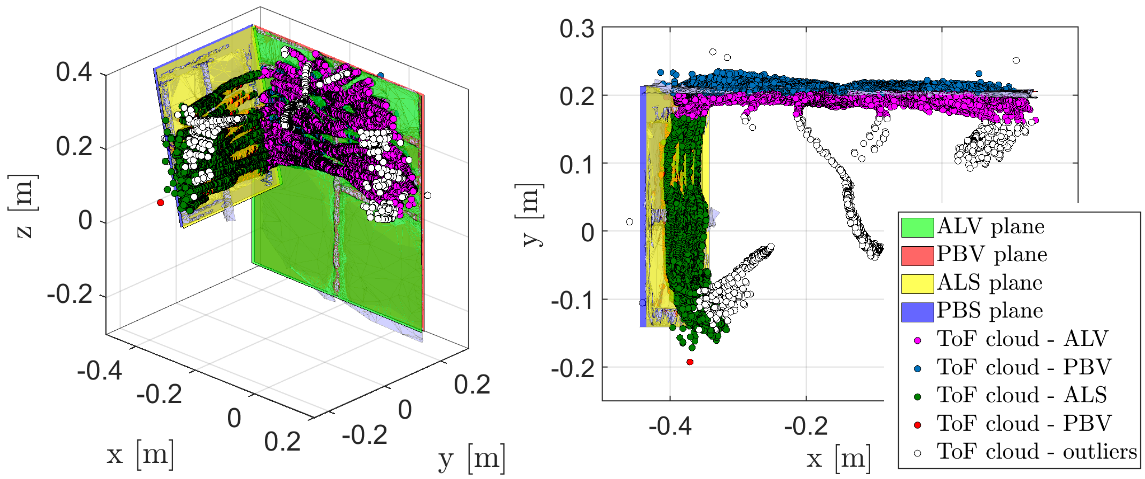

Figure 3.15: ToF point clouds sorted by proximity to ground truth (ALV, PBV, ALS, PBS) planes.

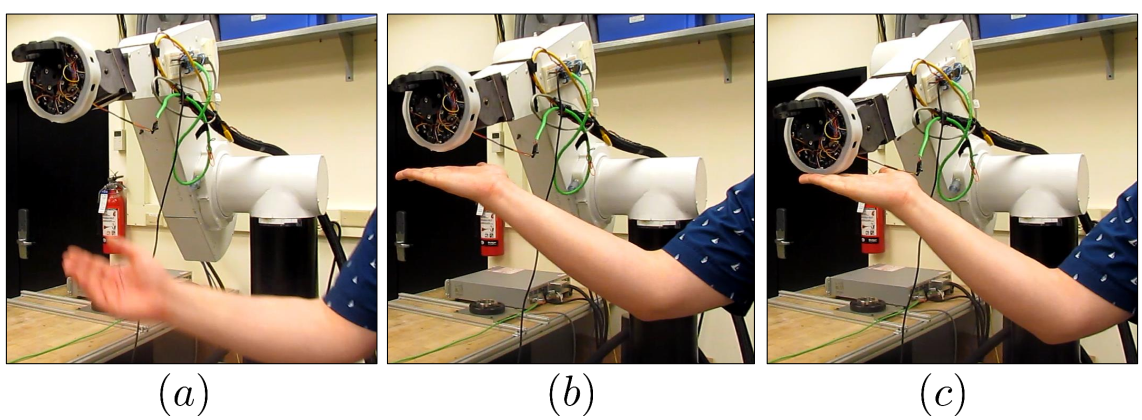

Figure 3.16: Video snapshots showing (a) robot moving with constant velocity, (b) slowing down near human contact, and (c) stopping motion after detecting contact.

velocity and detecting human contact using one of its Hall effect sensors. The ability to detect contact is limited for a single disk.

3.6.2 SDU Array on Continuum Robot

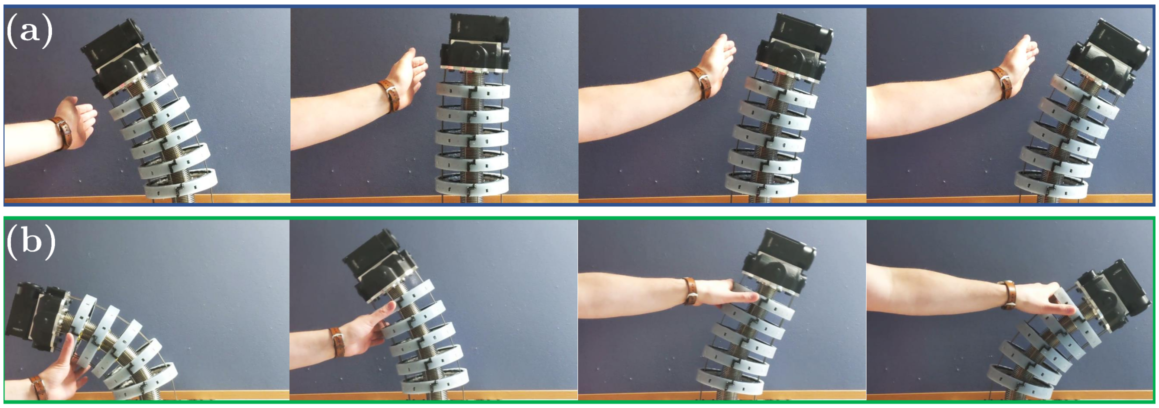

Figure 3.17: Video snapshots of two active compliance human-robot interaction modes: (a) Contact-less using time-of-flight sensors (b) Contact-based using Hall effect sensors.

The continuum robot described in Section 3.5 was also used to demonstrate the two modes of human-robot interaction (contact-less and contact-based) supported by the SDUs. For this experiment, the robot was mounted on a static base and sensors from the top SDU were used for active compliance motion control. Multimedia extension I shows these two modes of operation. Also, Fig. 3.17 shows video snapshots of this multimedia extension.

In Fig. 3.17a shows the contact-less interaction mode where the robot moves away from a user's hand using the ToF sensors. For this behavior, we selected two ToF sensors on the right and left sides of the segment and commanded the velocity of one motor according to:

$$v_m = \gamma(d_r - d_\ell) \tag{3.8}$$

where v_m is the velocity of the motor, γ is a manually-tuned gain, and d_r and d_ℓ are the distances measured with right and left ToF sensors, respectively.

Figure 3.17b shows the contact-based interaction mode where the robot moves based on sensed contact using the Hall effect sensors. For this behavior, we similarly selected two

Hall effect sensors on the right and left sides of the segment and the velocity of the motor is commanded according to:

$$v_m = \gamma \left(\Delta B_{z,r} - \Delta B_{z,\ell} \right) \tag{3.9}$$

where $\Delta B_{z,r}$ and $\Delta B_{z,\ell}$ are the changes in the magnetic flux density measured along the z axis of the sensors on the right and left sides, respectively.

These simple control laws demonstrate the potential of our proposed multi-modal sensing disks for human-robot interaction along the body of a continuum robot.

3.7 Discussion

Table 3.1 summarizes the key performance measures of our proposed multi-modal sensing architecture. The proximity data obtained from the distributed ToF sensors resulted in a map of the environment, accurate to 9.73 mm. The accuracy of the mapping was influenced by the ToF sensor data and by latency-induced motion artifacts due to the slow acquisition speed from the optical tracker we used to determine the spatial pose of each SDU. With an acquisition rate of 8.08 Hz, a motion speed of ± 0.1 rad/s, and optical markers located at a radius of 108.5 mm from the central backbone, the latency-induced position uncertainty is 1.343 mm. In the future, we anticipate using real-time shape sensing of the continuum segment to overcome the need for tracking the SDUs. Such shape sensing may be obtained using fiber-Bragg grating curvature sensors.

The mapping error we obtained is also influenced by the low data acquisition speed of the ToF sensors. While one could speed up the overall acquisition rate for a continuum segment to be closer to 20.4 Hz by using individual micro-processors for each SDU, faster ToF sensor technology is needed to allow faster acquisition rates for more accurate mapping and for safer human-robot interaction. Since the uncertainty of mapping depends on the motion being carried out by the robot, future works will need to investigate the effects of the robot's motion on the mapping performance and to optimize the motion of the robot for minimal uncertainty mapping results.

ToF detection error	Matte surface along cone axis: 0.1 mm Matte surface at cone edge: 12.5 mm Glossy surface along cone axis: 0.019 mm Glossy surface at cone edge: 15.6 mm
Hall sensor F-linearity:	$4.52\% \pm 0.56\%$
Communication Frequency	1 SDU: 20.4 Hz (ToF & Hall sensors) 5 SDUs: 4.26 Hz (ToF & Hall sensors)
Mapping RMSE:	9.73 mm†

† Result is influenced by 8.08Hz optical tracker acquisition frequency and the motion of the optical markers

Table 3.1: Summary of performance characteristics

3.8 Conclusion

Human-robot collaboration in confined spaces requires the use of continuum robots with whole-body situational awareness. To address this need, we developed sensing disk units (SDUs) that integrate into the body of continuum robots and endow them with a) mapping, b) proximity sensing, c) contact detection and localization, and d) force sensing capabilities. This chapter presented the detailed design and fabrication of the SDU components, along with the communication protocol required to interface with an array of SDUs.

Experimental evaluation showed a linear and repeatable relationship between the magnetic flux density and the external force applied, with each Hall effect sensor having its own magnetic flux density bias. Results for the ToF sensors also showed that matte surfaces are detected more accurately and with a wider detection cone than glossy surfaces and that the color of the detected object was not significant.

Experiments on an industrial manipulator demonstrated the use of a single SDU for preliminary mapping a mock environment, identifying potential bracing surfaces, and utilizing the multi-modal sensing capabilities to establish a bracing contact against an environment.

Finally, a continuum robot with five SDUs was used to demonstrate the utility of whole-body sensing for active mapping and human-robot collaboration. We believe that this work is a significant step towards a novel class of continuum robots that can be deployed in confined spaces, intelligently interact with their environment, and safely assist a co-located worker.

CHAPTER 4
SELF-STEERING CATHETERS FOR NEUROENDOVASCULAR INTERVENTIONS

This chapter is adapted in part from "Image-Guided Optimization of Robotic Catheters for Patient-Specific Endovascular Intervention" published in "2021 International Symposium on Medical Robotics (ISMR)" and has been reproduced with the permission of the publisher and my co-authors Rohan Chitale and Nabil Simaan © 2021 IEEE.

4.1 Background and Motivation

Stroke is the leading cause of permanent disability, second leading cause of dementia, and third leading cause of death world-wide [36, 118]. In the United States, $795,000$ people per year have a new or recurring stroke [36]. About 87% of strokes are ischemic [119] and 10% of ischemic strokes are due to large vessel occlusions (LVO) [120]. Without treatment, 80% of patients with LVO suffer from a disabling or deadly stroke [37]. Despite being a small portion of strokes, LVO strokes account for a disproportionately large economic burden and death [121, 119]. In stroke management, the strongest predictors of a good clinical outcome are the speed and extent of recanalization. Studies have shown that each additional 10 minutes of ischemic time (time from onset of thrombus blockage to recanalization) correlate with 40 days of added disability to the patient, and a $10,000 increase in economic burden [81].

Since 2015, mechanical thrombectomy (MT), i.e. the endovascular retrieval of blood clots using stent retrievers and/or aspiration catheters, has become the standard of care for patients who present with acute LVO strokes. This shift stemmed from multiple randomized controlled trials [38, 39, 40, 41, 42, 43] that showed the benefits of MT in reducing stroke burden. Patients treated with MT achieved recanalization rates up to 88% and had reduced disability rates (modified Rankin scale improved by up to 50%) at 90 days post-treatment. The advantage of MT over r-tPA intravenous thrombolysis alone (previous standard of care) was strong enough to justify ceasing patient enrollment in some of these clinical trials due to ethical concerns for the patients in the control group [38, 40, 41].

The rise in awareness of the importance of MT stands in contrast to the availability of this type of intervention in large portions of the U.S. geography. There is a shortage of specialized neuro-endovascular physicians [44] – especially in rural and semi-urban regions [122, 123]. Despite the availability of 5,000+ hospitals, there are only an estimated 800 to 1,100 neuro-interventionalists in U.S [124]. This shortage results in the need for interhospital transfers from smaller hospitals to thrombectomy-capable centers, which significantly increases ischemic time. Recent studies showed that the average inter-hospital transfer adds more than 100 minutes of ischemic time and results in a lower chance of a good functional outcome [16, 45, 46].

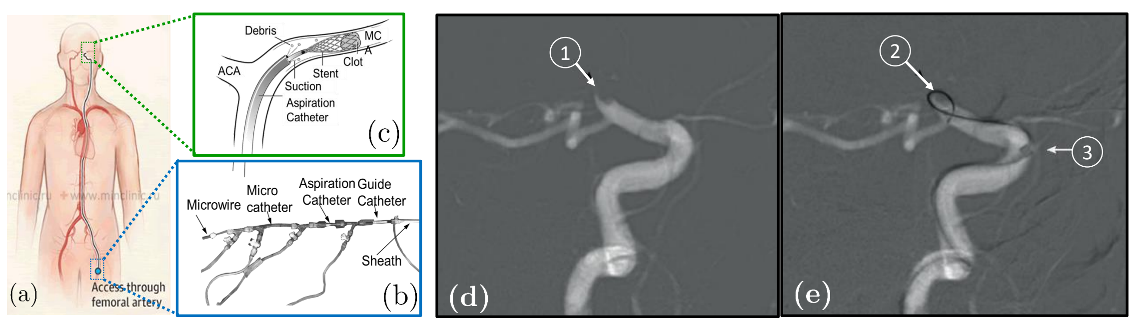

Figure 4.1: (a) Femoral artery access for mechanical thrombectomy, (b) stacked catheters for intravascular navigation, (c) stent retriever and suction deployed at site of occlusion. (d) Roadmap of the left ICA showing clot position ①, which is deduced from absence of contrast in a normally continuous blood vessel, (e) navigation roadmap used as a static background on which live fluoroscopy is overlaid: the microwire ② is used to navigate the tip of the aspiration catheter ③ to the clot site. Images adapted from [2, 3].

The lack of access to MT stroke care ([125]) and the shortage of neurointerventionalists can partially be attributed to the technical complexity and cognitive load required to navigate through thin, tortuous, and branched vasculature using passive guidewires and catheters. Figure 4.1 illustrates the standard MT setup. Neuro-interventionalists use a complex combination of stacked passive catheters (Fig. 4.1(b)) to manually navigate from the entry point at the femoral artery (Fig. 4.1(a)) to the site of occlusion (Fig.

4.1(c)). A contrast agent is injected near the occlusion site to obtain a digital substraction angiogram (DSA) of the target vasculature, using bi-plane fluoroscopy. Fig. 4.1(d) shows a sample roadmap of an occluded left internal carotid artery (ICA) obtained by applying a "SmartMask" filter to a DSA image. The position of the clot ① is deduced from the absence of (white) contrast in a normally continuous vessel. This roadmap is used as a static background against which live fluoroscopy is overlaid (Fig. 4.1(e)). The microwire ② and the tip of aspiration catheter ③ are radio-opaque and visible in real time.

There is a need for dexterous and actively steerable microcatheters for robotic-assisted neuro-endovascular navigation [17]. Such technology has the potential to: 1) increase the speed of neuro-endovascular navigation by providing distal control for steering and branch selection, 2) lower the skill barrier for mechanical thrombectomy to expand access to this time-sensitive procedure, 3) reduce radiation exposure to the surgeon, and 4) enable semi-automation of catheter navigation.

In addition to navigation challenges, surgeons lack sensory feedback about interaction forces at the tip of the catheter. The force sensed by their hands as they advance passive catheters is largely masked by cumulative friction over the catheter's course. This challenge leads to intentional design of flimsy passive guidewires and micro-catheters, which can suffer from large torsional windup. Our proposed robotic catheter includes series elastic elements that provide distal sensing information and enable the catheter tip to actively comply with the vasculature.

The related works section below identifies the scientific needs driving our work in this chapter. Briefly stated, these needs include design miniaturization for a multi-segment articulated continuum catheter for stroke care, lack of sensory tip capability, and lack of self-steering using sensory information.

4.2 Related Works

Previous works on robotic catheters have mostly focused on cardiac (percutaneous coronary) and peripheral vascular applications [47, 51, 49, 48, 50]. The driving forces towards robotic assistance in endovascular interventions have been: a) the need to improve catheter stability and precision, and b) the need to reduce total radiation exposure from fluoroscopy imaging to the patients and the surgeon [126].

Most current commercially available robotic catheter systems have been FDA approved for procedures in cardiology, peripheral vasculature, and lung biopsy:

- The Niobe® robotic magnetic navigation system (Stereotaxis) enables the surgeon to remotely guide the motion of a magnetic catheter (7Fr, 2.33mm) by controlling the orientation of two giant permanent magnets located at each side of the surgical table [52, 127, 128].

- The Monarch Platform (Johnson & Johnson) and the ION (Intuitive) were recently approved for lunch biopsy.

- The Sensei robotic catheter system (Hansen Medical) consists of a tendon-driven outer sheath (14Fr, 4.67mm) that houses standard mapping or ablation catheters. With this system, the surgeon controls the motion of the catheter in 3D via a joystick. The Sensei system has been deployed successfully for interventional electrophysiology procedures [129].

- The Magellan Robotic System (Hansen Medical), a successor of the Sensei system, includes a smaller robotically actuated guide catheter (6Fr, 2.18 mm) for navigation of peripheral blood vessels in a wide variety of endovascular abdominal and cardiovascular procedures [54, 130, 131, 132, 133]. This system has been demonstrated to perform a diagnostic cerebral angiogram [134], but has not been deployed in the MCA nor the intracranial ICA. We believe it to not be suited for cerebral vasculature because its catheter guide has two bends separated by a long straight segment (25 mm) and lacks the ability to bend around sharp corners.

- The Amigo system (Catheter Precision) is an FDA approved system for mapping and ablation of various arrhythmias. This system enables the remote control (insertion/withdrawal, roll, and tip deflection) of standard electrophysiology (EP) catheters [55].

- The CorPath 200 (Corindus/Siemens) is an FDA approved system for remote control of guidewires and balloon/stent devices during percutaneous coronary interventions (PCI) [135, 17, 136]. This system is also being investigated for use in neuroendovascular applications and was recently tested (first-in-human) for robotic-assisted carotid stenting, cerebral angiogram, and stent-assisted coil embolization of an aneurysm [137, 138, 139]. While this system shows promise for future remote stroke thrombectomies, the following limitations were reported: a) the system does not provide force sensing nor haptic feedback needed to traversing delicate, tortuous anatomy, b) some procedures had to be converted back to manual approach due to difficulty in navigating aortic arches in alternative geometry (bovine arch), c) the system is unable to drive microcatheters and guides wires and lacks attributes for complex intracranial procedures.

Commercial systems that potentially meet the size constraints for neuronavigation include the SwiftNinja (Merit Medical) [57] and Bendit (Bendit Technologies). Both microcatheters aim to eliminate the use of guidewires in endovascular navigation by enabling steering of a microcatheter using a manual dial. The SwiftNinja (2.4 F, 0.8mm) was recently cleared by the FDA and has demonstrated utility in coronary and peripheral applications [140, 141, 142]. However, these systems are not suitable for neuronavigation because they have planar single degree of articulation, which would hinder the navigation of the tortuous geometry of the carotid syphon.

In addition to commercially available devices, many steerable catheter prototypes have been proposed by research groups. Common actuation strategies include magnetic actuation [64, 143], thermal actuation with shape memory alloys [59, 62, 60, 63] and conducting polymer actuators [58], hydraulic actuation [144] and electromechanical actuation with tendons [126, 65, 67, 145, 146] and friction wheels [61]. Fagogenis et al. recently developed a 6-DoF catheter comprised of three concentric pre-curved tubes (2.77 mm) that utilizes haptic vision for automated steering into a beating heart [67]. From a design perspective, the closest work to our proposed catheter design is a robotically actuated 2-DoF guidewire in [66], which consists of a miniature steerable flexure-based catheter actuated with internal routing of tendons to limit cross talk between segments. Our actuation principle is closest to [147] where notched concentric tubes have been used to generate a 7.5 mm diameter actively bending continuum segment. In our ongoing and planned research, we overcome some limitations of these two works. The design in [66] uses actuation tendons which conflicts with the need for an uninterrupted bore for delivering stent retrievers. The design in [147] offers an open bore at a very large diameter and does not easily extend to more than one actively bending segment.

In addition to navigation challenges, there is a need for sensing and force feedback during neuroendovascular navigation. Sensing of catheter tip forces has received extensive attention in the literature [27, 69, 70, 71, 72, 73, 74, 75] and point force sensing exists commercially for larger cardiac catheters (e.g. [71, 73]). However, no sensing solutions currently can be used at the scale needed for neuro-endovascular procedures. Furthermore, active compliance control of continuum robots has been sparsely addressed for larger designs (e.g. [79]) and no commercial or research systems have demonstrated active compliance of miniature intravascular catheters.

4.3 Contributions

Figure 4.3 shows an overview of our envisioned system for semi-automated neuro-endovascular surgery. It includes a custom-designed robotic micro-catheter (404), a catheter actuation unit (402) with a quick connect interface to the catheter body and a quick connect mechanism connecting it to a linear insertion stage (403). The linear stage is affixed to a statically-balanced arm (3) that may be easily adjusted by the surgeon and surgical staff. The arm is positioned on a mobile base (2) that rolls into the operating room and may be locked in place by locking its casters.

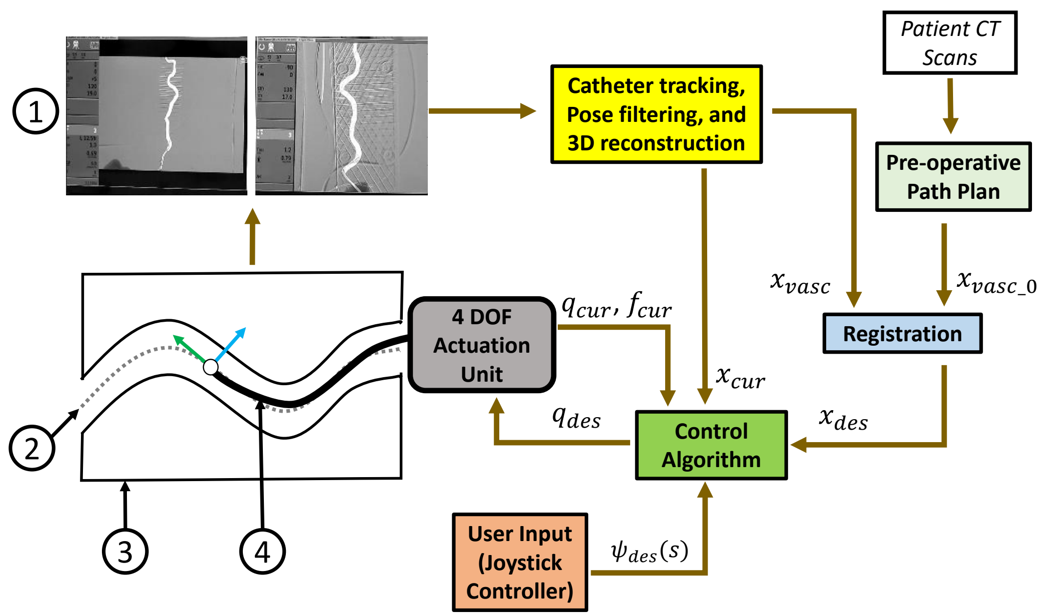

Figure 4.2: Overview of strategy for deployment and close loop control of a catheter in mock neuro-vasculature. ① Bi-plane Fluoroscopy images of the phantom vasculature anatomy, ② Centerline of vasculature phantom used as virtual fixture path, ③ phantom vasculature, ④ Steerable Micro-catheter

.

The system will allow for shared control between the surgeon and the robot, depending of the insertion stage and the geometry of the traversed vasculature (e.g: straight, tortuous, bifurcated). Fig. 4.2 shows an overview of the close loop architecture, with a highlight of technical components needed for safe deployment.

The key contributions presented in this chapter include:

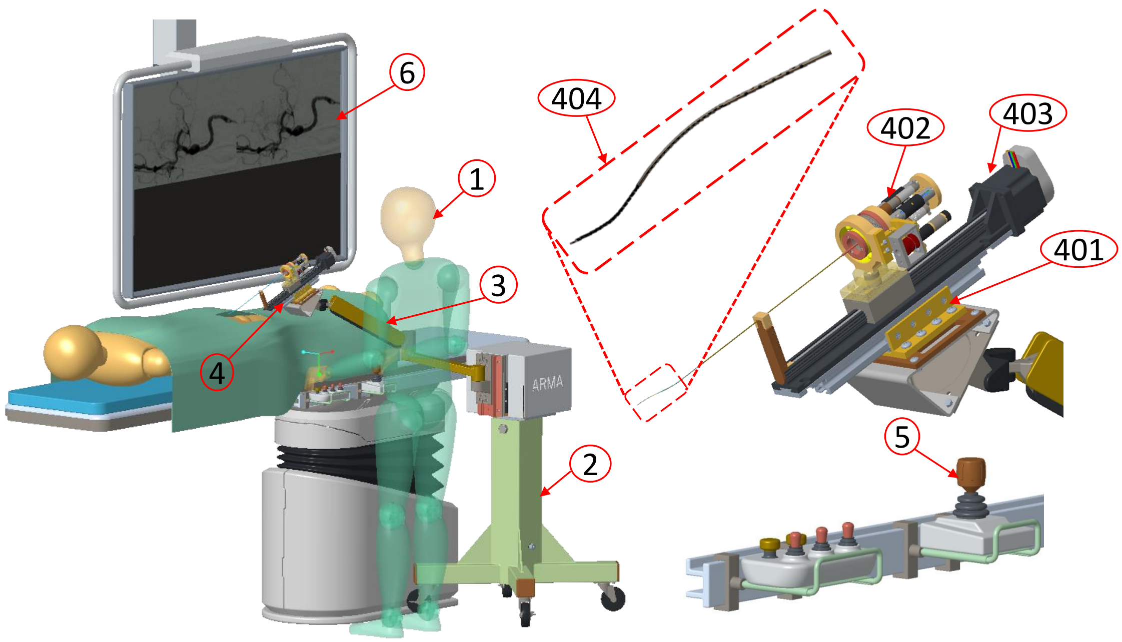

Figure 4.3: Concept of the semi-automated microcatheter system showing surgeon ① and surgical bed, movable cart ②, statically balanced arm ③, catheter insertion robot ④, joystick controls ⑤, fluoroscopy display ⑥. The robot includes: quick connect interface (401), actuation unit (402), insertion stage (403), steerable catheter (404). Note shown: bi-plane fluoroscopy, force/torque load cells for catheter force monitoring

.

- The kinematic modelling and image-based calibration of a novel antagonistic pair catheter
- The design and fabrication of a 4-DOF actuation unit with series elastic elements to interface with the robotic catheter
- A path planning algorithm that uses preoperative CT scan to plan to motion of the robotic catheter in a way that minimizes the shape error
- The first study of optimal catheter design parameters for patient-specific endovascular navigation
- Design, implementation and validation of a multi-mode control scheme for real-time control of the robotic catheter
- Preliminary catheter segmentation and tracking from bi-plane fluoroscopy imaging
- Extended Kalman Filter (EKF) formulation for pose filtering during catheter tracking.

4.4 System Overview

4.4.1 Multi-articulated Robotic Catheter

Figure 4.4 illustrates a Steerable Robotic Microcatheter (SRMC). This system includes two continuum segments which use antagonistic push-pull actuation (such as in [147]) to bend in separate planes. Distal bending is achieved by the linear motion of a notched inner NiTi tube (OD 0.66 mm, ID 0.475 mm) relative to a stationary intermediate NiTi tube (OD 0.89 mm, ID 0.725 mm). Proximal bending is achieved by the linear motion of a notched outer NiTi Tube (OD 1.2 mm, ID 0.95 mm) relative to the same intermediate NiTi tube. The two segments bend in different planes, which allows the device to create spatial s-shapes. The distal segment of the SRMC has a 0.88 mm outer diameter, which matches the size range of current (passive) thrombectomy microcatheters used for stent retriever deployment (e.g.: Marksman, 0.96 mm, Rebar, 0.94 mm), and is smaller than the size range of current (passive) aspiration catheters (e.g.: Sophia 6 Plus, 1.77 mm; ACE 068, 2 mm). This robotic catheter matches the size and articulation constraints for neuronavigation, and also include an open bore (0.475 mm ID) for possible deployment of mechanical thrombectomy tools (e.g. stent retriever).

The actuation unit for the SRMC includes global insertion and roll, in addition to the two bending DoFs. The steerable portion ($L_1 = 22$ mm and $L_2 = 18.8$ mm) of the SRMC is extended to 95 cm by gluing three concentric passive catheter tubing (PTFE) to the tree NiTi tubes. In addition, thick-wall stainless tubing is glued to the other end of the passive catheter tubing to enable mounting to the collets of the actuation unit. To imbue the robotic catheter with joint level force sensing capabilities and active compliance, we designed the actuation unit with series elastic elements. For each bending segment, an active carriage, controlled by motorized lead screw (Velmex, A1506B-S1.5, 4.5" travel, 20 turns/inch), pushes a passive (floating) carriage, via the intermediary of a calibrated spring. Both passive carriages are float the same guide rail (Igus, NS-01-17) and the spring deflections are recorded using linear potentiometers (Honeywell, MLT38000101).

Our current design of the steerable tip is such that the two bending segments are rigidly attached. An alternative design would include an interleaved passive flexure joint, with its compliant axis within the bending plane of the distal continuum segment, and perpendicular to the catheter shaft (as shown in Fig. 4.9). We explore the advantage of adding this passive flexure in a simulation study in Section 4.6.3.

4.4.2 Phantom Vasculature

The internal carotid artery (ICA) is a common site of occlusion in stroke patients, and thus was chosen as our vasculature model. A 3D model of the ICA was obtained by segmenting the CT scan of an anonymized patient in 3DSlicer. First, the *threshold* feature was used to increase the contrast between bone , tissue, and vasculature. Next,

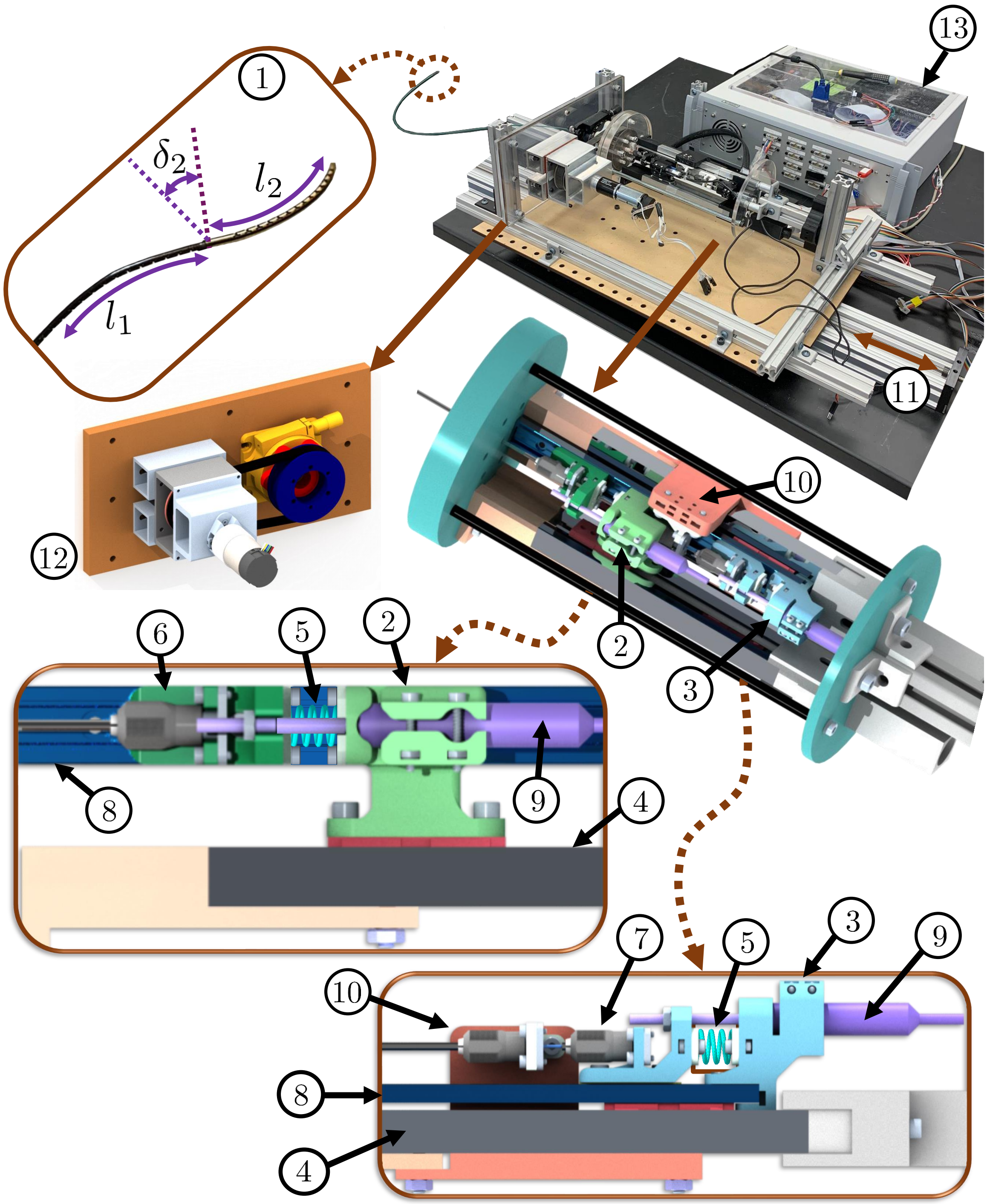

Figure 4.4: The steerable catheter ① uses the relative push-pull motion of three concentric antagonistic superelastic Nitinol tubes to bend in two separate planes. The proximal and distal bending DoFs are achieved by the linear motion of active carriages ② and ③, respectively, which are controlled by motorized lead screws ④. Calibrated springs ⑤ translate this motion to free floating carriages ⑥ and ⑦ with anchored collets, which connect to the outermost and innermost backbones, respectively. A passive rail ⑧, attached to ③, enables near frictionless motion of both floating carriages. Linear potentiometers ⑨ record the spring displacements. The middle backbone is held fixed by a holder ⑩ mounted to guide rails of the distal segment linear slide. In addition to the bending DoFs, the actuation unit includes a global insertion DoF ⑪ and a roll DoF ⑫. The four motors are controlled in real time using Simulink Real-time on a PC/104 target computer ⑬.

the surgeon manually painted section of the ICA visible in each slice. Manual painting achieved superior segmentation quality than the software, because the contrast provided by *thresholding* was insufficient to distinguish bone from vasculature. The resulting ICA model was smoothed in MeshMixer. This process is illustrated in Fig. 4.5.

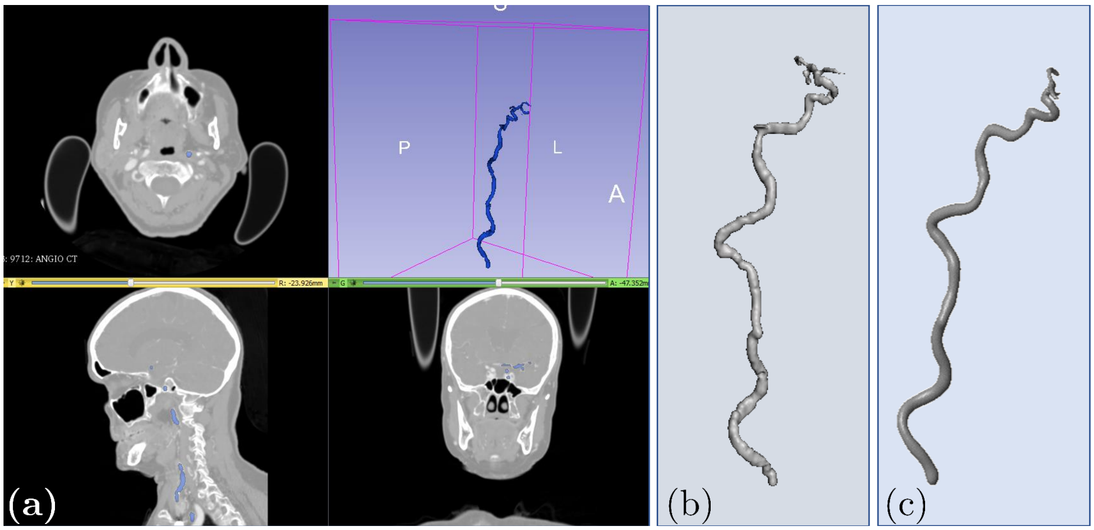

Figure 4.5: (a)3DSlicer view of anonymized patient's CT scan, with segmented ICA. (b) Raw STL of segmented ICA. (c) ICA STL smoothed in MeshMixer.

This ICA model was used for the dual purpose of 1) a preoperative path planning, and 2) the design of phantom vasculature models for experimental evaluation. Fig. 4.6 shows some of the phantom vasculature prototypes that we fabricated. The rigid vasculature (a) is fabricated out of PLA filament using 3D printing. The hybrid vasculature (b) consists of a rubber tubing (3.175 mm ID, 6.35 mm OD) mounted on a 3D printed based that follows the outline of the ICA. The soft vasculature (c) was fabricated by dip-coating liquid silicone rubber (Ecoflex 00-30) on a sacrificial 3D printed wax model of the ICA. Our latest 3D model was fabricated with polyjet 3D printing, which consists of spraying small droplets of liquid photopolymer in layers that are instantly UV cured. Our prototype was printed with a polymer of 50A durometer (508 psi tensile strength), which approximates the softness of the ICA. This model extends beyond the ICA, to include the aortic arch and alternative arterial branches.

For path planning purposes, the STL point cloud obtained from the CT scan (Fig.

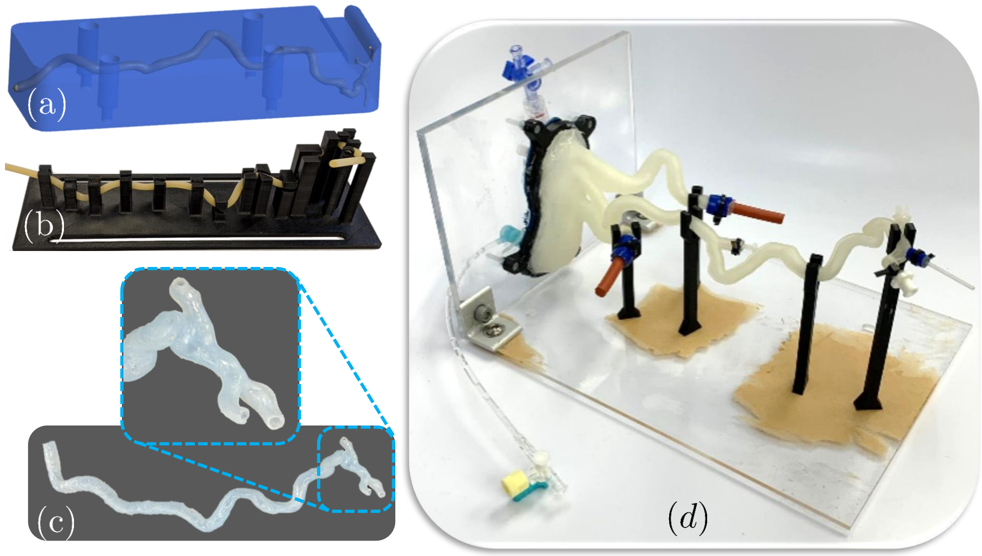

Figure 4.6: Phantom vasculature models (a) 3D printed model with a cavity shaped like the ICA model. (b) Hybrid 3D printed and latex phantom ICA vasculature model. (c) Silicone model fabricated using sacrificial wax printing followed by intermittent dipping in silicone. (d) 3D printed polyjet 50A elastomer model.

4.5(b)) was parameterized into a set of equidistant points separated by arc-length ds. First, the principal direction of the point cloud was determined using singular value decomposition and principal component analysis (PCA). Next, vertices were clustered into equidistant subsets, along the direction of the PCA data line. Each cluster was projected onto a local best fitting plane, and the local mean of the projected points was calculated. Finally, a spline was fitted through all mean vertices from the clusters and the spline points were resampled to obtain equidistant vertices, with arc length separation ds (Fig. 4.7(b)). Figure 4.7(c) shows some of the local tangents along the vasculature.

The 3D orientation of the vector between two consecutive vertices along the curve is a function of the angles α and β, such that ${}^0\mathbf{R}_2 = {}^0\mathbf{R}_1\,{}^1\mathbf{R}_2 = e^{\alpha[\hat{\mathbf{z}}\times]}e^{\beta[\hat{\mathbf{y}}\times]}$ where $[\mathbf{a}\times]$ designates the cross-product matrix form of the vector $\mathbf{a}$. The angles of rotation α (yaw) and β (pitch) are defined in Fig. 4.8, and calculated using the 3D coordinates of the consecutive points along the vasculature.

Let $\hat{\mathbf{z}}_2$ be the direction vector between two consecutive points $\mathbf{x}_i$ and $\mathbf{x}_{i+1}$ along the vasculature:

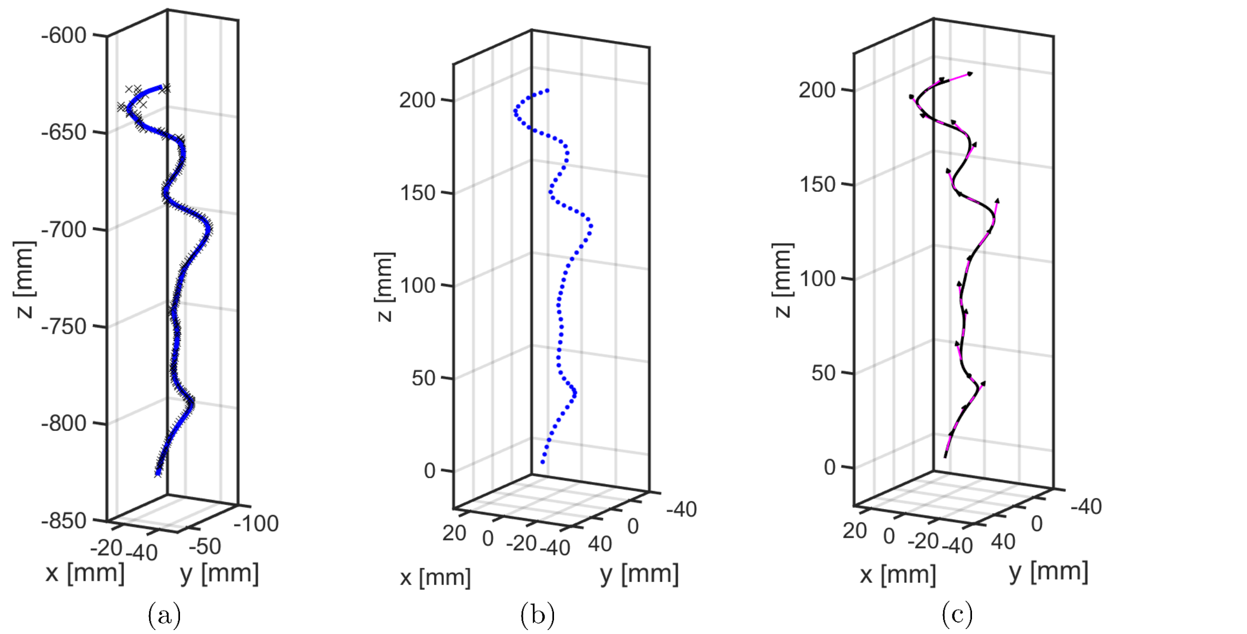

Figure 4.7: Parametrization of the ICA vasculature shown in Fig. 4.5. (a) The ICA centerline extracted using PCA and cubic smoothing spline fitting, (b) Equidistant (ds) points along the spline curve (c) Local tangent unit vectors along the ICA.

$$\hat{\mathbf{z}}_2 = (\mathbf{x}_{i+1} - \mathbf{x}_i) / (|\mathbf{x}_{i+1} - \mathbf{x}_i|) \tag{4.1}$$

The intermediate frame $\{\hat{\mathbf{x}}_1, \hat{\mathbf{y}}_1, \hat{\mathbf{z}}_1\}$ gives the orientation ${}^0\mathbf{R}_1$ of the local bending plane passing through the vertices $\mathbf{x}_i$ and $\mathbf{x}_{i+1}$ and perpendicular to the $(\hat{\mathbf{x}}_0, \hat{\mathbf{y}}_0)$ plane. The vector $\hat{\mathbf{x}}_1$ is the normalized projection of $\hat{\mathbf{z}}_2$ on the $\{\hat{\mathbf{x}}_0, \hat{\mathbf{y}}_0\}$ plane:

$$\hat{\mathbf{x}}_1 = \frac{1}{\sqrt{\left((\hat{\mathbf{z}}_2^T \hat{\mathbf{x}}_0)^2 + (\hat{\mathbf{z}}_2^T \hat{\mathbf{y}}_0)^2\right)}} \begin{bmatrix} \hat{\mathbf{z}}_2^T \hat{\mathbf{x}}_0 \\ \hat{\mathbf{z}}_2^T \hat{\mathbf{y}}_0 \\ 0 \end{bmatrix} \tag{4.2}$$

The angles α and β are derived:

$$\alpha = \mathrm{Atan2}\left(\frac{\hat{\mathbf{x}}_1^T \hat{\mathbf{y}}_0}{\hat{\mathbf{x}}_1^T \hat{\mathbf{x}}_0}\right) \qquad \beta = \mathrm{Atan2}\left(\frac{\hat{\mathbf{z}}_2^T \hat{\mathbf{x}}_1}{\hat{\mathbf{z}}_2^T \hat{\mathbf{z}}_0}\right) \tag{4.3}$$

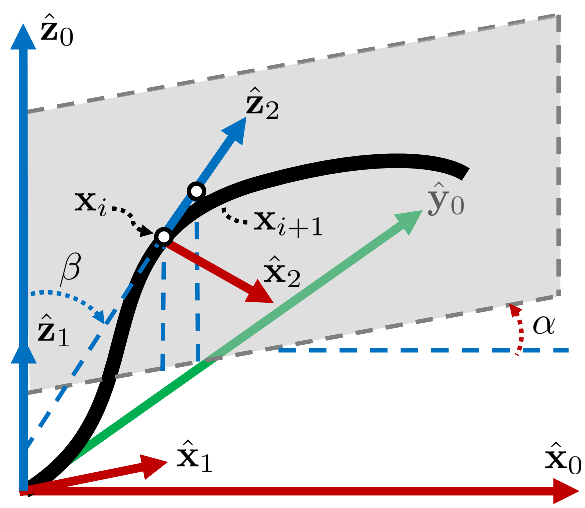

Figure 4.8: Frames used to calculate the local orientation along the vasculature; $\hat{\mathbf{y}}_i$ (not shown) follow the right-hand rule

4.5 Robot Modelling and Calibration

4.5.1 Kinematics Modelling

The direct kinematics of the SRMC are derived using the frame assignment shown in Fig. 4.9. The active joint parameters are described by $\mathbf{q} = [q_1, q_2, q_3, q_4]$, representing the insertion, roll, proximal CS bending, and distal CS bending, respectively. Each active-bending CS is assigned a frame at its base so that its x-axis is aligned in the bending plane of the CS and the y-axis is assigned along the direction of bending according to the right-hand rule. The z-axis of this frame points from the base to the tip of the CS when it is straight (Fig. 4.9a). A frame is also assigned to the tip of the CS with its z-axis along the tangent, its x-axis in the bending plane, and its y-axis parallel to the y-axis at the base frame. Assuming that an interleaving passive flexure has its compliant axis along the x-axis at the base of the distal segment, we use γ to designate its passive bending angle (Fig. 4.9b). We also assume that The bending planes of the first and second CSs are offset by a fixed angle δ. Using these definitions, the end effector pose is calculated by a moving frame transformation sequence between the base frame $\{0\}$ to the end effector frame $\{5\}$:

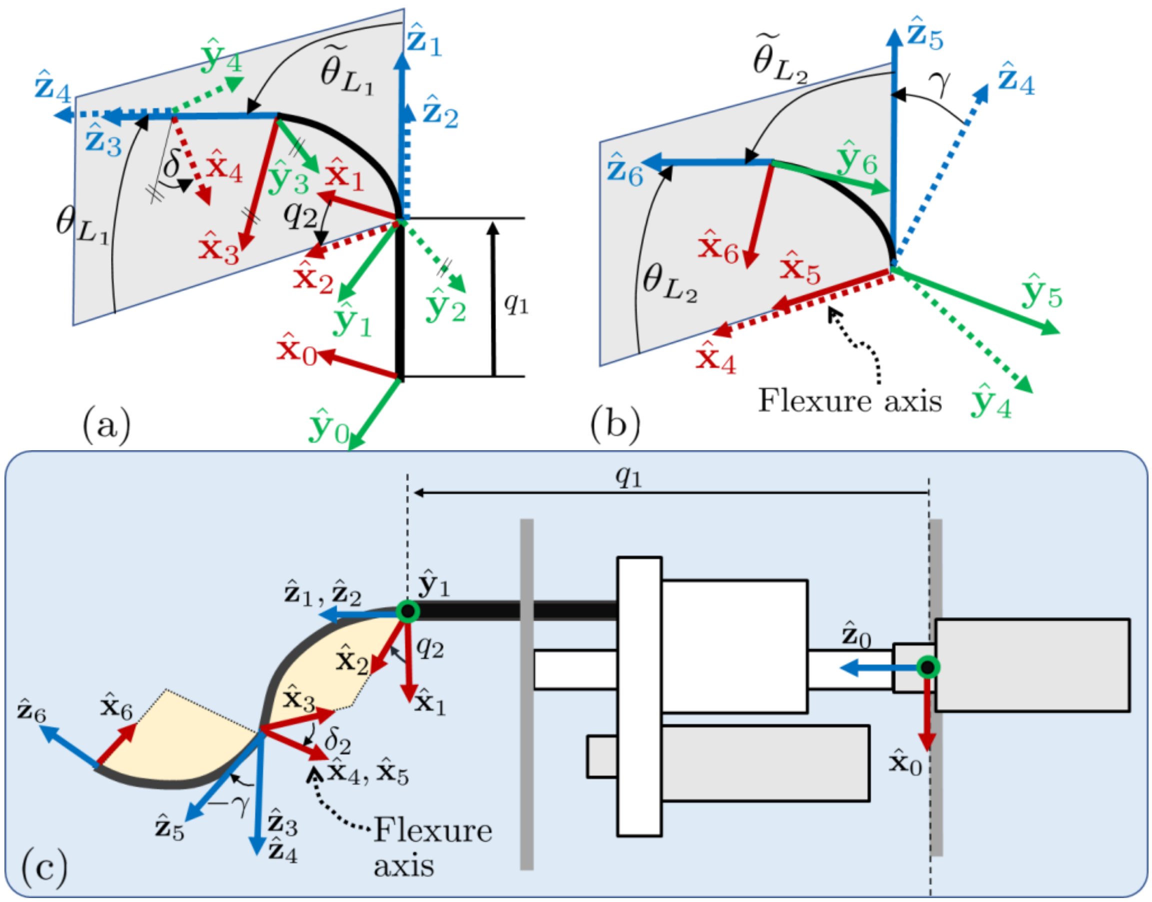

Figure 4.9: (a) Frames of proximal continuum segment. (b) Frames of the distal segment, including the passive flexure. (c) System overview. All $\hat{\mathbf{y}}_i$ axes (not shown) complete the frames using the right hand rule. The two shaded areas show the bending planes of each continuum segment.

$$ {}^{0}\mathbf{H}_5 = {}^{0}\mathbf{H}_1\, {}^{1}\mathbf{H}_2\, {}^{2}\mathbf{H}_3\, {}^{3}\mathbf{H}_4\, {}^{4}\mathbf{H}_5\, {}^{5}\mathbf{H}_6 \tag{4.4} $$

where the homogeneous transformations are given by:

$$ {}^{0}\mathbf{H}_1 = \begin{bmatrix} \mathbf{I}_{3\times 3} & q_1\hat{\mathbf{z}} \\ \mathbf{0} & 1 \end{bmatrix} \quad {}^{1}\mathbf{H}_2 = \begin{bmatrix} e^{q_2[\hat{\mathbf{z}}\times]} & \mathbf{0} \\ \mathbf{0} & 1 \end{bmatrix} \tag{4.5a} $$

$$ {}^{2}\mathbf{H}_3 = \begin{bmatrix} e^{\widetilde{\theta}_{L_1}[\hat{\mathbf{y}}\times]} & \mathbf{d}_1 \\ \mathbf{0} & 1 \end{bmatrix} \quad {}^{3}\mathbf{H}_4 = \begin{bmatrix} e^{\delta_2[\hat{\mathbf{z}}\times]} & \mathbf{0} \\ \mathbf{0} & 1 \end{bmatrix} \tag{4.5b} $$

$$ {}^{4}\mathbf{H}_5 = \begin{bmatrix} e^{\gamma[\hat{\mathbf{x}}\times]} & \mathbf{0} \\ \mathbf{0} & 1 \end{bmatrix} \quad {}^{5}\mathbf{H}_6 = \begin{bmatrix} e^{\widetilde{\theta}_{L_2}[\hat{\mathbf{y}}\times]} & \mathbf{d}_2 \\ \mathbf{0} & 1 \end{bmatrix} \tag{4.5c} $$

where $\widetilde{\theta}_{L_i} \triangleq \frac{\pi}{2} - \theta_{L_i}$ $(i = 1, 2)$, $e^{\theta[\hat{\mathbf{n}}\times]}$ is a shorthand notation for the rotation matrix about unit vector $\hat{\mathbf{n}}$ by angle θ, L_1 and L_2 are the lengths of the proximal and distal segments of the robot, and the vectors $\mathbf{d}_1$ and $\mathbf{d}_2$ are given by:

$$ \mathbf{d}_i = \int_0^{L_i} [\cos(\theta_i(s, q_{i+2})), 0, \sin(\theta_i(s, q_{i+2}))]^T \, ds \tag{4.6} $$

The bending motions of the proximal segment (θ_{L_1}) and the distal segment (θ_{L_2}) are actuated by the push-pull displacement of joints q_3 and q_4, respectively. The characteristic bending shape, i.e. the relationship $\theta(s, q)$, was determined experimentally for each CS.

4.5.2 Image-based Calibration

For each segment, the local tangent angle $\theta(s, q)$ is a function of the arc length $s \in [0, L]$ and the actuation displacement q, is determined using a modal approach [148] and an image-based calibration experiment following [149]. The minimal energy solution for the direct kinematics of a single segment is approximated using the modal representation:

$$\theta(s,q) = \sum_i a_i(q)\psi_i(s) = \boldsymbol{\Psi}(s)^T \mathbf{a}(q), \qquad \mathbf{a}, \boldsymbol{\Psi} \in \mathbb{R}^n \tag{4.7}$$

where $\boldsymbol{\Psi} = [1, s, s^2, ..., s^{n-1}]^T$ is a modal basis and $\mathbf{a}$ is a vector of modal coefficients. Since the variation of curvature along the length of the segment may be a function of the amount of segment bending, we define the modal coefficients as another smooth modal interpolation, such that:

$$\mathbf{a}(q) = \mathbf{A}\boldsymbol{\eta}(q), \quad \mathbf{A} \in \mathbb{R}^{n\times m}, \mathbf{q} \in \mathbb{R}^{m\times 1} \tag{4.8}$$

where $\boldsymbol{\eta}(q) = [1, q, q^2, ..., q^{m-1}]^T$ is another modal basis. This yields an interpolation map for local tangent:

$$\theta(s,q) = \boldsymbol{\Psi}(s)^T \mathbf{A}\boldsymbol{\eta}(q) \tag{4.9}$$

The matrix $\mathbf{A}$ is the *unknown* characteristic shape matrix and is determine experimentally through an image-based calibration experiment. For each segment, the associated actuation line was displaced in increment $dq = 0.1$ mm until a maximum bending range ($\theta_{max} \simeq 80°$). At each configuration, a camera oriented parallel to the bending plane was used to record the image of the segment. Fig. 4.10(a) shows configurations of the distal segment for various q displacements. The recorded images were subsequently segmented using *thresholding* to extract the nodes belonging to outline of the segment. A *smooth cubic spline* was then used to fit these vertices, and spline sections belonging to the straight portion of the catheter were truncated. In Fig. 4.10(b), the bent section is shown in green and the truncated portions are shown in red.

At each arc-length $s \in [0, L]$, the angle of the tangent $\theta(s)$ was calculated with respect to $\hat{\mathbf{x}}$ using forward finite different approximation between successive points, as shown in Fig. 4.10(b)).

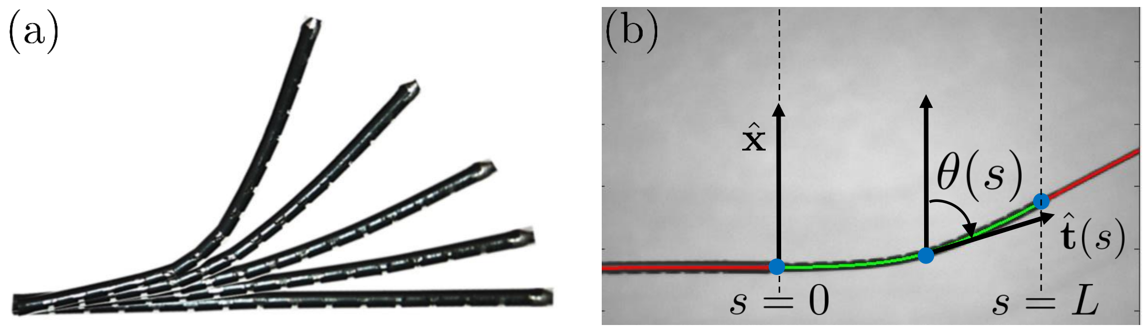

Figure 4.10: (a) Configurations of the distal SRMC segment for various $\mathbf{q}$ values. (b) Parametrization of the CS shape.

The experimental data from the calibration experiment was concatenated into an experimental matrix $\mathbf{\Phi}$, consisting of z joint displacements q (corresponding to z images) and r tangent locations (θ) along the length of segment:

$$\mathbf{\Phi}_{r\times z} = \begin{bmatrix} \theta(s_1,q_1) & \cdots & \theta(s_1,q_z) \\ \vdots & \ddots & \vdots \\ \theta(s_r,q_1) & \cdots & \theta(s_r,q_z) \end{bmatrix}$$

$$= \underbrace{\begin{bmatrix} \psi^{\mathrm{T}}(s_1) \\ \vdots \\ \psi^{\mathrm{T}}(s_r) \end{bmatrix}}_{\mathbf{\Omega}_{r\times n}} \mathbf{A}_{n\times m} \underbrace{\begin{bmatrix} \boldsymbol{\eta}(q_1), \cdots, \boldsymbol{\eta}(q_z) \end{bmatrix}}_{\mathbf{\Gamma}_{m\times z}} \tag{4.10}$$

Equation (4.10) is a matrix equation with the unknown $\mathbf{A}$. Using the *Vec* and the Krönecker product $\otimes$ as defined in [150], this equation is cast as a vector equation with the concatenated columns of $\mathbf{A}$ stacked in the unknown vector $Vec(\mathbf{A})$:

$$Vec(\mathbf{\Phi}) = Vec(\mathbf{\Omega}\boldsymbol{A}\mathbf{\Gamma}) = [\mathbf{\Gamma}^T \otimes \mathbf{\Omega}]Vec(\mathbf{A}) \tag{4.11}$$

The solution to the above equation is:

$$Vec(\mathbf{A}) = [\mathbf{\Gamma}^T \otimes \mathbf{\Omega}]^{-1} Vec(\mathbf{\Phi}) \tag{4.12}$$

Finally, the characteristic shape matrix $\mathbf{A}$ is determined by parsing $Vec(\mathbf{A})$ for the consecutive columns of $\mathbf{A}$. Given $\mathbf{A}$, the algebraic expression of $\theta(s,q)$ is calculated by plugging the numerical matrix $\mathbf{A}$ from (4.12) into (4.9).

A simulation study of the order of the monomial bases to fit the experimental data showed that the polynomial coefficients $m = 2$ and $n = 4$ provided the necessary precision without overfitting the data. The mean error between the experimental values in $\mathbf{\Phi}$ and analytical values (calculated using (4.9)) was 0.021 degrees for the proximal segment and 0.057 degrees for the distal segment.

4.5.3 Actuation Compensation and Kinematic Coupling

The calibration experiment described in Section 4.5.2 was performed on the NiTi segments, directly. Once this steerable tip is extended with the passive catheters and mounted to the actuation unit, there are losses in the system that introduce errors in the calibrated model. To capture these losses, we repeated the calibration data collection with the system fully assembled. Fig. 4.11 shows the measured end effector tangent angles $\theta_L(q)$, compared to the expected angle $\theta_L^* = \theta(L,q)$ at calculated from the calibrated model of the steerable tip alone.

The system losses due to passive catheter extensions, the springs, and the friction in the actuation unit are described by the linear equations (4.13) for the proximal segment and (4.14) for the distal segment.

$$\theta_{L_1} = 0.063\,\theta_{L_1}^* - 0.049 \tag{4.13}$$

$$\theta_{L_2} = 0.17\,\theta_{L_2}^* + 0.019 \tag{4.14}$$

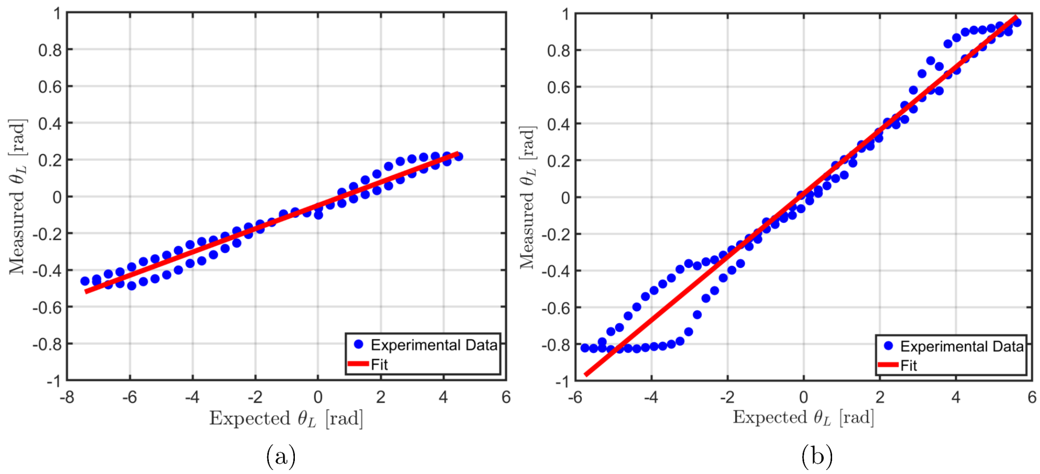

Figure 4.11: Expected bending angle from calibrated kinematics vs measured bending angle due to losses in the system: (a) proximal segment, (b) distal segment.

There is also the need to compensate for the kinematic coupling between the two segments. Such compensation was presented in [114] for a multi-backbone continuum robot. The bending of proximal segment results in the displacement of the distal segment actuation such that:

$$\frac{\partial q_4}{\partial \theta_{L_1}} = -r_1 \cos(\delta_2) \tag{4.15}$$

where r_1 is the outer radius of the proximal segment.

The path planning and catheter parameter optimization presented in section 4.6 rely on the nominal kinematics model, without compensation. The approach presented remains valid because the need for actuation compensation stems from the stiffness of the actuation lines, rather than the length of the active segments. Furthermore, we assume that the notches design of the segments keep the bending stiffness of the active segments fixed.

4.6 Preoperative Path Planning

4.6.1 Shape Error Minimization

Successful path planning requires minimizing the passive deflection of the catheter tip. This is achieved by matching the shape of the catheter as closely as possible to that of the vasculature using the active joints $[q_2,q_3,q_4]^T$ (roll and CS bending DoFs) and the passive flexure bending γ. For a given insertion depth q_1, which corresponds to the portion of vasculature arc-lengths occupied by the catheter $\{s_i \in [0,L_{vasc}]\,|s_i \leq q_1\}$, the shape deviation between the catheter and the vasculature is calculated using the local position and tangent errors as shown in Fig. 4.12. Denoting $\hat{\mathbf{t}}$ and $\hat{\mathbf{t}}_c$ as the local tangents to the catheter and vasculature, and $\mathbf{p}_i$ and $\mathbf{c}_i$ as the local points on the catheter and vasculature, we can define these errors as:

$$\boldsymbol{\delta}_{\mathbf{p}_i} = \mathbf{p}(s_i,\mathbf{q}) - \mathbf{c}(s_i),\ \boldsymbol{\delta}_{\hat{\mathbf{t}}_i} = \arccos(\hat{\mathbf{t}}(s_i,\mathbf{q})^T\hat{\mathbf{t}}_c(s_i)) \tag{4.16}$$

With these definitions, the problem is cast as the following nonlinear least-squares problem:

$$\underset{q_2,q_3,q_4}{\text{minimize}}\left(\sum_{i=1}^{n}(\boldsymbol{\delta}_{\mathbf{p}_i})^T\mathbf{W}_p(\boldsymbol{\delta}_{\mathbf{p}_i}) + \sum_{i=1}^{n}(\boldsymbol{\delta}_{\hat{\mathbf{t}}_i})^T\mathbf{W}_t(\boldsymbol{\delta}_{\hat{\mathbf{t}}_i})\right) \tag{4.17}$$

The number of inserted points n is a function of the inserted catheter length q_1 (which can measured using encoder values or a linear potentiometer), such that $n = \text{floor}(\text{q}_1/\text{ds})$. The weight matrices $\mathbf{W}_p$ and $\mathbf{W}_t$ correspond with the position and orientation error penalties, respectively. Equation (4.17) is solved numerically using the Levenberg-Marquardt nonlinear least squares formulation.

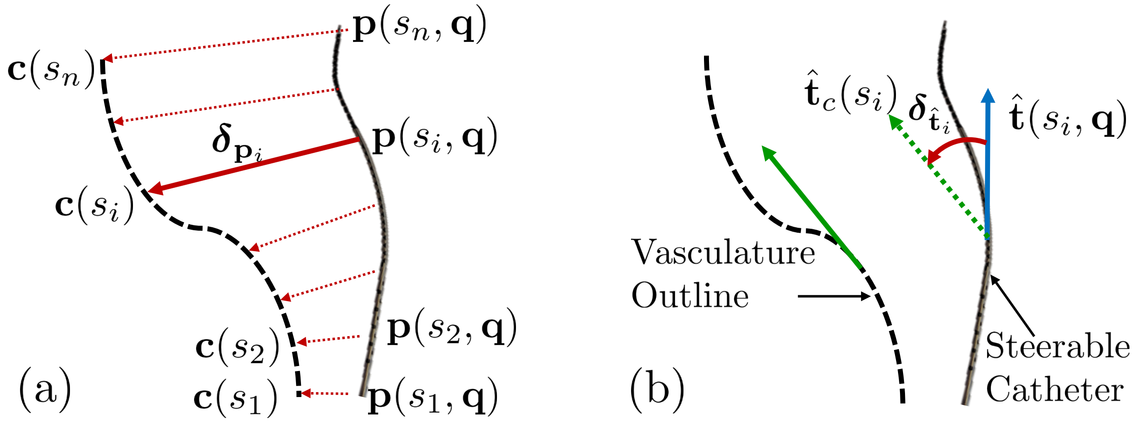

Figure 4.12: Illustration of the least square optimization problem, showing (a) local position error and (b) local tangent error between the vasculature and the robotic catheter.

$$\mathbf{W}_p = \frac{1}{\delta_{p_{range}}} \begin{bmatrix} \mathbf{W}_2 & \mathbf{0} & \mathbf{0} \\ \mathbf{0} & \mathbf{W}_1 & \mathbf{0} \\ \mathbf{0} & \mathbf{0} & \mathbf{0} \end{bmatrix}, \ \mathbf{W}_t = \frac{r_{tp}}{\delta_{t_{range}}}\mathbf{W_p} \tag{4.18}$$

Where $\mathbf{W}_2$ and $\mathbf{W}_1$ are the weights given to points along the distal and proximal segments, respectively. The bottom-right zero element in $\mathbf{W}_p$ is a zero-penalty weight matrix corresponding with the non-steerable lumen of the catheter. Also, r_{tp} is the orientation-to-position penalty ratio, and $\delta_{p_{range}} = 10$ mm and $\delta_{t_{range}} = 1$ rad are normalization numbers designating maximal expected errors.

We define a ratio of penalty for errors in the distal and proximal segments using r_{seg} such that:

$$\mathbf{W}_2 = \tilde{\mathbf{W}}_2, \quad \mathbf{W}_1 = r_{\mathrm{seg}}\tilde{\mathbf{W}}_1 \tag{4.19}$$

where $\tilde{\mathbf{W}}_k,\ k = 1,2$ are the weights along the spline of each segment. These weights were determined by soft step functions that minimize the risk of catheter tip jamming into the vasculature walls. This is achieved by giving the tracking error at the segment tip a higher weight than the tracking error at its base. Therefore, $\tilde{\mathbf{W}}_k \in [0,1]$ is defined as:

$$\tilde{\mathbf{W}}_k = diag\left(\frac{1}{2}\left(1+\tanh\left(5\left(\frac{\mathbf{v}_k}{n_k}-\frac{1}{2}\right)\right)\right)\right) \tag{4.20}$$

where n_k is the number of equidistant arc-length points along the k^{th} segment, $\mathbf{v}_k = 1,2,$ ..., n_k is the vector of indices up to n_k, and $diag(\mathbf{x})$ is a matrix having $\mathbf{x}$ along its main diagonal.

A weight selection procedure to determine the optimal r_{tp}^* and r_{seg}^* was performed by simulating the performance of the path planner over a range of 0-10 for both variables. Details of these optimal variables are provided in the results section.

Fig. 4.13 is a flow chart illustrating the path following with shape error minimization algorithm. The path following computation takes 14.5 seconds in MATLAB 2021a with a

Intel Core i7 processor.

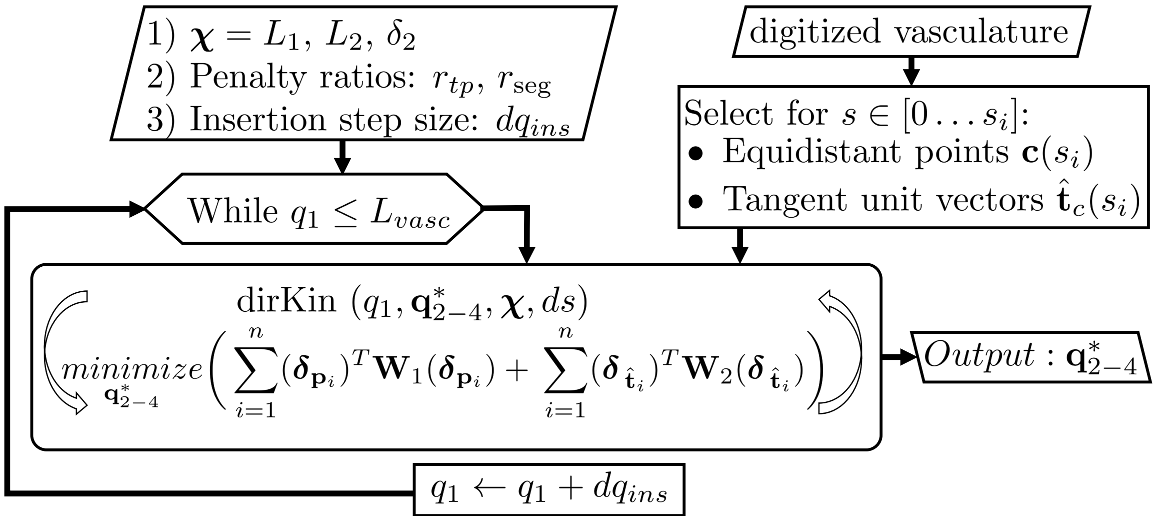

Figure 4.13: Path following algorithm for shape error minimization

4.6.2 Catheter Design Optimization

The catheter design parameters $\chi = [L_1,\ L_2,\ \delta_2]^{\mathrm{T}}$ affect the ability of a catheter to follow a desired vasculature. To find the optimal catheter design parameters χ^*, we used the Nedler-Mead Simplex algorithm to minimize a design error penalty score $g(\chi)$. This algorithm computes in 17.72 minutes in MATLAB 2021a. Figure 4.14 outlines this process. This penalty score was defined as the sum of normalized errors for an optimal path plan corresponding with the current catheter design parameters χ. Defining $\max(\boldsymbol{\delta}_p)$, $\bar{\boldsymbol{\delta}}_p$ and $\max(\boldsymbol{\delta}_t)$, $\bar{\boldsymbol{\delta}}_t$ as the maximal and average position and orientation errors for the optimal path plan covering the entire length of the vasculature, $g(\chi)$ is defined as:

$$g(\chi) = \frac{\max(\boldsymbol{\delta}_{\mathrm{p}}) + \bar{\boldsymbol{\delta}}_{\mathrm{p}}}{\delta_{p_{range}}} + \frac{\max(\boldsymbol{\delta}_{\mathrm{t}}) + \bar{\boldsymbol{\delta}}_{\mathrm{t}}}{\delta_{t_{range}}}$$

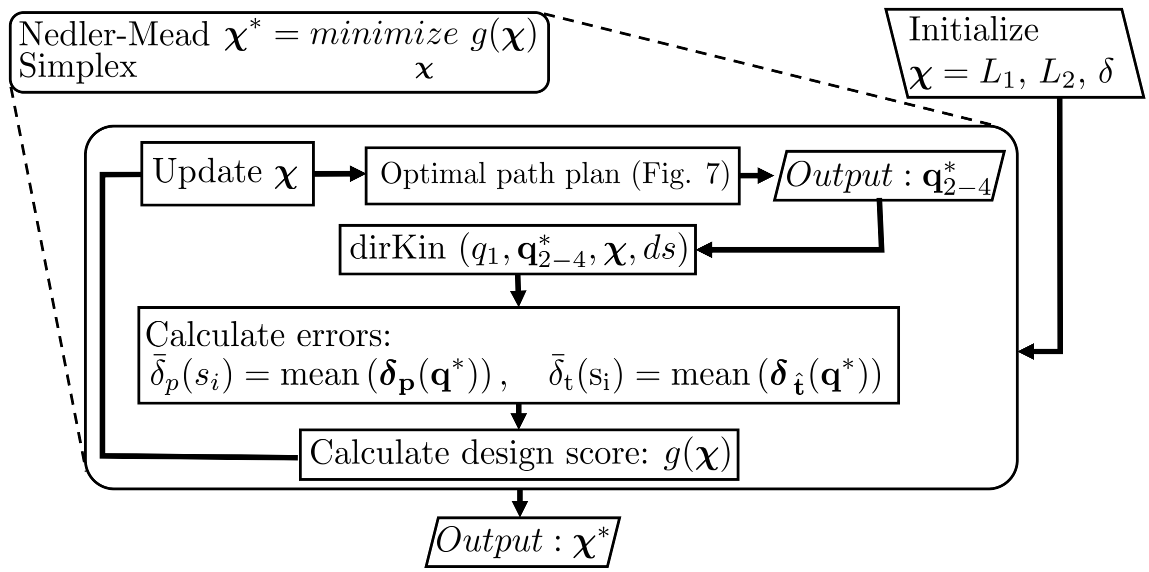

Figure 4.14: An overview of the catheter design parameter optimization using the Nedler-Mead simplex method

4.6.3 Simulation Study

We validated the algorithms of Figs. 4.13 and 4.14 in a simulation case study, where we insert a steerable catheter along the ICA path (Fig. 4.7). We compare three catheter options: our *ad-hoc* design ① shown in Fig. 4.4, an optimized version of the catheter without the flexure ②, and a optimized catheter with a flexure ③.

For cases ② and ③, we computed r^*_{tp} and r^*_{seg}, and catheter parameters χ^*. We used these optimal parameters as input to the path following algorithm (Fig. 4.13) and computed the position and orientation errors along the vasculature. Other inputs to the path planner include the curve parameterization step size ($ds = 0.5$ mm), and insertion step size ($dq_{ins} = dq_1 = 3$ mm).

Fig. 4.15 show the robotic catheter following the ICA path (Fig. 4.15(a)) and the RMS error as a function of insertion length illustrates these results (Fig. 4.15(a)) for different catheter geometric parameters. The parameters and path following performance of each case are summarized in Table 4.1.

These results show that the use of optimized penalty ratios and catheter design param-

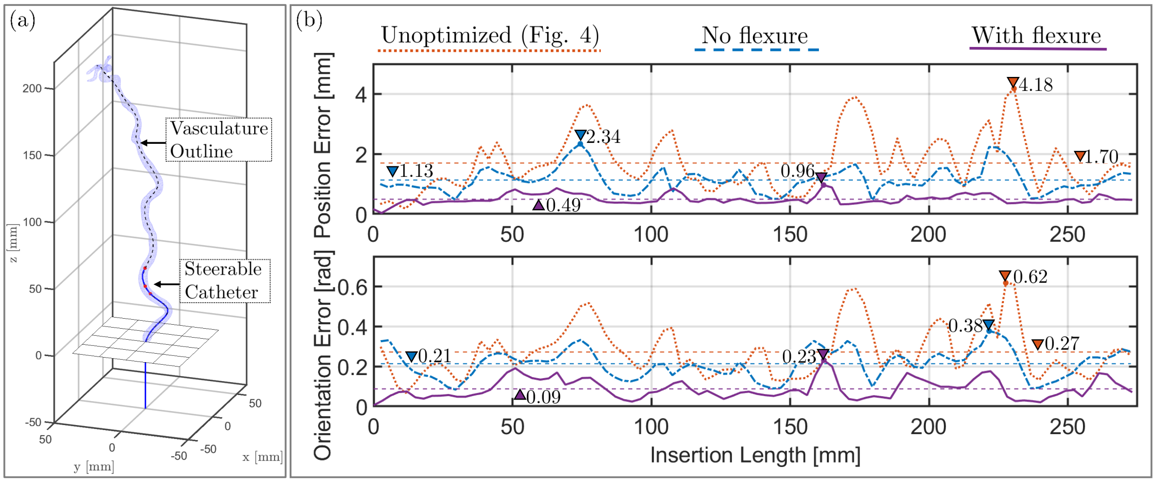

Figure 4.15: (a) Robotic catheter following the ICA path in simulation. (b) Position and orientation errors as a function of insertion length for three designs options: ① *ad hoc*, ② optimized without flexure, and ③ optimized with flexure.

	r^*_{seg}, r^*_{tp}	χ^* [mm, mm, rad]	$\bar{\delta}_p, \max(\delta_\text{p})$ [mm]	$\bar{\delta}_t, \max(\delta_\text{t})$ [rad]
①	n/a	[22, 18.8, -0.76]	1.70, (4.18)	0.27, (0.62)
②	[1, 0.75]	[10.5, 23.5, -0.44]	1.13, (2.34)	0.21, (0.38)
③	[1.25, 0.75]	[6.6, 13.8, 0.07]	0.49, (0.96)	0.09, (0.23)

Table 4.1: Optimization outputs and resulting path following errors for the *ad hoc* catheter ① and the optimized catheter excluding ②, and including ③ a passive flexure joint.

eters (case ②) significantly improves the tracking performance. The addition of a flexure DOF (case ③) further improves the tracking performance, such that the average position tracking error is 0.49 mm and the average orientation error is 0.09 rad (5.16 degrees).

To access the ICA during endovascular stroke care, surgeons need to navigate the aortic arch. A type III aortic arch can be particularly challenging to traverse because of its sharp curvature. A MATLAB vasculature path was generated using the complete CT scan that provided the ICA geometry in Fig. 4.5. This path was augmented with a sample path segmented from a trial path as shown on a 3D print of the CT scan as shown Fig. 4.16a. Fig. 4.16b shows the vasculature path that combines the ICA with a type III aortic arch.

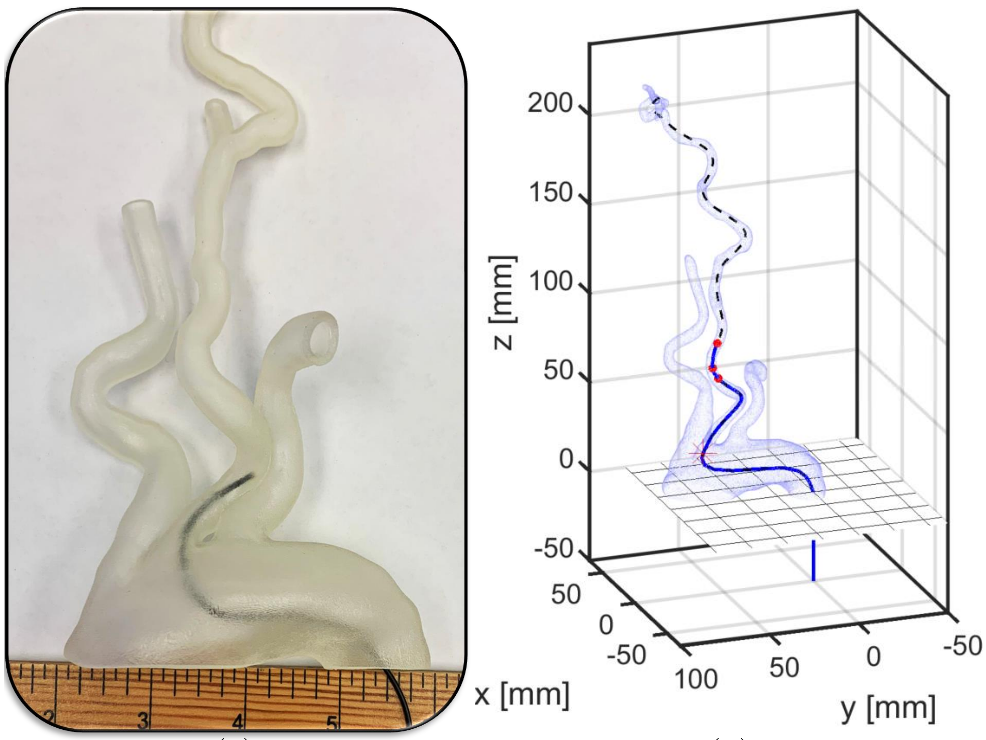

(a) (b)

Figure 4.16: (a) Possible path into the ICA through a type III aortic arch (b) Simulation of optimized catheter traversing the ICA via the aorta path.

The optimized catheter designed achieved average/maximal position tracking errors of 0.50/1.40 mm and average/maximum orientation errors of 0.09/0.22 rad, in simulation.

4.7 Multi-Mode Catheter Control

Figure 4.17 shows the strategy for real-time control of the robotic catheter system. This controller was implemented using Simulink Real-Time on a PC/104 target computer (⑬ in Fig. 4.4). A low-level controller (LLC) runs at 1kHz and uses proportional derivative integrator (PID) control law to close the error between the current joint values $\mathbf{q}_{cur}$ and the desired joint values $\mathbf{q}_{des}$. This controller ensures safe and smooth operation of the device. The LLC takes input from a mid-level controller (MLC), which specifies the desired joint values $\mathbf{q}_{des}$ based on the selected trajectory planner mode. The MLC includes four modes: joint space control, configuration space control, admittance control, and telemanipulation. A graphical user interface enables switching between these four modes.

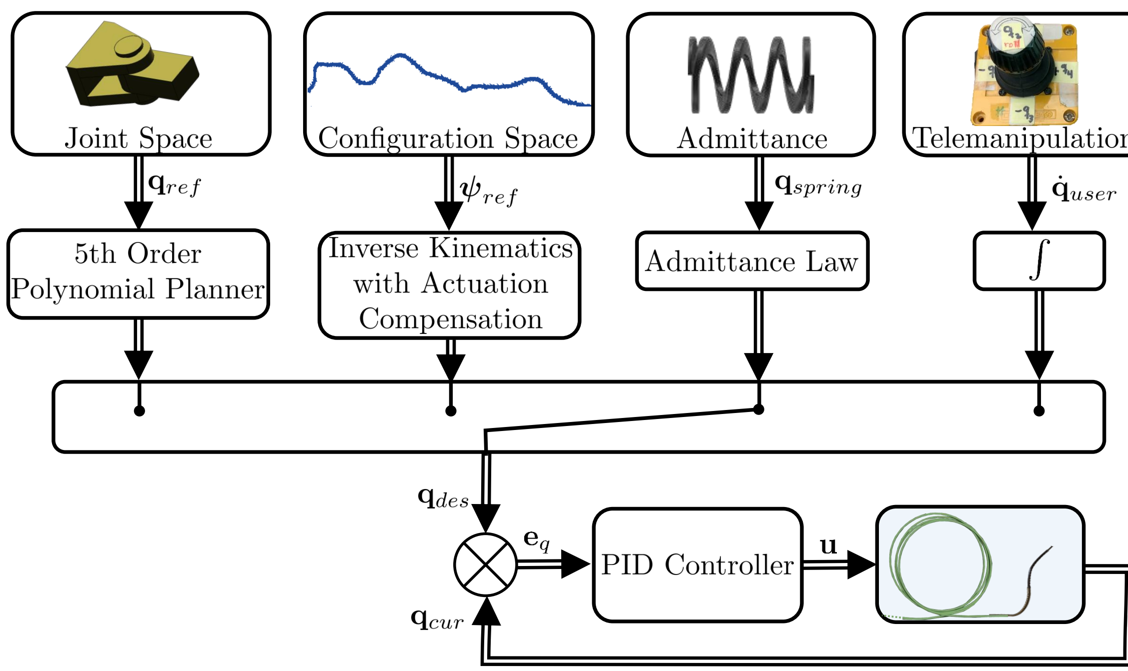

Figure 4.17: Control approach for enabling multi-mode control of catheters. Each mode corresponds to a different input source, accounting for different stages of catheter insertion.

4.7.1 *Joint Space Control*

In this mode, a fifth order polynomial interpolation law is used to ensure a smooth transition between the current joint positions $\mathbf{q}_{cur}$ and a reference joint position $\mathbf{q}_{ref}$. The

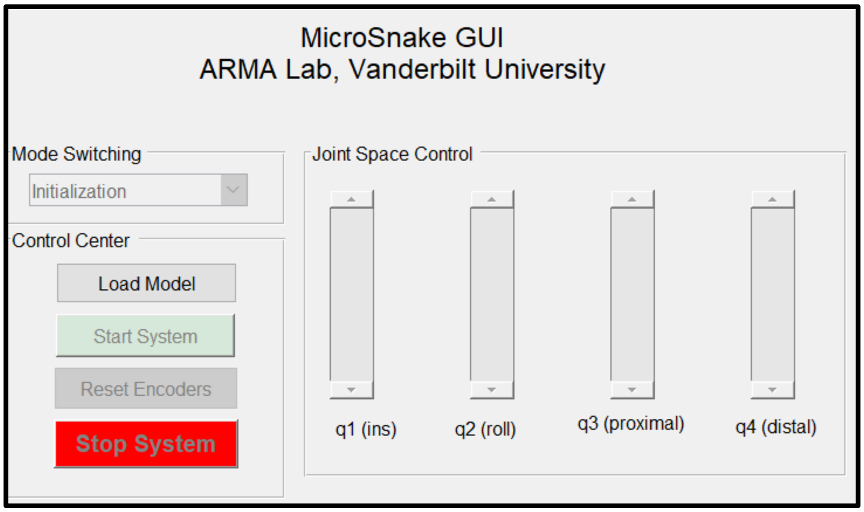

Figure 4.18: Graphical User Interface for intuitive catheter control and mode switching

polynomial interpolation updates $\mathbf{q}_{des}$ at 1 kHz, while the reference joint values $\mathbf{q}_{ref}$ are updated at more interactive rates (0.5-3Hz).

4.7.2 Configuration Space Control

Configuration space control enables the user to set desired bending angles θ_{L_1} and θ_{L_2} for the proximal and distal segments, respectively. The configuration space vector includes insertion, roll, and the bending DoFs, i.e. $\psi = [q_1, q_2, \theta_{L_1}, \theta_{L_2}]$. For a commanded reference configuration ψ_{ref}, a fifth order polynomial planner calculates intermediate joint velocities $\dot{\psi}_{des}$ to close the error from the current configuration ψ_{cur}. Differential kinematics and the calibrated loss matrix are then used to calculate the corresponding joint level velocity $\dot{\mathbf{q}}_{des}$:

$$\dot{\mathbf{q}}_{des} = \left(\mathbf{A}_{coupling} + \left(\mathbf{A}_{loss}\mathbf{J}_{\psi\mathbf{q}}\right)^{-1}\right)\dot{\psi}_{des} \tag{4.21}$$

where:

$$\mathbf{A}_{coupling} = \begin{bmatrix} 0 & 0 & 0 & 0 \\ 0 & 0 & 0 & 0 \\ 0 & 0 & 0 & 0 \\ 0 & 0 & r_1\cos(\delta_2) & 0 \end{bmatrix} \quad \text{and} \quad \mathbf{A}_{\text{loss}} = \begin{bmatrix} 1 & 0 & 0 & 0 \\ 0 & 1 & 0 & 0 \\ 0 & 0 & a_1 & 0 \\ 0 & 0 & 0 & a_2 \end{bmatrix} \tag{4.22}$$

The coupling matrix $\mathbf{A}_{coupling}$ is constructed using equation 4.15. The loss matrix $\mathbf{A}_{loss}$ is constructed from the slopes a_1 and a_2 of the linear loss functions calculated in (4.13) and (4.14), respectively. The Jacobian $\mathbf{J}_{\psi q}$ transforms configuration speeds into joint speeds, using the derivative of the analytical relation $\theta(s,q)$ derived for each segment in Section 4.5.2:

$$\mathbf{J}_{\psi q} = \begin{bmatrix} 1 & 0 & 0 & 0 \\ 0 & 1 & 0 & 0 \\ 0 & 0 & \frac{\partial \theta_{L_1}}{\partial q_3} & 0 \\ 0 & 0 & 0 & \frac{\partial \theta_{L_2}}{\partial q_4} \end{bmatrix} \tag{4.23}$$

Finally, the desired joint value $\dot{\mathbf{q}}_{des}$, passed to the LLC, is calculated by integrating $\dot{\mathbf{q}}_{des}$.

4.7.3 Active Compliance

In active compliance mode, the desired joint values $\mathbf{q}_{des}$ are calculated as function of the measured joint values $\mathbf{q}_{cur}$ (from encoders) and the spring displacements using the following admittance law:

$$\mathbf{q}_{des} = \mathbf{q}_{cur} + \begin{bmatrix} 0 \\ 0 \\ dq_{a_1} \\ dq_{a_2} \end{bmatrix} \tag{4.24}$$

where dq_{a_i} is the corrective joint motion produced by the displacement of i^{th} spring from equilibrium ($i = 1$ for proximal segment spring and $i = 2$ for distal segment spring).

$$dq_{a_i} = K_a\big((1 - t_i)\,v_{min} + t_i\,v_{max}\big)\,dt \tag{4.25}$$

in which K_a is the admittance gain, v_{min} is the minimum admittance speed, v_{max} is the maximum admittance speed, dt is the time step, and t_i is the admittance velocity scaling defined as:

$$t_i = \frac{q_{s_i}}{q_{s_{i,max}}} \tag{4.26}$$

where q_{s_i} is the measured deflection of the i^{th} spring and $q_{s_{i,max}}$ is the maximum allowable spring deflection.

4.7.4 Telemanipulation

A tripe-axis industrial joystick controller (P3America, series 822) enables the user to remotely input velocity commands for roll, proximal bending, and distal bending. For each axis, a precision potentiometer outputs a voltage (0-5V) proportional to the displacement in that direction. The voltage is shifted and scaled such that 5V corresponds to the maximum joint speed in the positive direction and 0V is the maximum joint speed in the negative direction. The joint velocity vector $\dot{\mathbf{q}}_{user}$ is then integrated to obtain $\mathbf{q}_{des}$.

4.8 Intraoperative Catheter Segmentation and Tracking

In this section, an approach for segmenting and tracking the pose of the catheter during endovascular navigation is presented. The catheter outline is segmented in 2D from the bi-plane fluoroscopy image stream.

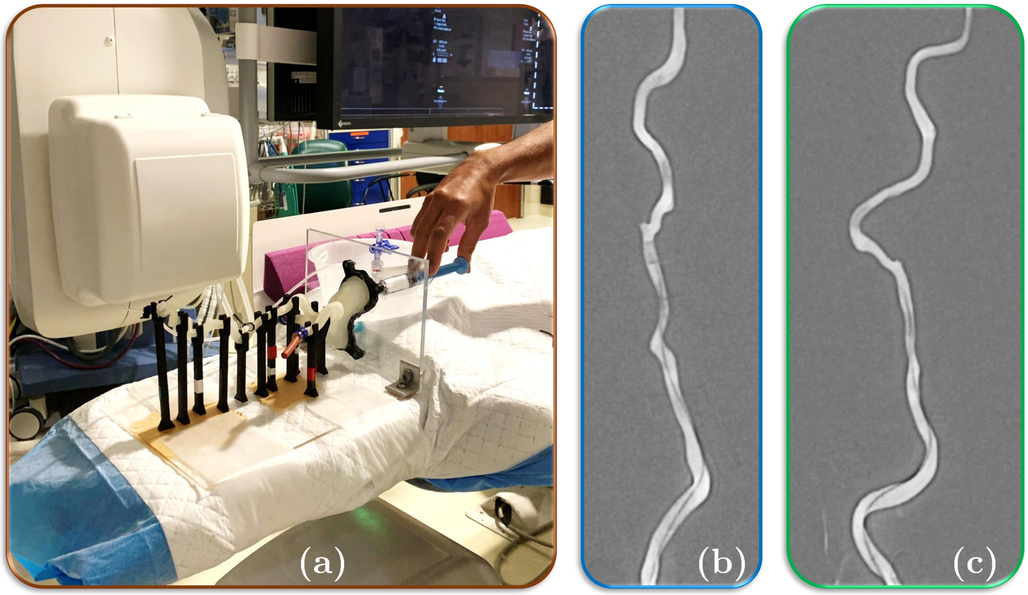

Figure 4.19: Setup for bi-plane fluoroscopy imaging of our mock vasculature. (a) The surgeon inserts a contrast agent in the mock vasculature. (b) Lateral view of the mock vasculature. (c) anteroposterior view of the mock vasculature.

4.8.1 Catheter Segmentation from Bi-plane Fluoroscopy Images

To develop and test our image segmentation algorithm, a mock endovascular insertion was performed in an operating room equipped with a Phillips bi-plane fluoroscopy machine, as shown in Fig. 4.19. A contrast agent (Omni 300) was injected into the phantom vasculature prototype to obtain an angiogram. A *SmartMask* filter was applied to the angiogram to obtain a static roadmap of the vasculature, and the robotic catheter was inserted into the vasculature against this static roadmap. Fluoroscopy images (AP and lateral views) of catheter insertion process were recorded for offline segmentation in MATLAB. Fig. 4.20(a) shows a sample image obtained from this experiment.

The outline of the catheter was segmented and tracked using the following steps: First, an image of the empty vasculature is cropped to exclude widgets of the fluoroscopy machine. This image is then binarized into foreground (white) and background (black) pixels using *thresholding* in MATLAB (Fig. 4.20(b)). Next, the background pixels (from the empty vasculature) are subtracted from an image of the filled (i.e. catheter inserted) vascu-

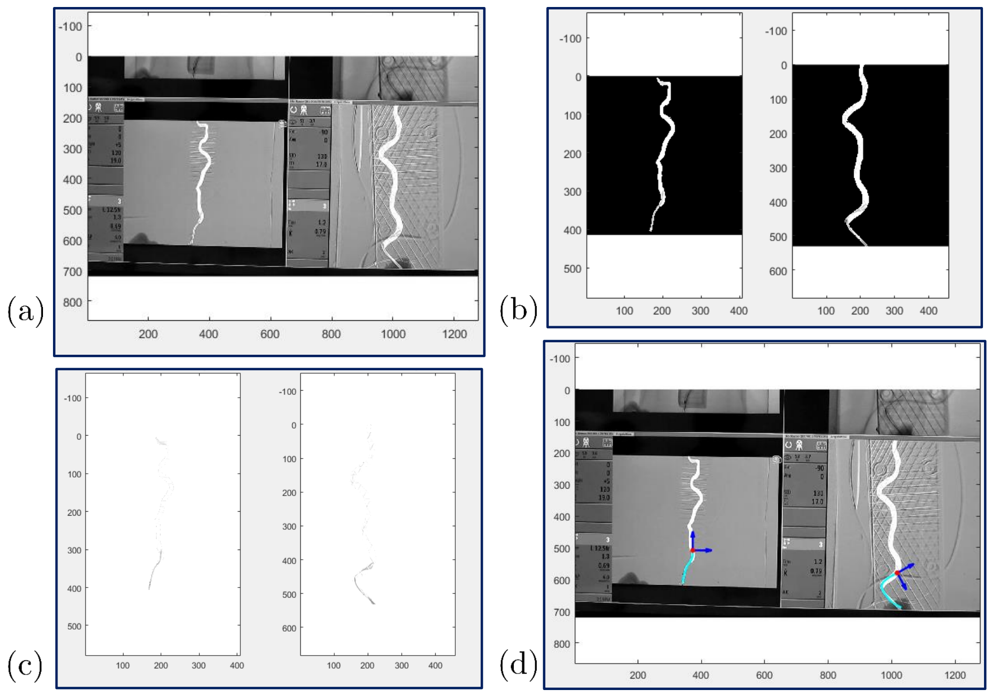

Figure 4.20: (a) Bi-plane fluoroscopy imaging of the phantom vasculature prototype. (b) Binarized image of the empty vasculature using *thresholding*. (c) Background is removed to isolate the outline of the catheter. (d) The catheter outline is segmented using Canny edge detection and the result is overlaid onto the original image

lature. This step serves to isolate the outline of the catheter, as shown in Fig. 4.20(c). Finally, the catheter outline is segmented using Canny edge detection. A spline is fit through the corresponding pixels and pose of the catheter is calculated. Fig. 4.20(d) shows the segmented catheter results overlaid on the original image. The segmentation parameters (cropping coordinates, threshold level, canny threshold) obtained from these two images (empty and filled vasculature) are utilized to track the catheter in all subsequent images. Fig. 4.21(a)-(c) show the poses of the tracked catheter at different insertion depth. The catheter segmentation and tracking algorithm run at 10 Hz.

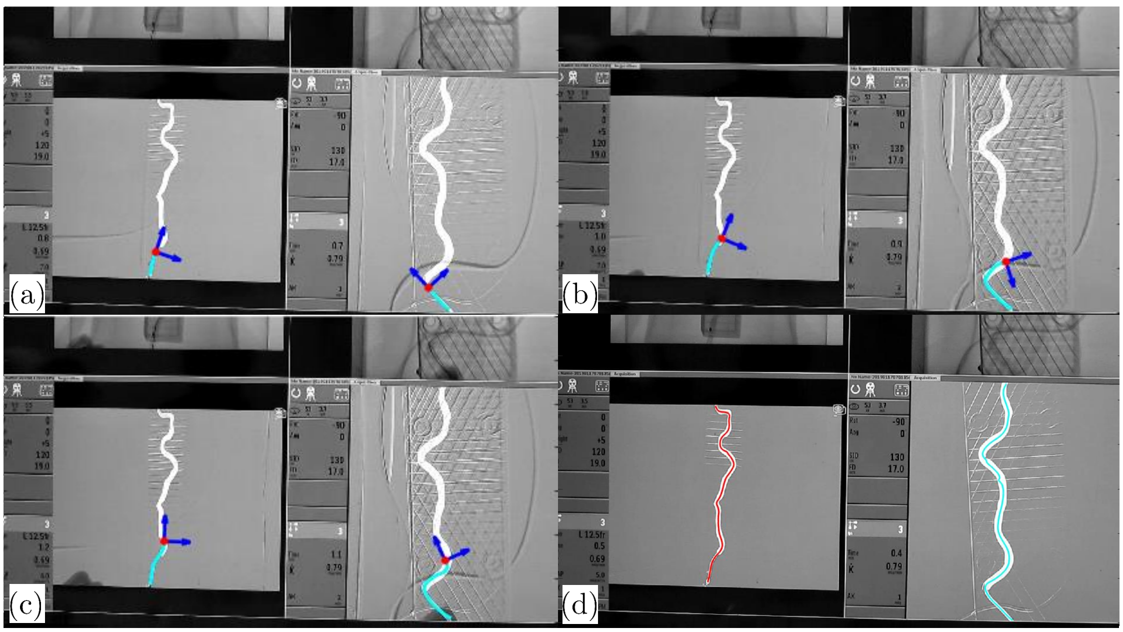

Figure 4.21: (a), (b) and (c) show segmentation and tracking of the microcatheter in three poses. (d) Segmentation of vasculature phantom centerline

The outline of the vasculature is obtained from the binary image of the empty vasculature (Fig. 4.20(b)) by thinning the foreground pixels using a morphological operator (*bwmorph*), calculating the cartesian positions of the thinned pixels, and fitting a smooth spline. Fig. 4.21(d) shows the outline of the vasculature overlaid onto an image of the empty vasculature. The vasculature outline segmentation runs at 20 Hz.

4.8.2 *Graphical User Interface for Live Image Segmentation*

The previous section describes our strategy for off-line segmentation of fluoroscopy images. For intraoperative *online* catheter segmentation and tracking, we developed a custom graphical user interface (Fig. 4.22) to enables the surgeon to interactively select the cropping, threshold and edge detection (Canny) parameters for both views (AP and lateral) to initiate the segmentation process. The image stream will be acquired for the fluoroscopy machine using a video encoder (Sensoray 2263).

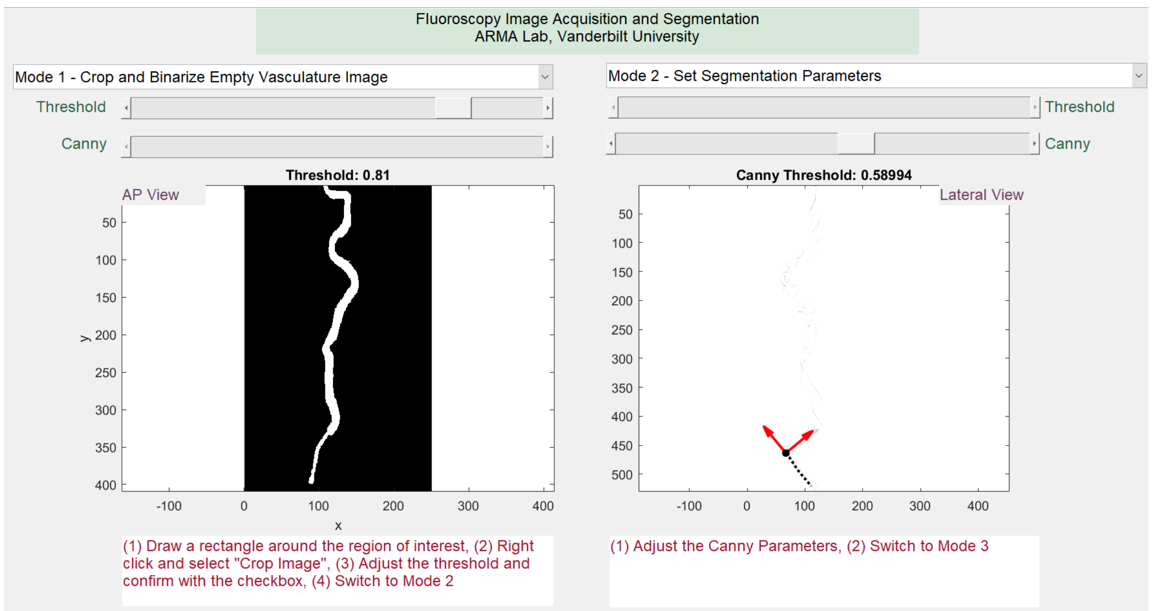

Figure 4.22: User interface for intraoperative catheter segmentation from bi-plane fluoroscopy imaging. The left side shows the thresholding of the AP view of vasculature. The right side shows the segmented catheter.

4.9 Catheter Pose Filtering

Pose filtering is needed to render the catheter tracking framework robust to noise and segmentation errors. Filtering-based estimation methods, which model the pose uncertainty as a probability density function and update the model parameters after subsequent measurements, are most appropriate for solving this sequential pose estimation problem. Kalman Filters are used to optimally estimate the state of linear systems, in which the state uncertainty is modelled as Gaussian distribution [151, 152]. For non-linear systems, the Extended Kalman Filter (EKF) [153] and the Unscented Kalman Filter (UKF) [154] have been used for the first-order and second-order linear approximations of systems, respectively. Probabilistic distribution such as Langevin distribution [155] and Bingham distribution [156] have also been used in the literature to model and filter pose uncertainty.

We chose Kalman filtering to estimate the catheter pose as it is deployed into a vasculature of known (pre-segmented) geometry. The equations describing the motion of the catheter during insertion are non-linear, thus we use the extended version of the Kalman filter (EKF). Prior works that have used Kalman filter for pose filtering and data fusion include [157, 158, 159, 160, 161, 162].

4.9.1 Kalman Filter Algorithm

The Kalman filter is an optimal recursive data processing algorithm that works in two stages: prediction and correction of the states of a system [151, 163, 164, 165]. We chose the Kalman filter for this application because it is well suited for applications where the states change in a consistent manner. Kalman filter combines all available (noisy) measurements with the mathematical model of the system, and output the best estimate of the next measurement, in such a way that minimizes the error statistically. Even in the presence of statistical noise and erroneous measurements, the Kalman filter estimate the true state values via optimization.

To solve a linear estimation problem using Kalman filter, the following steps are required [165]:

1. Define all components of the difference equation (4.27) and the observation vector (4.28):

$$\mathbf{x}_k = \mathbf{A}\mathbf{x}_{k-1} + \mathbf{B}\mathbf{u}_k + \mathbf{w}_{k-1} \tag{4.27}$$

$$\mathbf{z}_k = \mathbf{H}\mathbf{x}_k + \mathbf{v}_k \tag{4.28}$$

   - $\mathbf{x}$ - State vector ($n \times 1$) containing the variables of interest

- **A** - State transition matrix ($n \times n$)
- **u** - Input vector
- **B** - Input Matrix
- **w** - Gaussian process noise with mean = 0 and covariance = **Q**
- **z** - Observation vector ($m \times 1$) containing the measured variables
- **H** - Observation matrix ($m \times n$) which describes how the measurements **z** are related to the state vector **x**
- **v** - Gaussian measurement noise with mean = 0 and covariance = **R**

2. Define the initial state estimate $\mathbf{x}_0$ and process covariance matrix $\mathbf{P}_0$

3. In the Prediction stage, project the current state and covariance forward to obtain an *a priori* estimate:

   - Project the state ahead:

   $$\hat{\mathbf{x}}_k^- = \mathbf{A}\hat{\mathbf{x}}_{k-1}^- + \mathbf{B}\mathbf{u}_k \tag{4.29}$$

   - Project the process covariance matrix (**P**) ahead. The process covariance matrix P is a measure of the variance of the error between estimated state and measured state:

   $$\mathbf{P}_k^- = \mathbf{A}\mathbf{P}_{k-1}\mathbf{A}^T + \mathbf{Q} \tag{4.30}$$

4. In the Correction stage, incorporate a new measurement to get an improved *a posteriori* estimate

   - Compute the Kalman Gain:

   $$\mathbf{K}_k = \mathbf{P}_k^- \mathbf{H}^T (\mathbf{H}\mathbf{P}_k^- \mathbf{H}^T + \mathbf{R})^{-1} \tag{4.31}$$

- Update the state estimate:

$$\hat{\mathbf{x}}_k = \hat{\mathbf{x}}_k^- + \mathbf{K}_k(\mathbf{z}_k - \mathbf{H}\hat{\mathbf{x}}_k^-) \tag{4.32}$$

- Update the covariance:

$$\mathbf{P}_k = (\mathbf{I} - \mathbf{K}_k\mathbf{H})\mathbf{P}_k^- \tag{4.33}$$

5. Repeat step (3) and (4) for each new iteration k.

The matrices **Q** and **R** are the process noise covariance matrix and the measurement covariance matrix, respectively. Fig. 4.23 illustrates the effects of both covariance matrices on the filtering process. When **Q** is large, the Kalman Filter prioritizes the measured data over the model. Large **Q** corresponds to a larger state covariance matrix **P**, and thus a larger Kalman gain **K**.

R determines how much we trust the mathematical model, over new data input. When **R** is large, the Kalman gain becomes smaller ($\mathbf{K} \to 0$), thus the Kalman filter gives lower weight to new measurements and higher weight to the predicted state $\hat{\mathbf{x}}_k^-$. With low values of R, the Kalman gain gets closer to unity, and thus the filter follows new measurement inputs more closely.

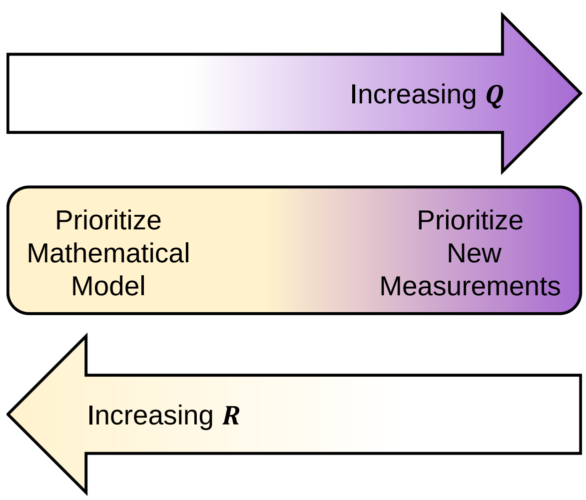

Figure 4.23: Effects of process covariance **Q** and measurement covariance **R** on Kalman Filter operation.

4.9.2 Extended Kalman Filter

For systems represented by non-linear models, the EKF can be applied to linearize the Kalman filter equations about the current mean and covariance. The projection equations (4.29) and (4.30) respectively update to:

$$\hat{\mathbf{x}}_k^- = \mathbf{f}(\hat{\mathbf{x}}_{k-1}^-, \mathbf{u}_k) \tag{4.34}$$

$$\mathbf{P}_k^- = \mathbf{A}_k \mathbf{P}_{k-1} \mathbf{A}_k^T + \mathbf{Q} \tag{4.35}$$

where $\mathbf{f}$ is the non-linear function relating the current state $\mathbf{x}_k$ to the previous state $\mathbf{x}_{k-1}$ and input signal $\mathbf{u}_k$, and $\mathbf{A}_k$ is the Jacobian of partial derivative of the function $\mathbf{f}$ with respect to the states $\mathbf{x}$, evaluated at $\hat{\mathbf{x}}_\mathbf{k}^-$:

4.9.3 Catheter EKF Formulation

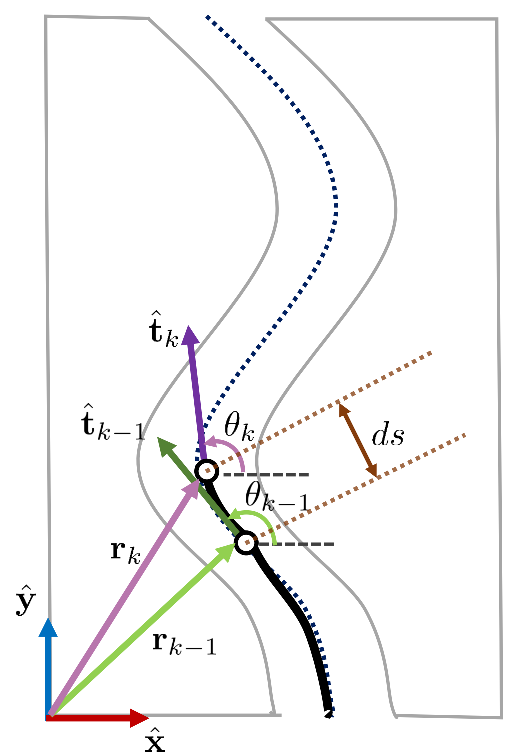

Figure 4.24: Catheter motion state variables

The state vector describing the motion of the catheter during insertion into the vasculature is given by:

$$\mathbf{x} = [x_k, y_k, \theta_k]^T \tag{4.36}$$

where x_k and y_k are the cartesian coordinates of the catheter tip and θ_k is the end effector orientation measured from the $\hat{\mathbf{x}}$ axis at time step k. These variables are illustrated in Fig. 4.24, with $\mathbf{r}(s) = [x(s), y(s)]$.

The tangent vector coordinates given by (4.37) and its relationship to the cartesian position $\mathbf{r}(s)$, derived using backward difference approximation ([166]), is given by (4.38):

$$\hat{\mathbf{t}}_{k-1} = \cos(\theta_{k-1})\hat{\mathbf{i}} + \sin(\theta_{k-1})\hat{\mathbf{j}} \tag{4.37}$$

$$\hat{\mathbf{t}}_{k-1} = \frac{d\mathbf{r}}{ds} \simeq \frac{\mathbf{r}_k - \mathbf{r}_{k-1}}{ds} \tag{4.38}$$

Plugging (4.37) into (4.38) and solving for $\mathbf{r}_k$ yields:

$$\mathbf{r}_k = \begin{bmatrix} x_k \\ y_k \end{bmatrix} = \begin{bmatrix} x_{k-1} + \cos(\theta_{k-1})ds \\ y_{k-1} + \sin(\theta_{k-1})ds \end{bmatrix} \tag{4.39}$$

The orientation of the catheter tip is given by (4.40). The local curvature $\kappa(s)$ is known a priori from the segmentation of the empty vasculature (e.g.: Fig. 4.21(d)). This formulation assumes that the vasculature remains stationary during catheter insertion and that the rate of change in curvature is negligible for the insertion speed and filtering frequency.

$$\theta_k = \theta_{k-1} + \kappa(s)ds \tag{4.40}$$

Thus, the state vector is obtained by plugging (4.39) and (4.40) into (4.36):

$$\mathbf{x}_k = \mathbf{f}(\mathbf{x}_{k-1}, \mathbf{u}_k) = \mathbf{x}_{k-1} + \begin{bmatrix} \cos(\theta_{k-1})ds \\ \sin(\theta_{k-1})ds \\ \kappa(s)ds \end{bmatrix} \tag{4.41}$$

where $\mathbf{u}_k = [ds, \kappa(s)]^T$ is the control input.

The state Jacobian $\mathbf{A}_k$ for the catheter system is given by:

$$\mathbf{A}_k = \frac{\partial \mathbf{f}}{\partial \mathbf{x}}(\mathbf{x}_{k-1}) = \begin{bmatrix} \frac{\partial \mathbf{f}_1}{\partial x_{k-1}} & \frac{\partial \mathbf{f}_1}{\partial y_{k-1}} & \frac{\partial \mathbf{f}_1}{\partial \theta_{k-1}} \\ \frac{\partial \mathbf{f}_2}{\partial x_{k-1}} & \frac{\partial \mathbf{f}_2}{\partial y_{k-1}} & \frac{\partial \mathbf{f}_2}{\partial \theta_{k-1}} \\ \frac{\partial \mathbf{f}_3}{\partial x_{k-1}} & \frac{\partial \mathbf{f}_3}{\partial y_{k-1}} & \frac{\partial \mathbf{f}_3}{\partial \theta_{k-1}} \end{bmatrix} = \begin{bmatrix} 1 & 0 & -\sin(\theta_{k-1})ds \\ 0 & 1 & \cos(\theta_{k-1})ds \\ 0 & 0 & 1 \end{bmatrix} \tag{4.42}$$

where $\mathbf{f} = [\mathbf{f}_1, \mathbf{f}_2, \mathbf{f}_3]^T$ is as defined in (4.41).

The measured states or observation vector $\mathbf{z}_k = [x_k, y_k, \theta_k]^T$ is the output from the catheter tracking using fluoroscopy image segmentation (e.g. Fig. 4.21(a)-(c)). The observation matrix linking $\mathbf{z}$ to the state vector $\mathbf{x}$ is $\mathbf{H} = \mathbf{I}_{3\times 3}$.

4.9.4 Catheter EKF Implementation

We implemented the catheter EKF formulation in MATLAB to follow two paths: a) an arbitrary hand-drawn curve and b) the outline of ICA lateral projection segmented from fluoroscopy imaging (Fig. 4.19)(b). The known path information includes a set of cartesian positions ($\mathbf{x}_{curve}$, $\mathbf{y}_{curve}$), the local tangent angles ($\boldsymbol{\theta}_{curve}$) calculated using forward different approximation, the arc lengths $\mathbf{s}_{curve}$ up to each point, and the local curvature $\boldsymbol{\kappa}_{curve}$ calculated using the angle and arc length information ($\kappa = d\theta/ds$).

The chosen rate of insertion was 3 mm per step, which match the insertion rate used for autonomous insertion in Section 4.10.3. At each step k, the ground truth state $\mathbf{x}_{true}$ is calculated by cubic spline interpolation of the known curve information, at query point s_k.

The model $\mathbf{x}_{model}$ is calculated using (4.41) and the measured states $\mathbf{z}_k$ are calculated by adding gaussian noise to the true states $\mathbf{x}_{true}$. Finally, the EKF states $\mathbf{x}_k$ are calculated using the prediction stage equations ((4.34) and (4.35)) and the correction stage equations ((4.31), (4.32), and (4.33)).

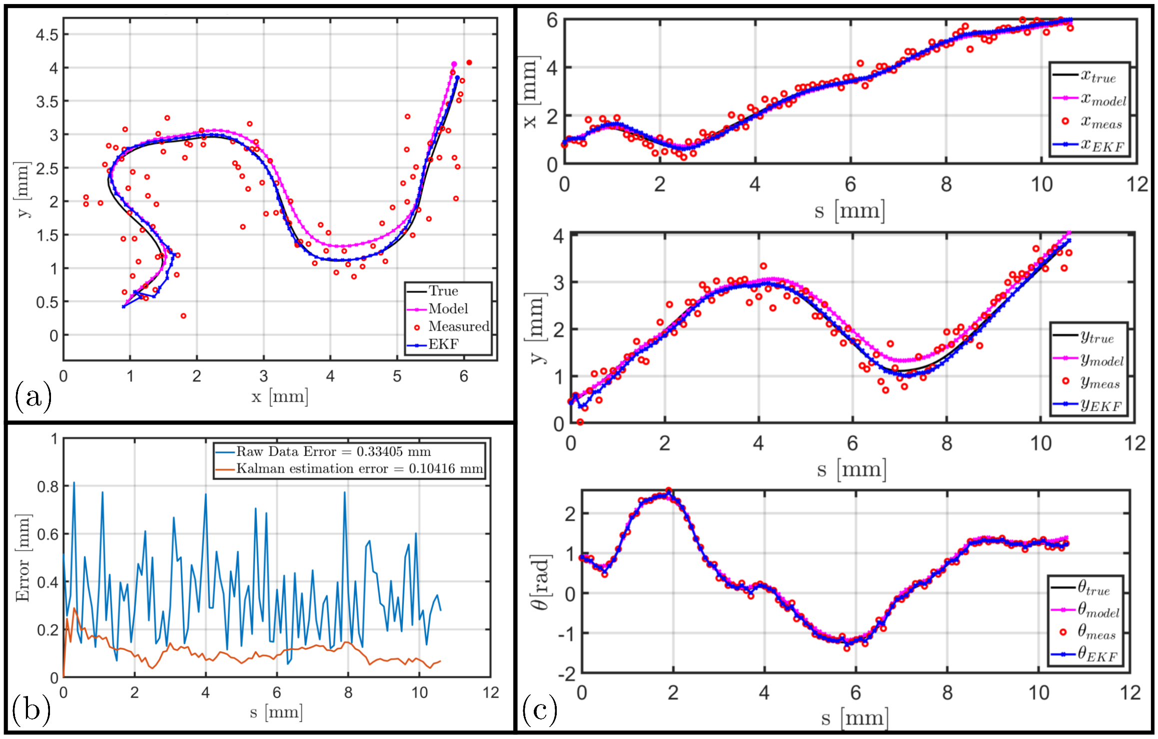

Figure 4.25: EKF results on arbitrary trajectory (a) Trajectory, (b) RMS error, (c) EKF states

Figure 4.25 shows the EKF results on the arbitrary curve. The process covariance matrix $\mathbf{Q}$ and the measurement covariance matrix $\mathbf{R}$ were set as:

$$\mathbf{Q} = \begin{bmatrix} (0.01)^2 & 0 & 0 \\ 0 & (0.01)^2 & 0 \\ 0 & 0 & (0.0175)^2 \end{bmatrix} ; \quad \mathbf{R} = \begin{bmatrix} (0.25)^2 & 0 & 0 \\ 0 & (0.25)^2 & 0 \\ 0 & 0 & (0.0873)^2 \end{bmatrix} \tag{4.43}$$

where each element in the diagonal is the variance (or squared standard deviation) of the uncertainty (in the model or in the measurement) of each state, with units mm^2, mm^2, and rad^2. With these EKF parameters, the tracking error was reduced by 68.8% when compared to raw (noisy) measurements without filtering.

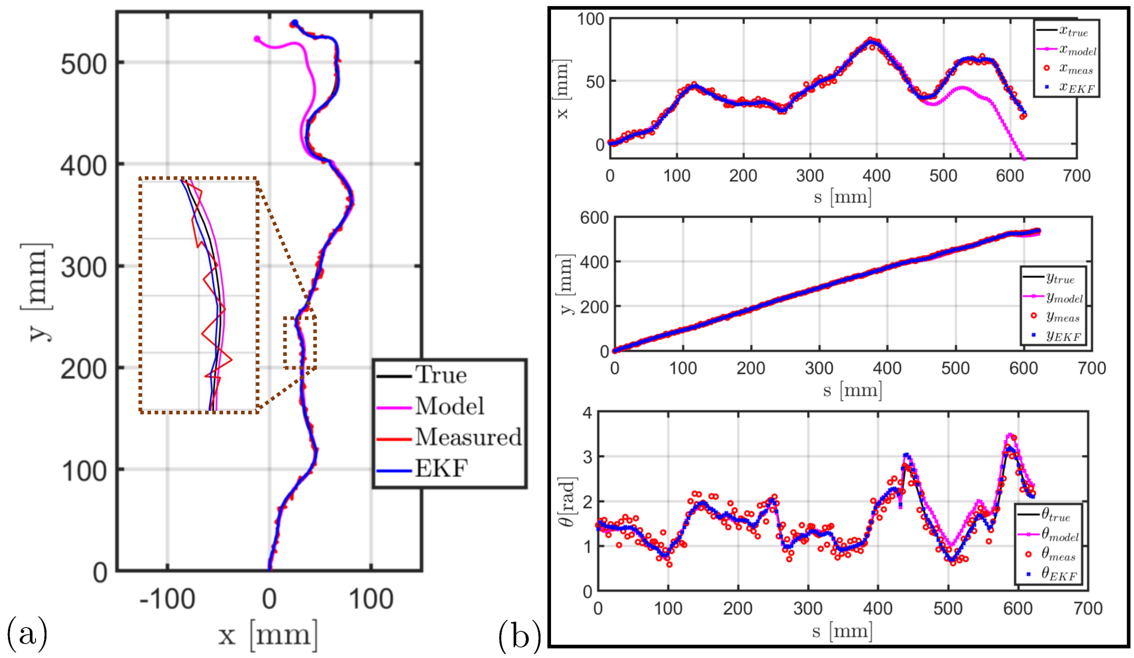

Figure 4.26: EKF results on ICA trajectory (AP view) (a) Trajectory (c) EKF states.

Figures 4.26 and 4.27 show the EKF results when following the projected ICA path. The process covariance matrix $\mathbf{Q}$ was the same as in (4.43) since the model is the same. The measurement covariance matrix $\mathbf{R}$ was updated with increased uncertainty, to match the scale of the ICA curve.

$$\mathbf{R} = \begin{bmatrix} (2)^2 & 0 & 0 \\ 0 & (2)^2 & 0 \\ 0 & 0 & (0.175)^2 \end{bmatrix} \tag{4.44}$$

The resulting tracking error was reduced by 65% when compared to raw measurements without filtering. Future works will integrate this EKF formulation with fluoroscopy image segmentation for in-vitro pose tracking and filtering.

4.10 Validation Experiments

We conducted a series of experiments to validate real-time control of the robotic catheter system. These experiments include branch selection in joint control mode, channel navi-

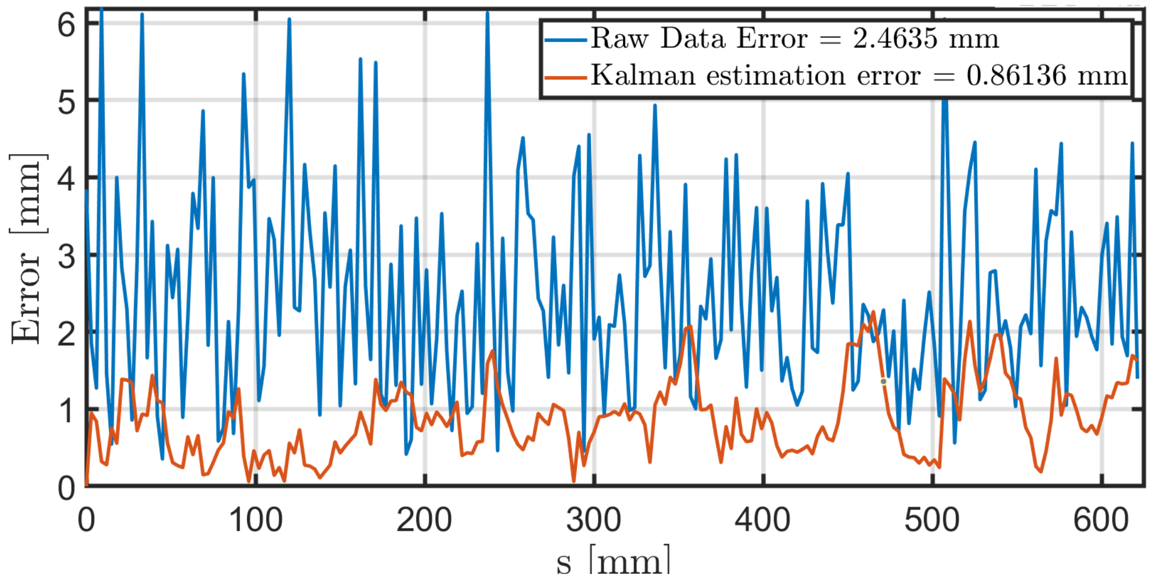

Figure 4.27: Path rms error on ICA trajectory with and without EKF

gation and compliance comparison in admittance control mode, and automatic catheter insertion and self-steering in configuration control mode.

4.10.1 Branch Selection

In Fig. 4.28, we used the robotic catheter in joint control mode to navigate a mock planar vasculature (polyurethane tubing, ID 3.175 mm). The robot was able to steer into both branches of the 60° bifurcation.

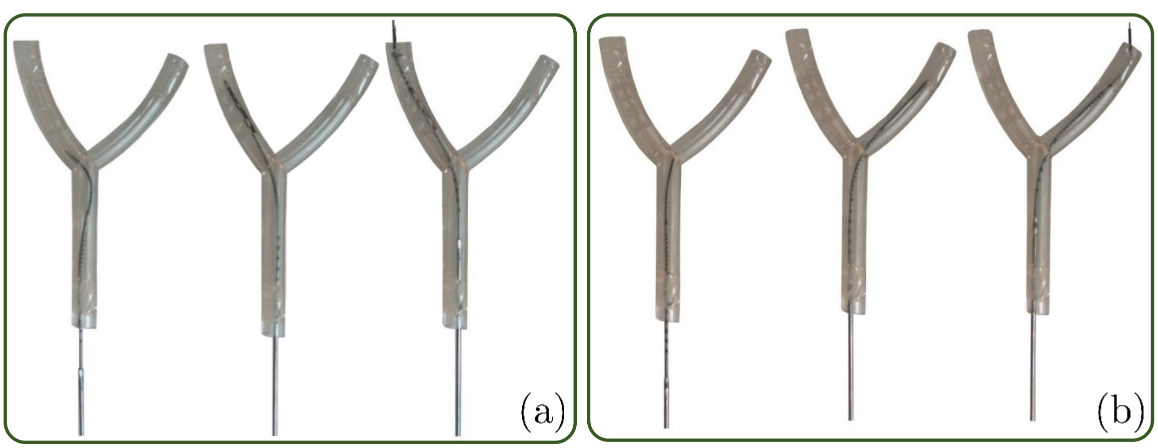

Figure 4.28: Insertion and branch selections (a) left and (b) right using the robotic catheter in joint control mode.

4.10.2 *Active Compliance*

We validated our active compliance approach with two preliminary experiments. In the first experiment, we inserted a catheter into a channel of unknown geometry while applying admittance control to minimize the load on the backbones. We showed that the catheter can actively comply with an unknown constraint as shown in Fig. 4.29(a). By stopping the active compliance and pulling the robot sideways through the channel (which was cut open in its inner radial wall), we can show the extent of active bending of the catheter. Fig. 4.29(b) shows that the catheter has actively bent 81° while experiencing 43° of passive bending due to friction and mechanical losses in our actuation unit.

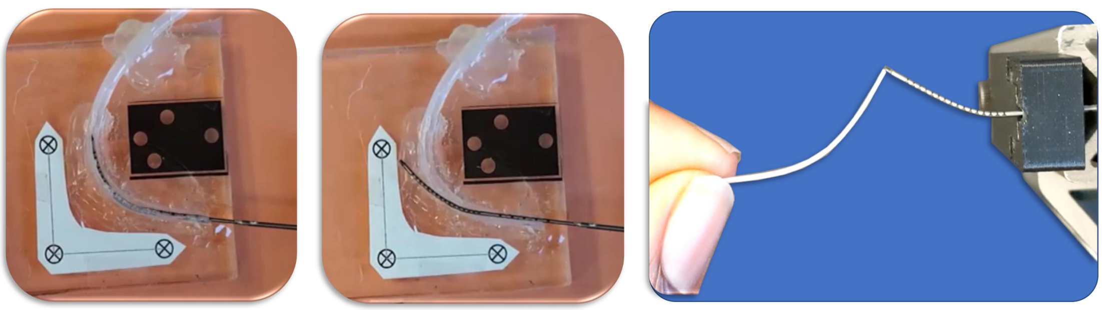

(a) (b) (c)

Figure 4.29: A demonstration of active compliance: (a) The robotic microcatheter is inserted into a curved channel mimicking a curved vessel, (b) the catheter after it was removed through a side slit in the tube and overlaid on the tube. (c) Comparison of our catheter under active compliance (right) vs. the Medtronic Phenom 21 (2.3 Fr (0.76mm)) (left).

In the second experiment, we show a comparison of our catheter under active compliance and being pushed against a 2.3 Fr Medtronic Phenom micro-catheter (Fig. 4.29(c). This result shows that our catheter prototype has similar compliance to commercial micro-catheters. We also measured the minimal tip force needed to trigger active compliance of our catheter and showed that it is close to 0.01 N (1 gram). We plan to improve actuation unit by reducing friction and optimizing spring selection (stiffness). While the springs can be used for force sensing (Hooke's law), for added precision, we plan to integrate load cells for sensing the actuation effort.

4.10.3 Autonomous Insertion and Steering

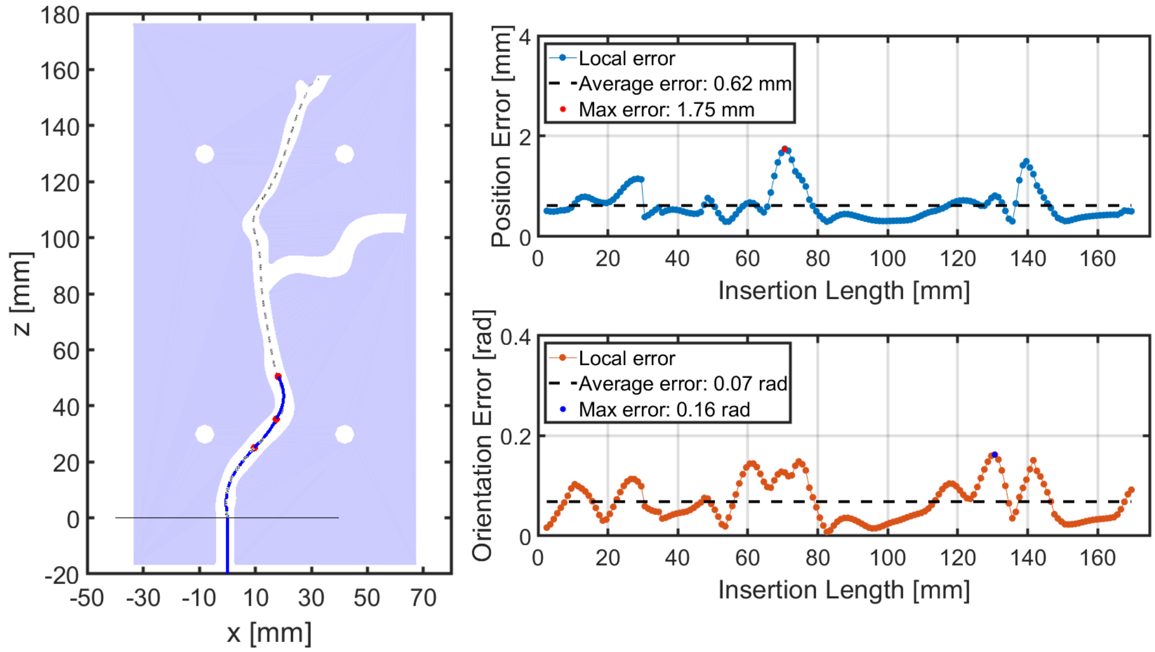

Figure 4.30: (a) Robotic catheter following the 2D ICA path in simulation. (b) Position and orientation errors as a function of insertion length.

The goal of this experiment was to validate the results from the path planner (presented in Section 4.6) on the physical system, and to demonstrate autonomous insertion and steering within a 2D vasculature model. We created this 2D model using a lateral projection of the 3D phantom vasculature, obtained from bi-plane fluoroscopy imaging (Fig. 4.19(b)). This phantom was fabricated by laser cutting the walls of 2D path into an acrylic plate (12.7 mm thick), along with an acrylic cover (2 mm thick). The phantom was mounted on a grid plate and held stationary during catheter insertion.

The trajectory planning algorithm (Fig. 4.13) was use to calculate the joint values and corresponding catheter configurations that minimize the shape error at each insertion step. This path planner uses the nominal model of the catheter (i.e. just the NiTi tip, without system losses), derived via calibration in Section 4.5.2. Inputs to this algorithm included the geometric parameters for our latest catheter prototype ($L_1 = 13$ mm, $L_2 = 16$ mm, $\delta_2 = -0.48$ rad), the penalty ratios ($r_{tp} = 0.75$, $r_{seg} = 1$), the curve parameterization step size ($ds = 0.5$ mm), and insertion step size ($dq_1 = 3$ mm). The joint limit imposed on the nominal model of the catheter were $\| q_2^* \| \leq \pi/2$ rad, $\| q_3^* \| \leq 1$ mm, and $\| q_4^* \| \leq 1$ mm.

Figure 4.31(a) shows the optimal configurations of the steerable catheter as a function of insertion depth. These were output from the path planner (dashed curves) and input into the real-time system (solid curves) in configuration control mode. Fig. 4.31(b) shows the actuation level motion that achieves these configuration. The dashed lines represent the theoretical actuation calculated from the nominal model. The solid lines show the actual joint values needed to achieve these configurations. These joint values were calculated in real-time using the configuration to joint level mapping with actuation compensation, derived in (4.21). The physical joint limits on the actuation unit are -6 mm $\leq q_3 \leq 10$ mm and $\| q_4 \| \leq 5$ mm.

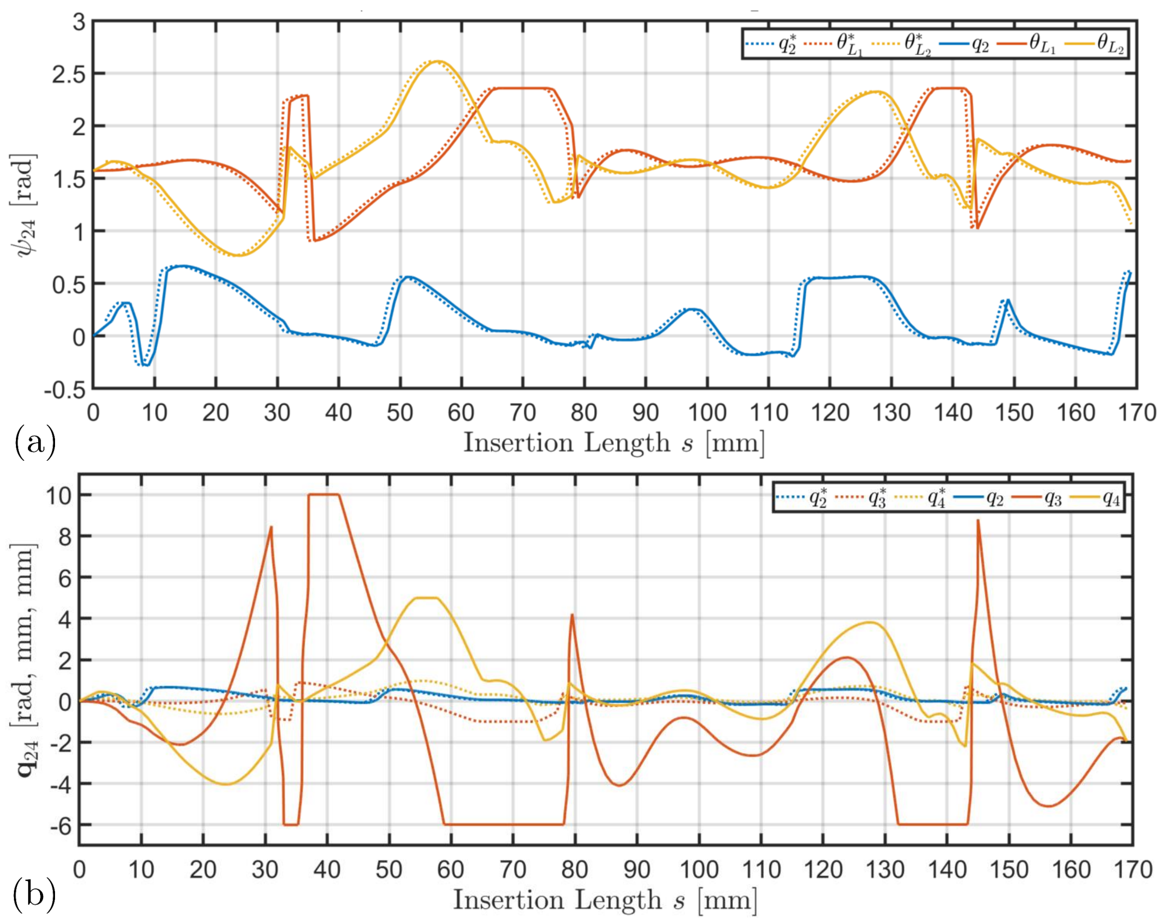

Figure 4.31: (a) Catheter configurations that minimize shaper error during insertion. (b) Joint level motion that achieves these desired configurations. (*) indicates nominal model, without system losses.

Figure 4.32 shows video snapshots of the autonomous catheter insertion and steering. The catheter was able to follow the general shape of the vasculature and steer itself using the pre-planned optimal configurations. However, the catheter deviated from the centerline with larger position errors than predicted from our simulated trajectory following (Fig. 4.30). Our simulation assumes a 1-to-1 mapping between the insertion motion q_1 measured at the motor level, and the insertion length s within the vasculature. However, on the physical system, the insertion motion does not fully translates to insertion length within the vasculature. There are motion losses due to a large portion of the catheter (i.e. the passive catheter extension) floating unconstrained between the actuation unit exit and the vasculature entry point. To overcome this limitation, we plan to integrate a linear potentiometer at the entrance of the vasculature for more accurate measurement of the insertion motion. In addition, we plan to update the pre-operative path plan based on intraoperative information obtained from fluoroscopy imaging. In future works, we will integrate a calibrated statics model of the catheter and use active compliance to minimize interaction forces with the vessel walls.

Figure 4.32: Video snapshots of autonomous catheter insertion and steering in 2D ICA model

4.11 Conclusions

Since 2015, mechanical thrombectomy (MT), i.e. the endovascular retrieval of blood clots using stent retrievers and/or aspiration catheters, has become the recommended standard of care for patients who present with acute large vessel occlusion strokes. However, the recent awareness to the importance of early revascularization via MT stands in contrast to the current availability of this intervention. The widespread availability of MT is hindered by the skill barrier associated with the complexity of navigating and steering through thin, tortuous, and branched vasculature using passive guidewires and catheters.

In this chapter, we introduced our envisioned system for a multi-articulated, actively steerable catheter for future robotic assistance in neuro-endovascular surgery. First, we presented the design, kinematic modelling, and image-based calibration of this robotic catheter. Next, Anonymized CT scans of a patient head and neck were utilized to extract a model of the internal carotid artery (ICA). We proposed a path planning algorithm that computes the joint values that minimize shape deviation at each stage of insertion within a vasculature model. The preoperative path planning problem was casted as a non-linear least squares minimization of the shape error between the catheter and the local vasculature and solved in MATLAB using Levenberg-Marquardt formulation.

The design of multi-articulated catheters for cerebrovascular interventions is especially challenging due to vessel size, vessel tortuosity, and the requirement for an open bore. Regardless of the particular embodiment of a catheter, there is a need for an approach that identifies the ideal catheter design parameters for a given target vasculature. We used the error metrics from this path planner as a design penalty score and computed the optimal catheter design parameters that minimize this score for a given vasculature anatomy. We also explore the potential benefits of adding a passive flexure joint between two planar-bending continuum segments. A simulation study compared the ad-hoc catheter to the optimized catheter with and without flexure. The results from this study suggest that the optimized catheters with and without a passive flexure are able to follow the path with minimal passive deflection of the distal end of the catheter. The initial results suggest the possible utility of this approach for the development of a library of catheters that may be designed a-priori for anatomical regions while taking into account across-patient anatomical variabilities. For clinical-deployment, the same methods can be used to select the best catheter candidate from a library of catheters.

We implemented a multi-mode control scheme for real-time control of the robotic catheter, using Simulink Real-Time on a PC/104 target computer. In addition to the low-level control loop that uses a PID control law to close the error at the joint level, we implemented a mid-level controller that enables the user to control the robot in joint space, configuration space, using admittance control or using telemanipulation. In the future, we plan to integrate a high level controller that will be based on position feedback from the real-time segmentation of the bi-plane fluoroscopy image stream and path planning predictions based on the measured insertion depth.

We experimentally validated the robotic system through a series of experiments, including branch selection, insertion into an unknown channel under active compliance, compliance comparison with existing passive catheters, and autonomous deployment within the 2D vasculature. These experiments informed future improvements needed to optimize our robotic catheter, and confirmed the need for intraoperative update of the path plan using bi-plane fluoroscopy imaging.

We proposed an approach for segmentation and tracking of the catheter outline from bi-plane fluoroscopy images. This approach was implemented *offline* with pre-recorded fluoroscopy images of the mock vasculature. For future *online* segmentation and tracking, a graphical user interface was designed to enable the surgeon to initialize the cropping and segmentation parameters.

We formulated and implemented an Extended Kalman Filter (EKF) model for pose filtering of the catheter during tracking. This formulation was tested in simulation with artificially noisy (gaussian) measurements, and reduced the RMS error by 60%. Future works will integrate this EKF formulation with fluoroscopy image segmentation measurements for in-vitro pose tracking and filtering.

In this chapter, we have presented the design and proof-of-concept of various sub-systems needed for our envisioned catheter deployment strategy (Fig. 4.2). To achieve our main goal of robot-assisted endovascular intervention, a significant research effort is needed for successful integration of these different sub-systems.

CHAPTER 5
TOWARDS SMART ASPIRATION CATHETERS

5.1 Introduction and Motivation

Patient outcomes following endovascular treatment for cerebral ischemic stroke depend heavily on the ischemic time (time from onset of blockage to recanalization) and on the extent of recanalization of the cerebral vasculature. In a recent study by Kunz et al. [80], based on data from the HERMES meta-analysis [43], it was shown that each 10 minute delay in ischemic time correlated with 40 days of added patient disability and $10,000 of added economic burden. "First pass effect" is the achievement of complete revascularization from a single thrombectomy device pass. It has been associated with faster revascularization (i.e. reduce ischemic time), lower mortality, reduced disability rate, and fewer procedural adverse events [81]. However, with the current thrombectomy technique, first pass recanalization is achieved in only 25% of cases [82]. Clot retrieval is abandoned after several time-consuming failed attempts when further benefits of restoring blood flow are outweighed by the surgical risk and the cumulative ischemic burden already suffered by the patient.

First-pass failure is partly due to sensory deficiencies hampering the surgeons' perception. The perception barriers are: 1) lack of simultaneous visualization of clot location and catheter tip in real-time, and 2) lack of sensory feedback about the level of engagement between the catheter tip and the clot. Surgeons currently rely on subjective measures (e.g. lack of blood return in the aspiration catheter [80]) to infer engagement with the thrombus. After aspiration for 2-5 minutes with the clot engaged, the surgeon removes the catheter. If unsuccessful, the process of catheter preparation, endovascular navigation, and suction must be repeated.

In this chapter, we begin to investigate the feasibility of an indirect intraoperative sensing approach with two unprecedented capabilities: 1) estimate the distance between the catheter tip and the blood clot, 2) inform the surgeon about the quality of the engagement of the catheter tip with the clot. The proposed technology has the potential to offer a low-cost rapidly deployable sensory solution that is compatible with existing catheter technology. While our focus application is for stroke care, this indirect sensing method could be applied to the endovascular treatment of aneurysms, arteriovenous malformations (AVM), and arteriovenous fistulae.

To the best of our knowledge, our proposed adaptation of stochastic modeling and machine learning to estimate distance to clot and to classify quality of catheter engagement has not been investigated in the literature. Ultrasonic sensing for flow velocimetry has been developed and explored for the past two decades [76]. The presence of the ultrasonic piezoelectric elements at the catheter tip prevents miniaturization while retaining a hollow and flexible tip. Such catheters have been used for cardiac applications [77][78]. Miniature intravascular ultrasound (IVUS) ablation and imaging catheters (e.g. Boston Scientific's Ultra-ICETM) lack the necessary tip flexibility and a working bore.

The goal of this research effort was to investigate an indirect sensing method to estimate the proximity and engagement between the distal tip of an aspiration catheter and a blood clot during neuro-endovascular surgery. The driving hypothesis is that this sensory feedback can increase the probability of successful clot retrieval. To achieve this goal, we plan to 1) investigate the pressure loss during pulsatile vacuum excitation as a function of distance between the catheter tip and a mock clot lodged a vasculature model, 2) investigate the effect of pulsatile vacuum excitation on catheter-clot engagement, and 3) investigate and develop a classification frame works for engagement quality (good vs bad) based on the pressure loss.

5.2 Methods

Aspiration thrombectomy refers to the endovascular retrieval of a cerebral blood clot using suction force applied via an aspiration catheter. The aspiration catheter is deployed from the femoral access in the leg to the site of occlusion in the brain, as shown in Fig. 4.1)(a). Once engagement with the clot is inferred, the surgeon apply a constant suction force using a vacuum pump (e.g. Penumbra pump) or more commonly a 60 mL Vacloc syringe. Prior works [167, 168] have experimentally determined that the vacuum level applied during aspiration thrombectomy ranges between -0.91×10^5 Pa to -0.78×10^5 Pa. The vacuum lines are filled with saline to prevent accidental injection of air bubbles into the blood stream. We replicated this setup ex-vivo and enhanced it with sensing modalities, with the eventual goal of providing predictive information to the surgeon during aspiration thrombectomy.

5.2.1 Experimental Setup

Figure 5.1 shows our experimental setup for smart aspiration thrombectomy. We replaced the manually suction force with an oscillating suction force applied using a linear actuator. This sinusoidal motion is commanded using Simulink Real-Time deployed on a PC/104 target computer. A pressure sensor (Honeywell, 26PCCFB2G, $\pm 1.03 \times 10^5$ Pa) measures the applied pressure at the proximal (extracorporeal) end of the aspiration catheter. The setup also includes a linear potentiometer that measures the catheter insertion into the vasculature. The data from both sensors are logged to the PC/104 computer via 16-bit analog inputs.

The intracorporeal portion of the setup consists of a mock vasculature filled with water and sealed at its distal end with mock blood clot. Its proximal end is sealed with an introducer sheath (e.g. Glidesheath slender), through which an aspiration catheter (e.g. Medtronic React 68) is inserted. This setup mimics the clinical practice of using an introducer sheath to keep the femoral artery sealed during endovascular interventions.

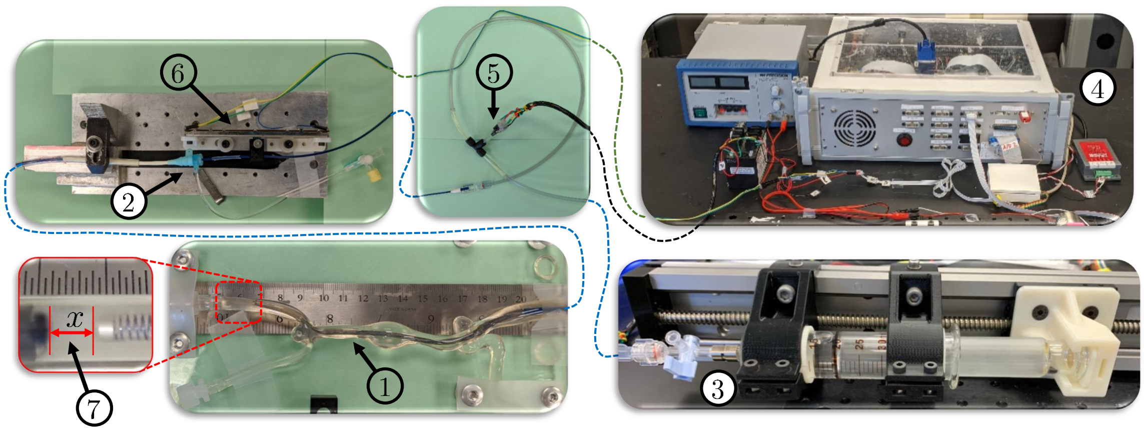

Figure 5.1: Experimental setup for smart aspiration thrombectomy: An aspiration catheter is inserted into a mock vasculature ① via an introducer sheath ② and system is filled with water to replicate the clinical setup. A glass syringe ③ is used to apply a negative pressure, at the distal end of the catheter. The syringe barrel is fixed and plunger is actuated using a linear actuator. The motion profile of the syringe is controlled using a PC-104 target computer ④. A pressure sensor ⑤ measures the vacuum applied by the syringe at the distal end of the catheter. A linear potentiometer ⑥ records the insertion of the catheter. A camera is used to measure the catheter-clot distance ⑦.

The blood clot in our setup is simulated by plugging the water-filled vasculature with a metal rod. Eventually, once the system is fully characterized and optimized, we will replace this rod with more standard blood clot models (e.g. [169, 170, 171]). We have started investigating the use of coagulated porcine blood as clot phantoms, as shown in Fig. 5.2. While this phantom is adequate for our needs, we opted for a less biohazardous model for the initial investigation. Future works will also explore methods for repeatable positioning and adhesion of the blood clots within the phantom vasculature.

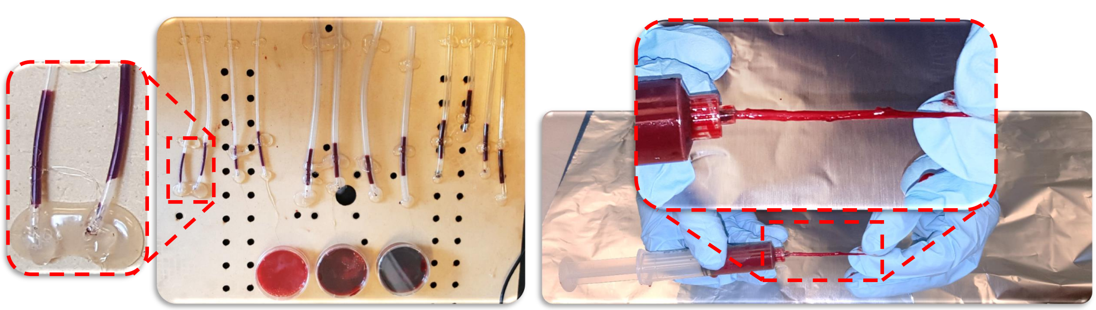

(a) (b)

Figure 5.2: Blood clot fabrication using coagulated swine blood: (a) clots coagulated inside different diameter Tygon tubes, (b) a sample clot tested for consistency by clinical collaborator

Figure 5.3 shows the various vasculature phantoms explored for this application. The rubber tubing model (a) is softer than arterial vessel, and is thus not a good phantom option. The branched commercial model (b) mimics the texture and geometry of blood vessels and will be the vasculature of choice once the system is optimized. For initial testing, we opted for the Tygon vasculature model (c), as it has a texture similar to the commercial model and can be kept in a straight configuration to minimize friction effects that can mask traction forces experienced by the clot.

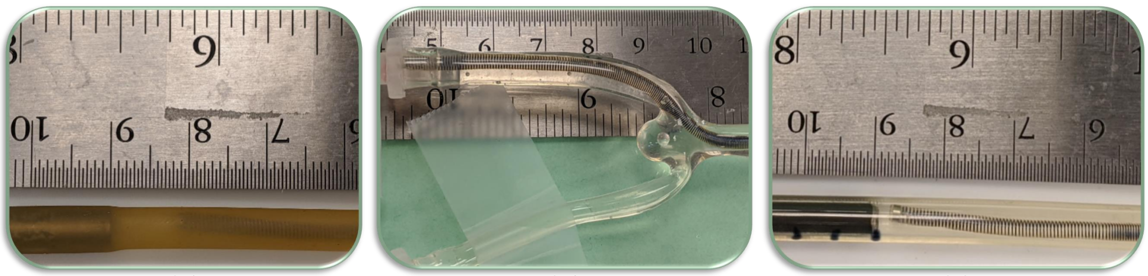

(a) (b) (c)

Figure 5.3: Vasculature models for smart aspiration thrombectomy. (a) commercial branched model with aneurysm, (b) Tygon tubing model (ID 3.175 mm), (c) Rubber tubing model (ID 3.175 mm).

We also explored different actuation options for pulsating the syringe. Our first prototype was a low-cost slider-crank mechanism (see Fig. 5.4(a)) actuated by a servo motor (Jameco Electronics, HN-GH12-1926Y). The motion of the syringe plunger was measured using an optical encoder (Moticont, OEM-030U-01, 30μm resolution) mounted externally and logged on the PC104 via an analog input. The frequency of the oscillation was set by the voltage input to the motor (directly from a power supply) and its amplitude was set using an adjustment feature in the crank mechanism. While this actuation method was functional, we needed a more robust and repeatable way of commanding the syringe motion.

In our second prototype (see Fig. 5.4(b)), the syringe was actuated using a high speed linear actuator (Firgelli Automations, FA-RA-22-12-2). The sinusoidal motion of this motor was controlled in real time using a PID control law on the PC/104 computer. The current required for this motor (5A) exceeded the limits of the PC/104's servo amplifiers (LSC 30/2, $I_{max} = 2$A), so we connected the analog output from the PC/104 to an external amplifier (Dimension Engineering, Sabertooth 2×5) to drive the motor. The syringe motion was captured by the same Moticont optical encoder. Unfortunately, the backlash in this motor exceeded the commanded range of motion of the syringe, which resulted in unreliable syringe position measurements.

Figure 5.4(c) shows our current actuation method, which is a precision lead screw with a ball bearing carriage (McMaster, 6734k34) connected to a DC motor (Maxxon group 369848). This motor and its internal encoder interfaces well with the PC/104, and removed the need for the external encoder and external amplifier. We also opted to use replace the Vacloc syringe with a glass syringe (Zoro, G4824206), as we noticed motion losses at high frequencies due to the rubber interface between the plunger and the barrel.

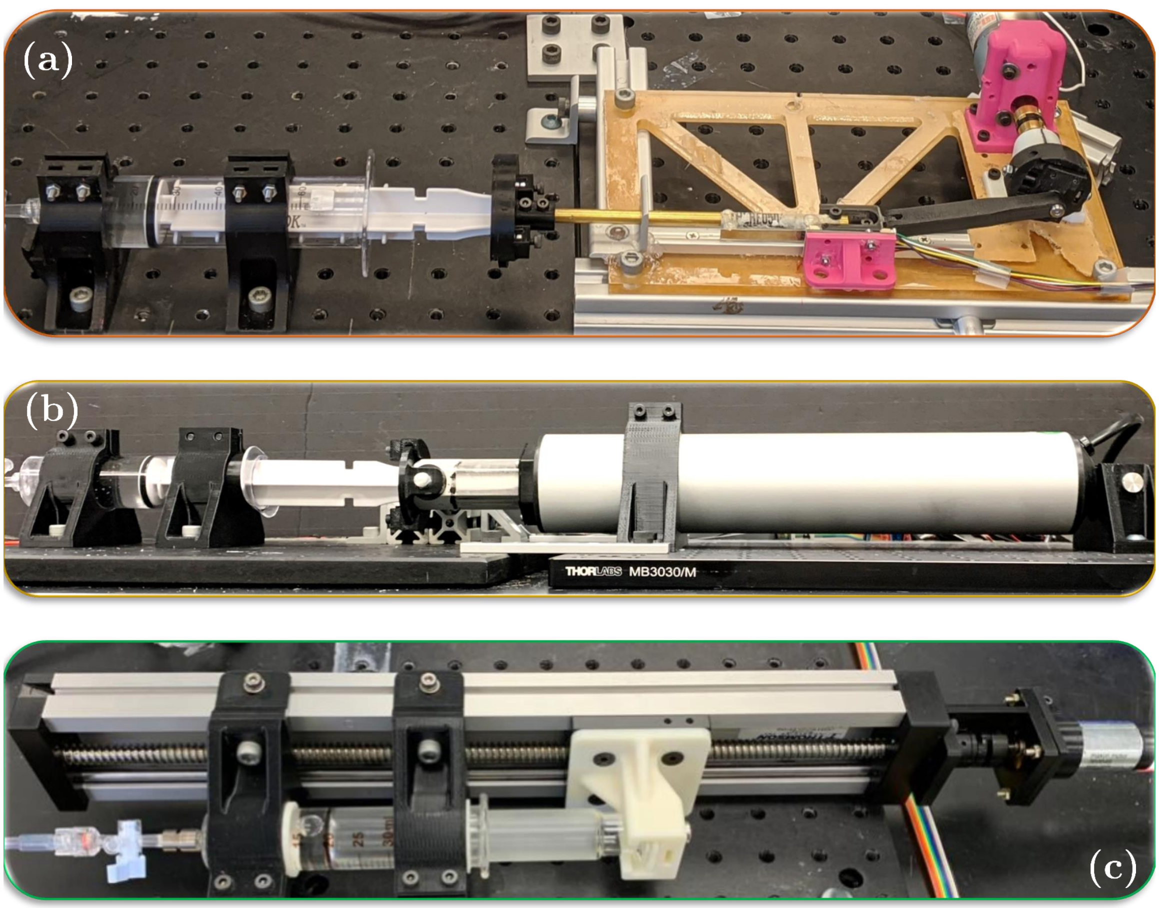

Figure 5.4: Actuation methods tested for pulsatile excitation: (a) Low-cost slider-crank mechanism, (b) High speed linear actuator, (c) Precision lead screw.

5.2.2 *Data Collection Procedure*

Using the setup shown in the Fig. 5.1 and a tygon tubing vasculature model, we applied a pulsating vacuum using the syringe and collected sensor data for different experimental conditions. This experiment was done in the following sequence:

1. The vasculature, aspiration catheter and syringe system are filled with water to create a closed system. Multiple syringes and 3-way valves are used release any air bubbles from the loop.

2. The aspiration catheter is placed at a set distance from the clot. This distance was recorded using a camera, with a ruler in the frame for scale.

3. The syringe is commanded to pulsate at a set frequency and amplitude for 10 seconds. The commanded profile is a time-base sinusoidal function:

$$q_{des} = A \sin\left(2\pi f t + \frac{\pi}{2}\right) - A \tag{5.1}$$

   where A is the amplitude and f is the frequency. The syringe motion starts at its home position and its motion ranges from 0 to $-2A$, thus generating a negative pressure (vacuum) on the system.

4. The syringe motion, the pressure data, and catheter insertion data are logged into the PC/104.

5. Steps 2-4 are repeated for different catheter-clot distances and motion frequencies.

5.3 Results

Using the presented data collection procedure, we commanded the syringe to move with $A = 0.1$ mm and frequencies 4 Hz, 6 Hz and 8 Hz, successively. The catheter was positioned at different distances from the clot, ranging from 10 mm to 0 mm. We recorded sensor data for each of these experimental conditions.

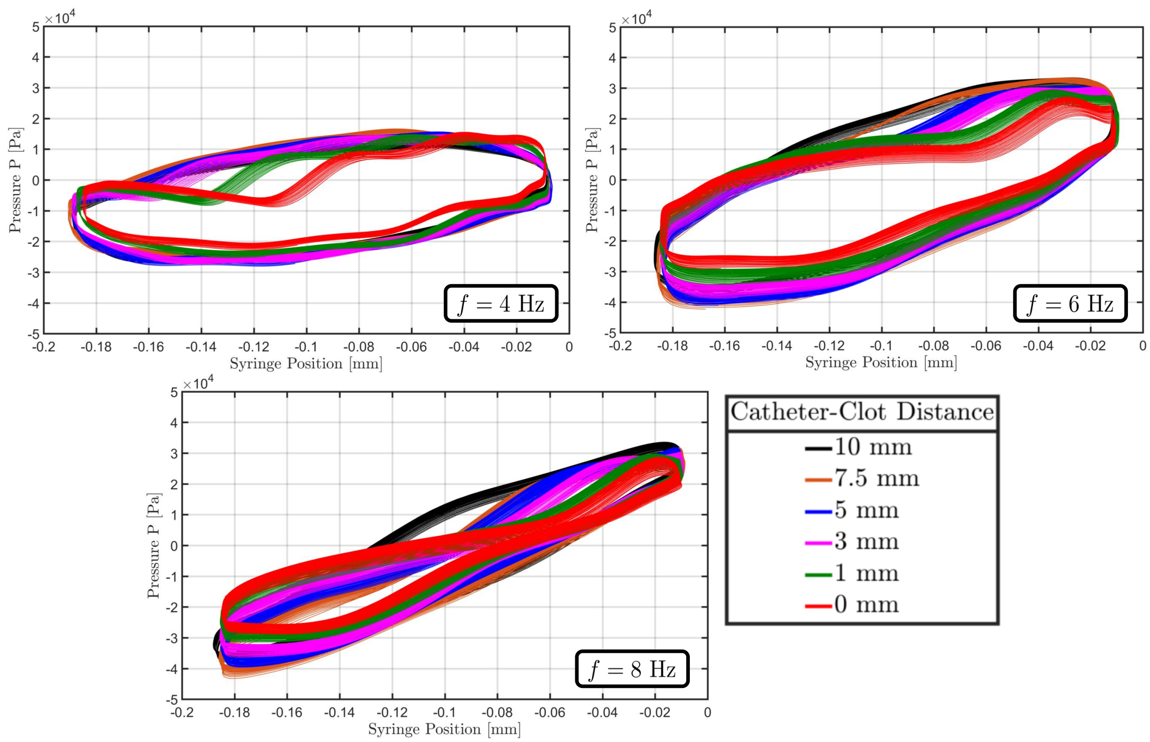

Figure 5.5: Pressure profiles as a function of syringe displacement and catheter-clot proximity, for three oscillation frequencies (4Hz, 6Hz, 8Hz)

Figure 5.5 shows the resulting pressure profiles as a function of syringe motion and catheter-clot proximity. These plots show that the pressure traces are ordered as a function of catheter-clot proximity. We also notice a slope increase in the pressure profiles as the frequency of syringe oscillation increases. Further analysis is required to interpret the trends observed from this data. The data should be used to obtain a statistical model of the system and tune a support vector classifier. In addition, a computational fluid dynamics model for the pulsatile flow and pressure transmission model should be investigated. Nevertheless, these preliminary results suggest that there may be a path forward in using pulsatile pressure excitation as a tool to measure catheter-clot proximity during aspiration thrombectomy.

5.4 Conclusions

In stroke care, early and complete revascularization are the strongest indicators of good clinical outcome for the patient. With the current clinical standard, first-pass recanalization is only achieved in 25% of cases. This is partially due to sensory deficiencies hampering the surgeon's perception about the clot location relative to the aspiration catheter tip, and the level of contact between the catheter and the clot. The overarching goal of this research effort is augment the current aspiration thrombectomy setup with sensory feedback and quantitative metrics to gauge catheter-clot proximity and engagement.

In this chapter, we have conducted a preliminary feasibility study for the proposed smart aspiration setup. We have developed a low-cost apparatus that supports controllable vacuum excitation and sensing. We have explored different phantom vasculature model and fabricated mock thrombus from coagulated porcine blood. Using this platform, we have collected experimental data with different sinusoidal vacuum excitation profiles. Our results suggest that there may be a relationship between the catheter-clot proximity, the pressure profile, and the excitation frequency. A significant research effort is still needed to extract this relationship, including a statistical model of the system and a computational fluid dynamics model to characterize the pulsatile flow within the system.

CHAPTER 6
CONCLUSIONS

6.1 Summary of Findings

Thanks to their distal actuation and high dexterity, continuum robots are able to perform navigation and manipulation tasks that would be too challenging for conventional rigid-link robots. This dissertation explored the design and sensing requirements for using continuum robots in confined spaces and near human anatomy. We focused on two applications that vary in scale but share the need for continuum robots with integrated sensing and adaptable behaviors. On the macro scale, we investigated continuum robots for human-robot interaction in confined spaces. On the sub-millimeter scale, we proposed a robotic catheter system and perception augmentation to improve stroke interventions.

The deployment of continuum robots in confined spaces for collaborative manufacturing can help alleviate the physiological burden on workers and reduce the incidence of work-related musculoskeletal disorders. As a means for enabling such interactions, Chapters 2 and 3 presented continuum robots with adaptable behaviors and integrated sensing for increased safety and optimal task execution.

Current continuum robots designs are limited to a constant cross-sectional diameter. The ability to actively change the diameter of continuum robots would expand the repertoire of kinematic redundancy and enable kinematic parameter adaptation to optimize performance. In Chapter 2, we explored this alternative design option by integrating circular angulated scissor linkages into the structure of continuum robots. We presented the kinematic analysis of this design, along with an exploration of admissible design parameters values for a given continuum robot segment with a desired maximum curvature. We proposed a strategy for using this additional degree of redundancy to minimize joint forces and avoid joint limits. The simulation results showed diameter adaptability can significantly reduce the joint forces, while preserving workspace. The contributions from this chapter are a first step towards continuum robots with situational awareness that will utilize adaptable behaviors for optimized task execution.

Safe human-robot interaction requires robots endowed with perception. In Chapter 3, we presented the design of a multi-modal sensory array for continuum robots, targeting operation in semi-structured confined spaces with human users. These sensors integrate into the body of continuum robots and endow them with proximity sensing, contact detection and localization, force sensing and mapping capabilities. We presented the characterization and calibration of the sensing modalities within this array, along with the communication protocol and multiplexing scheme used to allow an interactive rate of communication with a high-level controller. We integrated these sensors on an industrial manipulator and within the structure of a continuum robot, and demonstrated active mapping of a mock confined space and human-robot interaction. We believe that this technology is a significant step towards a novel class of continuum robots that can be deployed in confined spaces, intelligently interact with their environment, and safely assist a co-located worker.

Endovascular interventions for ischemic stroke requires dexterous manipulation of catheters and guidewires. Robot-assisted steerable microcatheters can facilitate navigation along tortuous vasculature and bifurcation selection, thereby reducing the surgical skill demands and expanding the availability these interventions. In Chapter 4, we proposed a novel multi-articulated robotic catheter that meets the size and steerability requirements for neuronavigation. We presented the design, non-linear kinematic modelling, and image-based calibration of this system. We segmented a 3D model of the internal carotid artery, which we used to create virtual and physical phantom vasculature models needed for path planning and system evaluation. We proposed a path planning algorithm that uses pre-operative CT information to compute the joint values that minimize shape deviation between the catheter and vasculature path. An optimization of the catheter design parameters including the continuum segment lengths and the angular offset of their respective bending planes was carried out using an algorithm based on the Nedler-Mead Simplex method for minimizing a path-specific design error score. A simulation study showed the effectiveness of this algorithm, by comparing the path following errors for the baseline ad-hoc catheter design against the optimized catheter design.

The steerable catheter is actuated using a custom-designed 4-DoF actuation unit with series elastic elements for active compliance and safety. A multi-mode control algorithm was implemented for real-time control of this system, using Simulink Real-Time on a PC/104 computer. We performed a preliminary validation of this robotic system through experiments demonstrating branch selection, insertion in an unknown channel under active compliance, and autonomous deployment within a 2D vasculature model.

For future image-guided steering and intraoperative updates of the path plan, we proposed a method for segmenting the vasculature path and tracking the catheter using fluoroscopy imaging. We also presented a formulation for Extended Kalman Filter for future catheter pose tracking and filtering.

In addition to manipulation challenges, neuro-interventionalists also face sensory limitations during endovascular procedures. Using bi-plane fluoroscopy imaging, the surgeon has a vague, but unprecise, knowledge of the relative position between the catheter tip and target clot. This perception barrier is partially responsible for the high failure rate (75%) of first-pass recanalization attempts. In Chapter 5, we explored the feasibility of using pressure data from an oscillating vacuum as a predictive metric for catheter-clot proximity and quality of engagement. We developed a low-cost testing apparatus that supports this controllable vacuum excitation and testing. We collected an initial set of data that seem to indicate a relationship between the catheter-clot proximity and the commanded excitation profile.

6.2 Future Research Directions

The contributions of this work will allow future continuum robots to operate more safely around workers and to use sensing combined with imaging to actively steer within blood vessels. For the manufacturing-related application of sensing, we have established the feasibility of a novel multi-modal sensory array that endows these robots with contact, force, and proximity sensing along their lengths. Future research questions relate to the optimal use of this sensory array for environmental mapping and localization. The motion profile of the continuum robot during mapping affects the precision of the environment mapping because the time of flight sensors have pre-determined sensory error map as determined in Chapter 3. With this distributed sensing along a continuum robot, one then may ask the question of how to use redundancy resolution to maximize mapping information while minimizing the measurement noise. Furthermore, the uncertainty in the shape of the continuum robot affects the mapping accuracy and one needs to consider in the control strategy of these robots how to include this information as part of the motion optimization scheme for these robots.

For the ischemic stroke work presented in this dissertation, there are several open-ended research problems that remain. Although we have shown sub-system design and proof-of-concept results, our overarching goal of robot-assisted endovascular intervention will require a significant research effort for successful integration. Bi-plane image segmentation and pose filtering need to be merged into the control algorithm of the catheter. There are two ways to merge the fluoroscopy information with the controller: 1) implement 3D reconstruction from 2D biplane fluoroscopy imaging, or 2) implement a controller that fuses error information from the two image planes to deduce a local correction of the catheter motion in 3D. This may be achieved via two local controllers that operate in each image plane and then are weighted based on a 3D projection map that takes into account the 3D kinematics of the catheter. In addition to this challenge, the 3D tracking of the state of a catheter that may be subject to twisting motion remains a challenging problem. One may consider in the future the use of helical radiopaque markers to be embedded on the catheter body to give local rotation information about the axis.

The ways in which active compliance and assistive virtual fixtures for catheters endowed with active compliance remains an open research question. The extent to which a user may be left to their own devices to steer a catheter v.s. using semi-automation remains to be explored in future user studies.

Finally, we have explored the possible use of oscillatory vacuum as a way to estimate the distance from the clot and to verify the quality of clot engagement. We have explored the excitation frequency ranges of 0.5 to 12 Hz and found dependence of the results on the excitation frequency. Our preliminary results weakly suggest that this approach may work provided the type of oscillation is adaptive as a function of distance, and that the system inducing the oscillation has the necessary mechanical bandwidth to achieve very accurate motion control at a reasonable frequency of oscillation.

CHAPTER 7
PUBLISHED WORK

7.1 Journal Publications

1. **Abah, C.**, Orekhov, A., Johnston, Simaan, N., "A Multi-Modal Sensor Array for Human-Robot Interaction and Confined Spaces Exploration Using Continuum Robots", *IEEE Sensors Journal*(2021).

2. **Abah, C.**, Jared P. Lawson, Rashid M. Yasin, Chitale, R., Simaan, N., "Self-steering Catheters for Neuroendovascular Interventions", in preparation, *The International Journal of Robotics Research*.

7.2 Conference Publications

1. **Abah, C.**, Chitale, R., Simaan, N., "Image-Guided Optimization of Robotic Catheters for Patient-Specific Endovascular Intervention", *the International Symposium on Medical Robotics (ISMR)*, Atlanta, GA, 2021.

2. Orekhov, A. L., Johnston, G. L., **Abah, C.**, "An In-situ Collaborative Robot for Manufacturing in Confined Spaces" in ASME IDETC 2021: Student Mechanism & Robot Design Competition (SMRDC), August 2021 (*1st Place*).

3. **Abah, C.**, Del Giudice, G., Shihora, N., Chitale, R., Simaan, N., "Towards Semi-Automated Mechanical Thrombectomy: Path Planning Considerations for a Double Articulated Microcatheter", *the Hamlyn Symposium on Medical Robotics* (p. 67), London, UK, 2019.

4. **Abah, C.**, Orekhov, A., Johnston, G., Yin, P., Choset, H., Simaan, N., "A Multi-Modal Sensor Array for Safe Human Robot Interaction and Mapping", *IEEE Inter-*

national Conference on Robotics & Automation (ICRA), Montreal, Canada, 2019.

5. Orekhov, A.L., Johnston, G.L., **Abah, C.**, Choset, H. and Simaan, N., "Towards collaborative robots with sensory awareness: preliminary results using multi-modal sensing". ICRA 2019 workshop on "Physical human-robot interaction: a design focus", Montreal, Canada, 2019.

6. **Abah, C.**, Orekhov, A., Simaan, N., "Design Considerations and Redundancy Resolution for Variable Geometry Continuum Robots", *IEEE International Conference on Robotics & Automation (ICRA)*, Brisbane, Australia, 2018.

7. Yasin, R., Wang, L., **Abah, C.**, Simaan, N., "Using Continuum Robots for Force-Controlled Semi-Autonomous Organ Exploration and Registration", the International Symposium on Medical Robotics (ISMR), Atlanta, GA, 2018 (*finalist for best student paper award*).

7.3 Book Chapters

1. Orekhov, A., **Abah, C.**, Simaan, N., "Snake-Like Robots for Minimally Invasive, Single Port, and Intraluminal Surgeries", *The Encyclopedia of Medical Robotics. World Scientific* (2018): 203-243.

7.4 Patents and Invention Disclosures

1. Simaan, N., Del Giudice, G., **Abah, C.**, Chitale, R., "Smart Multi-Articulated Catheters with Safety Methods and Systems for Image-guided Collaborative Intravascular Deployment", International Application PCT/US2020/051009, *published* as #WO/2021/055428.

2. Simaan, N., **Abah, C.**, Chitale, R., Luo, H., "Smart Catheters: Assistive Perception for Effective Thrombus Retrieval and Aneurysm Embolization", Vanderbilt Invention Report VU21036, filed 10/23/2020.

3. Simaan, N., **Abah, C.**, Orekhov, A., "Continuum Robots with Adaptive Geometry and Performance Characteristics" Vanderbilt Invention Report VU181716, filed 05/17/2018.

BIBLIOGRAPHY

[1] C. Abah, G. D. Giudice, R. Chitale, and N. Simaan, "Towards Semi-Automated Mechanical Thrombectomy: Path Planning Considerations for a Double Articulated Microcatheter," in *Hamlyn Symposium on Surgical Robotics*, (London, UK), pp. 67–68, 2019.

[2] T. M. Dumont, M. Mokin, G. C. Sorkin, E. I. Levy, and A. H. Siddiqui, "Aspiration thrombectomy in concert with stent thrombectomy," *Journal of NeuroInterventional Surgery*, vol. 6, pp. e26–e26, may 2014.

[3] L. H. de Castro-Afonso, G. S. Nakiri, L. M. Monsignore, P. T. Cougo-Pinto, F. A. Dias, F. Aléssio-Alves, O. M. Pontes-Neto, and D. G. Abud, "The direct first pass aspiration technique in the treatment of acute ischemic stroke resulting from large vessel occlusions," *Arquivos de Neuro-Psiquiatria*, vol. 75, no. 7, pp. 412–418, 2017.

[4] G. Michalos, S. Makris, N. Papakostas, D. Mourtzis, and G. Chryssolouris, "Automotive assembly technologies review: challenges and outlook for a flexible and adaptive approach," *CIRP Journal of Manufacturing Science and Technology*, vol. 2, pp. 81–91, jan 2010.

[5] B. Singh and N. Sellappan, "Evolution of Industrial Robots and their Applications," *International Journal of Emerging Technology and Advanced Engineering Website: www.ijetae.com ISO Certified Journal*, vol. 9001, no. 5, pp. 1–6, 2013.

[6] S. Laster, "Military Robots and Drones: A Reference Handbook," *Reference Reviews*, vol. 28, pp. 16–17, jan 2014.

[7] A. Seeni, B. Schäfer, B. Rebele, and N. Tolyarenko, "Robot mobility concepts

for extraterrestrial surface exploration," *IEEE Aerospace Conference Proceedings*, pp. 1–14, 2008.

[8] R. Taylor, "A Perspective on Medical Robotics," *Proceedings of the IEEE*, vol. 94, pp. 1652–1664, sep 2006.

[9] C. Bergeles and Guang-Zhong Yang, "From Passive Tool Holders to Microsurgeons: Safer, Smaller, Smarter Surgical Robots," *IEEE Transactions on Biomedical Engineering*, vol. 61, pp. 1565–1576, may 2014.

[10] G. Robinson and J. B. C. Davies, "Continuum robots-a state of the art," in *Proceedings 1999 IEEE international conference on robotics and automation (Cat. No. 99CH36288C)*, vol. 4, pp. 2849–2854, IEEE, 1999.

[11] S. Kolachalama and S. Lakshmanan, "Continuum robots for manipulation applications: A survey," *Journal of Robotics*, vol. 2020, 2020.

[12] A. L. Orekhov, C. Abah, and N. Simaan, "Snake-like robots for minimally invasive, single-port, and intraluminal surgeries," in *Transportation Research Procedia*, vol. 25, pp. 203–243, oct 2018.

[13] J. Burgner-Kahrs, D. C. Rucker, and H. Choset, "Continuum Robots for Medical Applications: A Survey," *IEEE Transactions on Robotics*, vol. 31, pp. 1261–1280, dec 2015.

[14] V. Villani, F. Pini, F. Leali, and C. Secchi, "Survey on human–robot collaboration in industrial settings: Safety, intuitive interfaces and applications," *Mechatronics*, vol. 55, no. June 2017, pp. 248–266, 2018.

[15] M. Lorenzini, W. Kim, E. D. Momi, and A. Ajoudani, "A New Overloading Fatigue Model for Ergonomic Risk Assessment with Application to Human-Robot

Collaboration," in *2019 International Conference on Robotics and Automation (ICRA)*, vol. 25, pp. 1962–1968, IEEE, may 2019.

[16] M. T. Froehler, J. L. Saver, O. O. Zaidat, R. Jahan, M. A. Aziz-Sultan, R. P. Klucznik, D. C. Haussen, F. R. Hellinger Jr, D. R. Yavagal, T. L. Yao, *et al.*, "Interhospital Transfer Before Thrombectomy Is Associated With Delayed Treatment and Worse Outcome in the STRATIS Registry (Systematic Evaluation of Patients Treated With Neurothrombectomy Devices for Acute Ischemic Stroke)," *Circulation*, vol. 136, pp. 2311–2321, dec 2017.

[17] T. S. Harmon, P. C. Hulsberg, J. R. McFarland, V. V. Villescas, and J. Matteo, "Time is Brain: The Future for Acute Ischemic Stroke Management is the Utilization of Steerable Microcatheters for Reperfusion," *Cureus*, vol. 11, no. 1, pp. 1–12, 2019.

[18] N. Simaan, R. Taylor, and P. Flint, "A dexterous system for laryngeal surgery," in *Robotics and Automation, 2004. Proceedings. ICRA'04. 2004 IEEE International Conference on*, vol. 1, pp. 351–357, IEEE, 2004.

[19] T.-D. Nguyen and J. Burgner-Kahrs, "A tendon-driven continuum robot with extensible sections," in *Intelligent Robots and Systems (IROS), 2015 IEEE/RSJ International Conference on*, pp. 2130–2135, IEEE, 2015.

[20] H.-S. Yoon and B.-J. Yi, "A 4-dof flexible continuum robot using a spring backbone," in *2009 International Conference on Mechatronics and Automation*, pp. 1249–1254, Aug 2009.

[21] G. Immega and K. Antonelli, "The ksi tentacle manipulator," in *Proceedings of 1995 IEEE International Conference on Robotics and Automation*, vol. 3, pp. 3149–3154 vol.3, May 1995.

[22] V. Falkenhahn, T. Mahl, A. Hildebrandt, R. Neumann, and O. Sawodny,

"Dynamic modeling of bellows-actuated continuum robots using the euler–lagrange formalism," *IEEE Transactions on Robotics*, vol. 31, no. 6, pp. 1483–1496, 2015.

[23] M. B. Pritts and C. D. Rahn, "Design of an artificial muscle continuum robot," in *Robotics and Automation, 2004. Proceedings. ICRA'04. 2004 IEEE International Conference on*, vol. 5, pp. 4742–4746, IEEE, 2004.

[24] K. Xu and N. Simaan, "An investigation of the intrinsic force sensing capabilities of continuum robots," *IEEE Transactions on Robotics*, vol. 24, no. 3, pp. 576–587, 2008.

[25] D. C. Rucker and R. J. Webster, "Deflection-based force sensing for continuum robots: A probabilistic approach," in *Intelligent Robots and Systems (IROS), 2011 IEEE/RSJ International Conference on*, pp. 3764–3769, IEEE, 2011.

[26] W. Wei and N. Simaan, "Modeling, Force Sensing, and Control of Flexible Cannulas for Microstent Delivery," *Journal of Dynamic Systems, Measurement, and Control*, vol. 134, no. 4, p. 041004, 2012.

[27] S. Hasanzadeh and F. Janabi-Sharifi, "Model-based Force Estimation for Intracardiac Catheters," *IEEE/ASME Transactions on Mechatronics*, vol. 21, no. 1, pp. 1–1, 2015.

[28] R. Xu, A. Yurkewich, and R. V. Patel, "Curvature, torsion, and force sensing in continuum robots using helically wrapped fbg sensors," *IEEE Robotics and Automation Letters*, vol. 1, no. 2, pp. 1052–1059, 2016.

[29] A. Bajo and N. Simaan, "Kinematics-based detection and localization of contacts along multisegment continuum robots," *IEEE Transactions on Robotics*, vol. 28, no. 2, pp. 291–302, 2012.

[30] Y. Chen, L. Wang, K. Galloway, I. Godage, N. Simaan, and E. Barth, "Modal-based kinematics and contact detection of soft robots," *Soft Robotics*, 2020.

[31] D. Hughes, J. Lammie, and N. Correll, "A robotic skin for collision avoidance and affective touch recognition," *IEEE Robotics and Automation Letters*, vol. 3, no. 3, pp. 1386–1393, 2018.

[32] M. Kaboli, D. Feng, K. Yao, P. Lanillos, and G. Cheng, "A tactile-based framework for active object learning and discrimination using multimodal robotic skin," *IEEE Robotics and Automation Letters*, vol. 2, no. 4, pp. 2143–2150, 2017.

[33] P. Mittendorfer and G. Cheng, "Humanoid multimodal tactile-sensing modules," *IEEE Transactions on robotics*, vol. 27, no. 3, pp. 401–410, 2011.

[34] R. Patel, R. Cox, and N. Correll, "Integrated proximity, contact and force sensing using elastomer-embedded commodity proximity sensors," *Autonomous Robots*, vol. 42, no. 7, pp. 1443–1458, 2018.

[35] M. Sohgawa, A. Nozawa, H. Yokoyama, T. Kanashima, M. Okuyama, T. Abe, H. Noma, and T. Azuma, "Multimodal measurement of proximity and touch force by light-and strain-sensitive multifunctional mems sensor," in *SENSORS, 2014 IEEE*, pp. 1749–1752, IEEE, 2014.

[36] "Stroke Facts | cdc.gov."

[37] F. O. Lima, K. L. Furie, G. S. Silva, M. H. Lev, É. C. S. Camargo, A. B. Singhal, G. J. Harris, E. F. Halpern, W. J. Koroshetz, W. S. Smith, and R. G. Nogueira, "Prognosis of Untreated Strokes Due to Anterior Circulation Proximal Intracranial Arterial Occlusions Detected by Use of Computed Tomography Angiography," *JAMA Neurology*, vol. 71, p. 151, feb 2014.

[38] M. Goyal, A. M. Demchuk, B. K. Menon, M. Eesa, J. L. Rempel, J. Thornton, D. Roy, T. G. Jovin, R. A. Willinsky, B. L. Sapkota, *et al.*, "Randomized Assessment of Rapid Endovascular Treatment of Ischemic Stroke," *New England Journal of Medicine*, vol. 372, pp. 1019–1030, mar 2015.

[39] O. A. Berkhemer, P. S. Fransen, D. Beumer, L. A. Van Den Berg, H. F. Lingsma, A. J. Yoo, W. J. Schonewille, J. A. Vos, P. J. Nederkoorn, M. J. Wermer, *et al.*, "A Randomized Trial of Intraarterial Treatment for Acute Ischemic Stroke," *New England Journal of Medicine*, vol. 372, pp. 11–20, jan 2015.

[40] J. L. Saver, M. Goyal, A. Bonafe, H.-C. Diener, E. I. Levy, V. M. Pereira, G. W. Albers, C. Cognard, D. J. Cohen, W. Hacke, *et al.*, "Stent-Retriever Thrombectomy after Intravenous t-PA vs. t-PA Alone in Stroke," *New England Journal of Medicine*, vol. 372, pp. 2285–2295, jun 2015.

[41] B. C. Campbell, P. J. Mitchell, T. J. Kleinig, H. M. Dewey, L. Churilov, N. Yassi, B. Yan, R. J. Dowling, M. W. Parsons, T. J. Oxley, *et al.*, "Endovascular Therapy for Ischemic Stroke with Perfusion-Imaging Selection," *New England Journal of Medicine*, vol. 372, pp. 1009–1018, mar 2015.

[42] T. G. Jovin, A. Chamorro, E. Cobo, M. A. de Miquel, C. A. Molina, A. Rovira, L. San Román, J. Serena, S. Abilleira, M. Ribó, *et al.*, "Thrombectomy within 8 Hours after Symptom Onset in Ischemic Stroke," *New England Journal of Medicine*, vol. 372, pp. 2296–2306, jun 2015.

[43] M. Goyal, B. K. Menon, W. H. van Zwam, D. W. Dippel, P. J. Mitchell, A. M. Demchuk, A. Dávalos, C. B. Majoie, A. van der Lugt, M. A. De Miquel, *et al.*, "Endovascular thrombectomy after large-vessel ischaemic stroke: a meta-analysis of individual patient data from five randomised trials," *The Lancet*, vol. 387, pp. 1723–1731, apr 2016.

[44] T. M. Dall, M. V. Storm, R. Chakrabarti, O. Drogan, C. M. Keran, P. D. Donofrio, V. W. Henderson, H. J. Kaminski, J. C. Stevens, and T. R. Vidic, "Supply and demand analysis of the current and future US neurology workforce," *Neurology*, vol. 81, no. 5, pp. 470–478, 2013.

[45] J. Yi, D. Zielinski, B. Ouyang, J. Conners, R. Dafer, and M. Chen, "Predictors of false-positive stroke thrombectomy transfers," *Journal of NeuroInterventional Surgery*, vol. 9, no. 9, pp. 834–836, 2017.

[46] S. Hussain, D. Fiorella, J. Mocco, A. Arthur, I. Linfante, G. Zipfel, H. Woo, D. Frei, R. Nogueira, and F. C. Albuquerque, "In defense of our patients," *Journal of NeuroInterventional Surgery*, vol. 9, pp. 525–526, jun 2017.

[47] J. Bonatti, G. Vetrovec, C. V. Riga, O. Wazni, and P. Stadler, "Robotic technology in cardiovascular medicine," *Nature Reviews Cardiology*, vol. 11, no. 5, pp. 266–275, 2014.

[48] Y. Fu, H. Liu, W. Huang, S. Wang, and Z. Liang, "Steerable catheters in minimally invasive vascular surgery," *The international journal of medical robotics + computer assisted surgery : MRCAS*, vol. 5, no. September, pp. 381–391, 2009.

[49] G. A. Antoniou, C. V. Riga, E. K. Mayer, J. W. Nicholas, C. D. Bicknell, U. Kingdom, N. J. Cheshire, and C. D. Bicknell, "Clinical applications of robotic technology in vascular and endovascular surgery," *Journal of Vascular Surgery*, vol. 53, no. 2, pp. 493–499, 2011.

[50] H. Rafii-Tari, C. J. Payne, and G.-Z. Yang, "Current and emerging robot-assisted endovascular catheterization technologies: a review.," *Annals of biomedical engineering*, vol. 42, no. 4, pp. 697–715, 2014.

[51] A. Ali, D. H. Plettenburg, and P. Breedveld, "Steerable Catheters in Cardiology: Classifying Steerability and Assessing Future Challenges," 2016.

[52] A. Da Costa, M. Ben H'Dech, C. Romeyer-Bouchard, L. Bisch, A. Gate-Martinet, M. Levallois, and K. Isaaz, "Remote-controlled magnetic pulmonary vein isolation using a new three-dimensional non-fluoroscopic navigation system: A single-centre prospective study," *Archives of Cardiovascular Diseases*, vol. 106, no. 8-9, pp. 423–432, 2013.

[53] W. Saliba, V. Y. Reddy, O. Wazni, J. E. Cummings, J. D. Burkhardt, M. Haissaguerre, J. Kautzner, P. Peichl, P. Neuzil, V. Schibgilla, *et al.*, "Atrial Fibrillation Ablation Using a Robotic Catheter Remote Control System. Initial Human Experience and Long-Term Follow-Up Results," *Journal of the American College of Cardiology*, vol. 51, no. 25, pp. 2407–2411, 2008.

[54] R. Bai, L. Di Biase, M. Valderrabano, F. Lorgat, H. Mlcochova, R. Tilz, U. Meyerfeldt, P. M. Hranitzky, O. Wazni, P. Kanagaratnam, *et al.*, "Worldwide experience with the robotic navigation system in catheter ablation of atrial fibrillation: Methodology, efficacy and safety," *Journal of Cardiovascular Electrophysiology*, vol. 23, no. 8, pp. 820–826, 2012.

[55] Z. Shaikh, M. Eilenberg, and T. Cohen, "The Amigo™ Remote Catheter System: From Concept to Bedside," *The Journal of Innovations in Cardiac Rhythm Management*, vol. 8, no. 8, pp. 2795–2802, 2017.

[56] D. Walters, J. Omran, M. Patel, R. Reeves, L. Ang, and E. Mahmud, "Robotic-Assisted Percutaneous Coronary Intervention: Concept, Data, and Clinical Application," 2019.

[57] T. Soyama, D. Yoshida, Y. Sakuhara, R. Morita, D. Abo, and K. Kudo, "The Steerable Microcatheter: A New Device for Selective Catheterisation," *CardioVascular and Interventional Radiology*, vol. 40, no. 6, pp. 947–952, 2017.

[58] A. D. Santa and D. D. Rossi, "Intravascular microcatheter steered by conducting

polymer actuators," *International Conference of the IEEE Engineering in Medicine and Biology Society*, pp. 2203–2204, 1996.

[59] T. Fukuda, Shuxiang Guo, K. Kosuge, F. Arai, M. Negoro, and K. Nakabayashi, "Micro active catheter system with multi degrees of freedom," pp. 2290–2295, 2002.

[60] W. Small IV, T. S. Wilson, P. R. Buckley, W. J. Benett, J. M. Loge, J. Hartman, and D. J. Maitland, "Prototype fabrication and preliminary In Vitro testing of a shape memory endovascular thrombectomy device," *IEEE Transactions on Biomedical Engineering*, vol. 54, no. 9, pp. 1657–1666, 2007.

[61] Y. Fu, A. Gao, H. Liu, K. Li, and Z. Liang, "Development of a novel robotic catheter system for endovascular minimally invasive surgery," in *2011 IEEE/ICME International Conference on Complex Medical Engineering, CME 2011*, pp. 400–405, IEEE, 2011.

[62] E. Ayvali and J. P. Desai, "Towards a discretely actuated steerable cannula," *Proceedings - IEEE International Conference on Robotics and Automation*, pp. 1614–1619, 2012.

[63] Y. Haga and T. Matsunaga, "Microsystems for minimally invasive medicine and healthcare," *2014 International Conference on Electronics Packaging, ICEP 2014*, pp. 353–356, 2014.

[64] N. Kim, S. Lee, W. Lee, and G. Jang, "Development of a magnetic catheter with rotating multi-magnets to achieve unclogging motions with enhanced steering capability," *AIP Advances*, vol. 8, no. 5, 2018.

[65] J. Janjic, F. Mastik, M. D. Leistikow, J. G. Bosch, G. Springeling, A. F. Van Der Steen, and G. Van Soest, "Sparse ultrasound image reconstruction from a shape-sensing single-element forward-looking catheter," *IEEE Transactions on Biomedical Engineering*, vol. 65, no. 10, pp. 2210–2218, 2018.

[66] Y. Chitalia, X. Wang, and J. P. Desai, "Design, Modeling and Control of a 2-DoF Robotic Guidewire," in *Proceedings - IEEE International Conference on Robotics and Automation*, pp. 32–37, IEEE, may 2018.

[67] G. Fagogenis, M. Mencattelli, Z. Machaidze, B. Rosa, K. Price, F. Wu, V. Weixler, M. Saeed, J. E. Mayer, and P. E. Dupont, "Autonomous robotic intracardiac catheter navigation using haptic vision," *Science Robotics*, vol. 4, no. 29, 2019.

[68] O. Nikoubashman, A. Nikoubashman, M. Büsen, and M. Wiesmann, "Necessary catheter diameters for mechanical thrombectomy with ADAPT," *American Journal of Neuroradiology*, vol. 38, no. 12, pp. 2277–2281, 2017.

[69] S. B. Kesner and R. D. Howe, "Position control of motion compensation cardiac catheters," *IEEE Transactions on Robotics*, vol. 27, no. 6, pp. 1045–1055, 2011.

[70] M. Khoshnam and R. V. Patel, "Estimating contact force for steerable ablation catheters based on shape analysis," *IEEE International Conference on Intelligent Robots and Systems*, pp. 3509–3514, sep 2014.

[71] S. Haldar, J. W. E. Jarman, S. Panikker, D. G. Jones, T. Salukhe, D. Gupta, G. Wynn, W. Hussain, V. Markides, and T. Wong, "Contact force sensing technology identifies sites of inadequate contact and reduces acute pulmonary vein reconnection: a prospective case control study.," *International journal of cardiology*, vol. 168, pp. 1160–6, sep 2013.

[72] E. R. Duncan, M. Finlay, S. P. Page, R. Hunter, F. Goromonzi, L. Richmond, V. Baker, M. Ginks, V. Ezzat, M. Dhinoja, M. J. Earley, S. Sporton, and R. J. Schilling, "Improved electrogram attenuation during ablation of paroxysmal atrial fibrillation with the Hansen robotic system.," *Pacing and clinical electrophysiology : PACE*, vol. 35, pp. 730–8, jun 2012.

[73] K.-H. Kuck, V. Y. Reddy, B. Schmidt, A. Natale, P. Neuzil, N. Saoudi, J. Kautzner, C. Herrera, G. Hindricks, P. Jaïs, *et al.*, "A novel radiofrequency ablation catheter using contact force sensing: Toccata study.," *Heart rhythm : the official journal of the Heart Rhythm Society*, vol. 9, pp. 18–23, jan 2012.

[74] M. Seelen, R. U. S. A. Data, and P. Classification, *United States c12) Patent Application Publication Figure 1*, vol. 111111. 2011.

[75] H. Liu, N. Kubota, X. Zhu, R. Dillmann, D. Zhou, and R. Goebel, *Intelligent Robotics and Applications*, vol. 9245 of *Lecture Notes in Computer Science*. Cham: Springer International Publishing, 2015.

[76] C. Poelma, "Ultrasound Imaging Velocimetry: a review," *Experiments in Fluids*, vol. 58, no. 1, pp. 1–28, 2017.

[77] S. J. Denardo, L. Talbot, V. K. Hargrave, A. R. Selfridge, T. A. Ports, and P. G. Yock, "Accuracy of Doppler catheter measurements: Effect of inhomogeneous beam power distribution on mean and peak velocity," *Journal of the American College of Cardiology*, vol. 29, no. 2, pp. 283–292, 1997.

[78] M. Cesari, C. Leeuwenburgh, F. Lauretani, G. Onder, S. Bandinelli, C. Maraldi, J. M. Guralnik, M. Pahor, and L. Ferrucci, "Experimental Studies with a 9 French Forward-Looking Intracardiac Imaging and Ablation Catheter," *American Journal of Clinical Nutrition*, vol. 83, no. 5, pp. 1142–1148, 2006.

[79] R. E. Goldman, A. Bajo, and N. Simaan, "Compliant motion control for multisegment continuum robots with actuation force sensing," *IEEE Transactions on Robotics*, vol. 30, no. 4, pp. 890–902, 2014.

[80] W. Kunz, M. Almekhlafi, B. Menon, J. Saver, D. Dippel, C. Majoie, T. Jovin, A. Davalos, S. Bracard, F. Guillemin, B. Campbell, P. Mitchell, P. White, K. Muir,

S. Brown, A. Demchuk, M. Hill, and M. Goyal, "Lifetime quality of life and cost consequences of treatment delays in endovascular thrombectomy for stroke based on hermes data," *Journal of NeuroInterventional Surgery*, vol. 10, pp. A1 LP – A2, jul 2018.

[81] O. O. Zaidat, A. C. Castonguay, I. Linfante, R. Gupta, C. O. Martin, W. E. Holloway, N. Mueller-Kronast, J. D. English, G. Dabus, T. W. Malisch, *et al.*, "First pass effect: A new measure for stroke thrombectomy devices," *Stroke*, vol. 49, no. 3, pp. 660–666, 2018.

[82] J. Vargas, A. M. Spiotta, K. Fargen, R. D. Turner, I. Chaudry, and A. Turk, "Experience with A Direct Aspiration First Pass Technique (ADAPT) for Thrombectomy in Distal Cerebral Artery Occlusions Causing Acute Ischemic Stroke," *World Neurosurgery*, vol. 99, pp. 31–36, 2017.

[83] J.-h. Baek, B. M. Kim, J. H. Heo, H. S. Nam, S. H. Kim, C. W. Ryu, Y.-k. Ihn, B. Kim, H.-j. Jeon, J. W. Kim, J. S. Byun, S. Suh, J. J. Park, W. J. Lee, J. Roh, and B.-s. Shin, "Number of Stent Retriever Passes Associated With Futile Recanalization in Acute Stroke," pp. 2088–2095, 2018.

[84] C. Shi, X. Luo, P. Qi, T. Li, S. Song, Z. Najdovski, T. Fukuda, and H. Ren, "Shape sensing techniques for continuum robots in minimally invasive surgery: A survey," *IEEE Transactions on Biomedical Engineering*, vol. 64, no. 8, pp. 1665–1678, 2017.

[85] J. Peirs, D. Reynaerts, H. Van Brussel, G. De Gersem, and H.-W. Tang, "Design of an advanced tool guiding system for robotic surgery," in *Robotics and Automation, 2003. Proceedings. ICRA'03. IEEE International Conference on*, vol. 2, pp. 2651–2656, IEEE, 2003.

[86] P. E. Dupont, J. Lock, B. Itkowitz, and E. Butler, "Design and control of concentric-tube robots," *IEEE Transactions on Robotics*, vol. 26, no. 2, pp. 209–225, 2010.

[87] J. Burgner, D. C. Rucker, H. B. Gilbert, P. J. Swaney, P. T. Russell, K. D. Weaver, and R. J. Webster, “A telerobotic system for transnasal surgery,” *IEEE/ASME Transactions on Mechatronics*, vol. 19, pp. 996–1006, June 2014.

[88] W. McMahan, V. Chitrakaran, M. Csencsits, D. Dawson, I. D. Walker, B. A. Jones, M. Pritts, D. Dienno, M. Grissom, and C. D. Rahn, “Field trials and testing of the octarm continuum manipulator,” in *Robotics and Automation, 2006. ICRA 2006. Proceedings 2006 IEEE International Conference on*, pp. 2336–2341, IEEE, 2006.

[89] I. Gravagne and I. Walker, “On the Kinematics of Remotely-Actuated Continuum Robots,” pp. 2544–2550, 2000.

[90] T. Hassan, M. Cianchetti, B. Mazzolai, C. Laschi, and P. Dario, “Active-braid, a bioinspired continuum manipulator,” *IEEE Robotics and Automation Letters*, vol. 2, no. 4, pp. 2104–2110, 2017.

[91] F. Maden, K. Korkmaz, and Y. Akgün, “A review of planar scissor structural mechanisms: geometric principles and design methods,” *Architectural Science Review*, vol. 54, no. 3, pp. 246–257, 2011.

[92] A. Baab, “Iris diaphragm with linear aperture scale,” Apr. 17 1973. US Patent 3,727,531.

[93] M. Gharib, “A new design for variable diameter orifice mechanism,” in *ASME 2012 International Mechanical Engineering Congress and Exposition*, pp. 1551–1552, American Society of Mechanical Engineers, 2012.

[94] W. Hermanns, “Variable diameter wheel,” Apr. 9 1974. US Patent 3,802,743.

[95] R. Roy, L. Wang, and N. Simaan, “Investigation of effects of dynamics on intrinsic wrench sensing in continuum robots,” in *Robotics and Automation (ICRA), 2016 IEEE International Conference on*, pp. 2052–2059, IEEE, 2016.

[96] N. Simaan, "Snake-like units using flexible backbones and actuation redundancy for enhanced miniaturization," in *Robotics and Automation, 2005. ICRA 2005. Proceedings of the 2005 IEEE International Conference on*, pp. 3012–3017, IEEE, 2005.

[97] R. E. Goldman, A. Bajo, and N. Simaan, "Compliant Motion Control for Multisegment Continuum Robots With Actuation Force Sensing," *IEEE Transactions on Robotics*, vol. 30, pp. 890–902, Aug. 2014.

[98] G. Del Giudice, N. Sarli, S. D. Herrell, and N. Simaan, "Design considerations for continuum robot actuation units enabling dexterous transurethral bladder cancer resection," in *ASME 2016 International Design Engineering Technical Conferences and Computers and Information in Engineering Conference*, pp. V05AT07A030–V05AT07A030, American Society of Mechanical Engineers, 2016.

[99] H. Zghal, R. Dubey, and J. Euler, "Efficient gradient projection optimization for manipulators with multiple degrees of redundancy," in *Robotics and Automation, 1990. Proceedings., 1990 IEEE International Conference on*, pp. 1006–1011, IEEE, 1990.

[100] K. Xu and N. Simaan, "Intrinsic wrench estimation and its performance index for multisegment continuum robots," *IEEE Transactions on Robotics*, vol. 26, no. 3, pp. 555–561, 2010.

[101] M. Zinn, O. Khatib, B. Roth, and J. K. Salisbury, "Playing it safe [human-friendly robots]," *IEEE Robotics & Automation Magazine*, vol. 11, no. 2, pp. 12–21, 2004.

[102] A. De Luca, A. Albu-Schaffer, S. Haddadin, and G. Hirzinger, "Collision detection and safe reaction with the dlr-iii lightweight manipulator arm," in *2006 IEEE/RSJ International Conference on Intelligent Robots and Systems*, pp. 1623–1630, IEEE, 2006.

[103] R. Bloss, "Collaborative robots are rapidly providing major improvements in productivity, safety, programing ease, portability and cost while addressing many new applications," *Industrial Robot: An International Journal*, vol. 43, no. 5, pp. 463–468, 2016.

[104] R. Yasin and N. Simaan, "Joint-level force sensing for indirect hybrid force/position control of continuum robots with friction," *The International Journal of Robotics Research*, vol. 40, no. 4-5, pp. 764–781, 2021.

[105] H. Donat, S. Lilge, J. Burgner-Kahrs, and J. J. Steil, "Estimating Tip Contact Forces for Concentric Tube Continuum Robots Based on Backbone Deflection," *IEEE Transactions on Medical Robotics and Bionics*, vol. 2, pp. 619–630, oct 2020.

[106] F. Khan, R. J. Roesthuis, and S. Misra, "Force sensing in continuum manipulators using fiber Bragg grating sensors," in *IEEE International Conference on Intelligent Robots and Systems*, vol. 2017-September, pp. 2531–2536, Institute of Electrical and Electronics Engineers Inc., dec 2017.

[107] Z. Wu, A. Gao, N. Liu, Z. Jin, and G. Z. Yang, "FBG-Based Triaxial Force Sensor Integrated with an Eccentrically Configured Imaging Probe for Endoluminal Optical Biopsy," in *Proceedings - IEEE International Conference on Robotics and Automation*, pp. 1625–1631, Institute of Electrical and Electronics Engineers Inc., may 2020.

[108] R. E. Goldman, A. Bajo, and N. Simaan, "Compliant motion control for continuum robots with intrinsic actuation sensing," in *2011 IEEE International Conference on Robotics and Automation*, (Shanghai, China), pp. 1126–1132, IEEE, may 2011.

[109] D. Silvera-Tawil, D. Rye, and M. Velonaki, "Artificial skin and tactile sensing for socially interactive robots: A review," *Robotics and Autonomous Systems*, vol. 63, pp. 230–243, 2015.

[110] Z. Kappassov, J.-A. Corrales, and V. Perdereau, “Tactile sensing in dexterous robot hands,” *Robotics and Autonomous Systems*, vol. 74, pp. 195–220, 2015.

[111] Y. Yamada, T. Morizono, Y. Umetani, and H. Takahashi, “Highly soft viscoelastic robot skin with a contact object-location-sensing capability,” *IEEE Transactions on Industrial electronics*, vol. 52, no. 4, pp. 960–968, 2005.

[112] Y. Ding and U. Thomas, “Collision avoidance with proximity servoing for redundant serial robot manipulators,” in *2020 IEEE International Conference on Robotics and Automation (ICRA)*, pp. 10249–10255, 2020.

[113] I. A. Gravagne and I. D. Walker, “Kinematic transformations for remotely-actuated planar continuum robots,” in *Robotics and Automation, 2000. Proceedings. ICRA’00. IEEE International Conference on*, vol. 1, pp. 19–26, IEEE, 2000.

[114] N. Simaan, K. Xu, W. Wei, A. Kapoor, P. Kazanzides, R. Taylor, and P. Flint, “Design and integration of a telerobotic system for minimally invasive surgery of the throat,” *The International journal of robotics research*, vol. 28, no. 9, pp. 1134–1153, 2009.

[115] T. Paulino, P. Ribeiro, M. Neto, S. Cardoso, A. Schmitz, J. Santos-Victor, A. Bernardino, and L. Jamone, “Low-cost 3-axis soft tactile sensors for the human-friendly robot vizzy,” in *Robotics and Automation (ICRA), 2017 IEEE International Conference on*, pp. 966–971, IEEE, 2017.

[116] R. H. Bishop, “The Mechatronics Handbook, Second Edition - 2 Volume Set,” in *The Mechatronics Handbook, Second Edition - 2 Volume Set*, pp. 18–3, CRC Press, feb 2002.

[117] J. Ding, R. E. Goldman, K. Xu, P. K. Allen, D. L. Fowler, and N. Simaan, “Design and coordination kinematics of an insertable robotic effectors platform for single-

port access surgery," *IEEE/ASME transactions on mechatronics*, vol. 18, no. 5, pp. 1612–1624, 2013.

[118] P. Papanagiotou and C. J. White, "Endovascular reperfusion strategies for acute stroke," *JACC: Cardiovascular Interventions*, vol. 9, no. 4, pp. 307–317, 2016.

[119] E. J. Benjamin, M. J. Blaha, S. E. Chiuve, M. Cushman, S. R. Das, R. Deo, S. D. De Ferranti, J. Floyd, M. Fornage, C. Gillespie, *et al.*, *Heart Disease and Stroke Statistics'2017 Update: A Report from the American Heart Association*, vol. 135. 2017.

[120] A. T. Rai, A. E. Seldon, S. Boo, P. S. Link, J. R. Domico, A. R. Tarabishy, N. Lucke-Wold, and J. S. Carpenter, "A population-based incidence of acute large vessel occlusions and thrombectomy eligible patients indicates significant potential for growth of endovascular stroke therapy in the USA," *Journal of NeuroInterventional Surgery*, vol. 9, no. 8, pp. 722–726, 2017.

[121] S. Rajsic, H. Gothe, H. H. Borba, G. Sroczynski, J. Vujicic, T. Toell, and U. Siebert, "Economic burden of stroke: a systematic review on post-stroke care," *The European Journal of Health Economics*, vol. 20, pp. 107–134, feb 2019.

[122] S. Seabury, K. Bognar, Y. Xu, C. Huber, S. R. Commerford, and D. Tayama, "Regional disparities in the quality of stroke care," *American Journal of Emergency Medicine*, vol. 35, no. 9, pp. 1234–1239, 2017.

[123] L. N. Hopkins and D. R. Holmes, "Public Health Urgency Created by the Success of Mechanical Thrombectomy Studies in Stroke," *Circulation*, vol. 135, no. 13, pp. 1188–1190, 2017.

[124] D. R. Holmes and L. N. Hopkins, "Interventional Cardiology and Acute Stroke Care Going Forward: JACC Review Topic of the Week," *Journal of the American College of Cardiology*, vol. 73, no. 12, pp. 1483–1490, 2019.

[125] J. Aldstadt, M. Waqas, M. Yasumiishi, M. Mokin, V. M. Tuinto, H. H. Rai, F. Chin, B. R. Levy, A. T. Rai, J. Mocco, K. V. Snyder, J. M. Davies, E. I. Levy, and A. H. Siddiqui, "Mapping access to endovascular stroke care in the USA and implications for transport models," *Journal of NeuroInterventional Surgery*, 2021.

[126] L. Cercenelli, B. Bortolani, and E. Marcelli, "CathROB: A Highly Compact and Versatile Remote Catheter Navigation System," *Applied Bionics and Biomechanics*, vol. 2017, pp. 1–13, 2017.

[127] M. N. Faddis, J. Chen, J. Osborn, M. Talcott, M. E. Cain, and B. D. Lindsay, "Magnetic Guidance System for Cardiac Electrophysiology: A Prospective Trial of Safety and Efficacy in Humans," *Journal of the American College of Cardiology*, vol. 42, no. 11, pp. 1952–1958, 2003.

[128] G. Nölker, K. J. Gutleben, B. Muntean, J. Vogt, D. Horstkotte, L. Dabiri Abkenari, F. Akca, and T. Szili-Torok, "Novel robotic catheter manipulation system integrated with remote magnetic navigation for fully remote ablation of atrial tachyarrhythmias: A two-centre evaluation," *Europace*, vol. 14, no. 12, pp. 1715–1718, 2012.

[129] W. Saliba, J. E. Cummings, S. Oh, Y. Zhang, T. N. Mazgalev, R. A. Schweikert, J. D. Burkhardt, and A. Natale, "Novel Robotic Catheter Remote Control System : Feasibility and Safety of Transseptal Puncture and Endocardial Catheter Navigation," *Journal of Cardiovascular Electrophysiology*, vol. 17, pp. 1102–1105, 2006.

[130] C. Del Giudice, O. Pellerin, M. Nouri Neville, G. Amouyal, I. Fitton, C. Leré-Déan, and M. Sapoval, "Comparison of Two Endovascular Steerable Robotic Catheters for Percutaneous Robot-Assisted Fibroid Embolization," *CardioVascular and Interventional Radiology*, vol. 41, no. 3, pp. 483–488, 2018.

[131] S. Owji, T. Lu, T. M. Loh, A. Schwein, A. B. Lumsden, and J. Bismuth, "Robotic-

Assisted Inferior Vena Cava Filter Retrieval," *Methodist DeBakey Cardiovascular Journal*, vol. 13, no. 1, pp. 34–36, 2017.

[132] A. H. Perera, C. V. Riga, L. Monzon, R. G. Gibbs, C. D. Bicknell, and M. Hamady, "Robotic Arch Catheter Placement Reduces Cerebral Embolization During Thoracic Endovascular Aortic Repair (TEVAR)," *European Journal of Vascular and Endovascular Surgery*, vol. 53, no. 3, pp. 362–369, 2017.

[133] C. V. Riga, C. D. Bicknell, A. Rolls, N. J. Cheshire, and M. S. Hamady, "Robot-assisted fenestrated endovascular aneurysm repair (FEVAR) using the magellan system," *Journal of Vascular and Interventional Radiology*, vol. 24, no. 2, pp. 191–196, 2013.

[134] S. M. Vuong, C. P. Carroll, R. D. Tackla, W. J. Jeong, and A. J. Ringer, "Application of emerging technologies to improve access to ischemic stroke care | Neurosurgical Focus," *Neurosurgical Focus*, vol. 42, no. April, p. E8, 2017.

[135] I. D. Walker, "Continuous Backbone "Continuum" Robot Manipulators," *ISRN Robotics*, vol. 2013, pp. 1–19, 2013.

[136] R. Beyar, L. Gruberg, D. Deleanu, A. Roguin, Y. Almagor, S. Cohen, G. Kumar, and T. Wenderow, "Remote-control percutaneous coronary interventions: Concept, validation, and first-in-humans pilot clinical trial," *Journal of the American College of Cardiology*, vol. 47, no. 2, pp. 296–300, 2006.

[137] V. M. Pereira, N. M. Cancelliere, P. Nicholson, I. Radovanovic, K. E. Drake, J. M. Sungur, T. Krings, and A. Turk, "First-in-human, robotic-assisted neuroendovascular intervention," *Journal of NeuroInterventional Surgery*, vol. 12, pp. 338–340, apr 2020.

[138] R. G. Nogueira, R. Sachdeva, A. R. Al-Bayati, M. H. Mohammaden, M. R. Frankel, and D. C. Haussen, "Robotic assisted carotid artery stenting for the treatment of

symptomatic carotid disease: Technical feasibility and preliminary results," *Journal of NeuroInterventional Surgery*, vol. 12, no. 4, pp. 341–344, 2020.

[139] K. C. Sajja, A. Sweid, F. Al Saiegh, N. Chalouhi, M. B. Avery, R. F. Schmidt, S. I. Tjoumakaris, M. R. Gooch, N. Herial, R. Abbas, H. Zarzour, V. Romo, R. Rosenwasser, and P. Jabbour, "Endovascular robotic: Feasibility and proof of principle for diagnostic cerebral angiography and carotid artery stenting," *Journal of NeuroInterventional Surgery*, vol. 12, no. 4, pp. 345–349, 2020.

[140] J. B. Hinrichs, S. Marquardt, F. K. Wacker, and B. C. Meyer, "Coil embolization of reversed-curve hepatointestinal collaterals in radioembolization: potential solutions for a challenging task," *Radiology Case Reports*, vol. 12, no. 3, pp. 529–533, 2017.

[141] J. T. Martin, P. C. Hulsberg, E. Soule, M. Shabandi, and J. Matteo, "Welcome to the New Era: A Completely Wireless Interventional Procedure," *Cureus*, vol. 10, no. 9, 2018.

[142] Y. Nishihara, "Embolization of post-EVAR type II endoleaks," vol. 2.

[143] S. Jeon, A. K. Hoshiar, K. Kim, S. Lee, E. Kim, S. Lee, J.-y. Kim, B. J. Nelson, H.-J. Cha, B.-J. Yi, *et al.*, "A magnetically controlled soft microrobot steering a guidewire in a three-dimensional phantom vascular network," *Soft robotics*, vol. 6, no. 1, pp. 54–68, 2019.

[144] T. Gopesh, J. H. Wen, D. Santiago-Dieppa, B. Yan, J. S. Pannell, A. Khalessi, A. Norbash, and J. Friend, "Soft robotic steerable microcatheter for the endovascular treatment of cerebral disorders," *Science Robotics*, vol. 6, no. 57, p. eabf0601, 2021.

[145] S. Jeong, Y. Chitalia, and J. P. Desai, "Design, modeling, and control of a coaxially aligned steerable (coast) guidewire robot," *IEEE Robotics and Automation Letters*, vol. 5, no. 3, pp. 4947–4954, 2020.

[146] A. Sarma, G. C. Collins, N. Nayar, Y. Chitalia, S. Jeong, B. D. Lindsey, and J. P. Desai, "Towards the development of an ultrasound-guided robotically steerable guidewire," in *2020 International Symposium on Medical Robotics (ISMR)*, pp. 173–180, IEEE, 2020.

[147] K. Oliver-Butler, Z. H. Epps, and D. C. Rucker, "Concentric agonist-antagonist robots for minimally invasive surgeries," in *Transportation Research Procedia* (R. J. Webster and B. Fei, eds.), vol. 25, p. 1013511, mar 2017.

[148] J. W. Burdick, "A Modal Approach to Hyper-Redundant Manipulator Kinematics," *IEEE Transactions on Robotics and Automation*, vol. 10, no. 3, pp. 343–354, 1994.

[149] J. Zhang, K. Xu, N. Simaan, and S. Manolidis, "A pilot study of robot-assisted cochlear implant surgery using steerable electrode arrays.," *Medical image computing and computer-assisted intervention : MICCAI ... International Conference on Medical Image Computing and Computer-Assisted Intervention*, vol. 9, pp. 33–40, jan 2006.

[150] J. Brewer, "Kronecker products and matrix calculus in system theory," *IEEE Transactions on circuits and systems*, vol. 25, no. 9, pp. 772–781, 1978.

[151] R. E. Kalman, "A new approach to linear filtering and prediction problems," *Journal of Fluids Engineering, Transactions of the ASME*, vol. 82, pp. 35–45, mar 1960.

[152] R. A. Srivatsan, G. T. Rosen, D. F. N. Mohamed, and H. Choset, "Estimating SE(3) elements using a dual quaternion based linear Kalman filter," *Robotics: Science and Systems {XII}.*, vol. 10., 2016.

[153] X. Pennec and J.-p. Thirion, "A Framework for Uncertainty and Validation of 3-D Registration Methods based on Points and Frames," *International Journal of Computer Vision*, vol. 25, no. 3, pp. 203–229, 1997.

[154] M. H. Moghari and P. Abolmaesumi, “Point-based rigid-body registration using an unscented Kalman filter,” *IEEE Transactions on Medical Imaging*, vol. 26, no. 12, pp. 1708–1728, 2007.

[155] D. M. Rosen, L. Carlone, A. S. Bandeira, and J. J. Leonard, “SE-Sync: A certifiably correct algorithm for synchronization over the special Euclidean group,” *International Journal of Robotics Research*, vol. 38, no. 2-3, pp. 95–125, 2019.

[156] R. Arun Srivatsan, M. Xu, N. Zevallos, and H. Choset, “Probabilistic pose estimation using a Bingham distribution-based linear filter,” *International Journal of Robotics Research*, vol. 37, no. 13-14, pp. 1610–1631, 2018.

[157] A. Dore, G. Smoljkic, E. V. Poorten, M. Sette, J. V. Sloten, and G. Z. Yang, “Catheter navigation based on probabilistic fusion of electromagnetic tracking and physically-based simulation,” *IEEE International Conference on Intelligent Robots and Systems*, pp. 3806–3811, 2012.

[158] A. Hong, A. J. Petruska, and B. J. Nelson, “Tracking a magnetically guided catheter with a single rotating C-Arm,” *Proceedings - IEEE International Conference on Robotics and Automation*, vol. 2015-June, no. June, pp. 618–623, 2015.

[159] X. Wu, J. Housden, Y. Ma, B. Razavi, K. Rhode, and D. Rueckert, “Fast catheter segmentation from echocardiographic sequences based on segmentation from corresponding X-ray fluoroscopy for cardiac catheterization interventions,” *IEEE Transactions on Medical Imaging*, vol. 34, no. 4, pp. 861–876, 2015.

[160] A. Denasi, F. Khan, K. J. Boskma, M. Kaya, C. Hennersperger, R. Gobl, M. Tirindelli, N. Navab, and S. Misra, “An Observer-Based Fusion Method Using Multicore Optical Shape Sensors and Ultrasound Images for Magnetically-Actuated Catheters,” *Proceedings - IEEE International Conference on Robotics and Automation*, pp. 50–57, 2018.

[161] Y. Xiang, H. Shen, L. Xie, and H. Wang, “Master-Slave Guidewire and Catheter Robotic System for Cardiovascular Intervention,” *2019 28th IEEE International Conference on Robot and Human Interactive Communication, RO-MAN 2019*, pp. 1–6, 2019.

[162] P. M. Loschak, A. Degirmenci, and R. D. Howe, “Predictive filtering in motion compensation with steerable cardiac catheters,” in *2017 IEEE International Conference on Robotics and Automation (ICRA)*, vol. 118, pp. 4830–4836, IEEE, may 2017.

[163] D. J. DePriest and J. M. Mendel, “Lessons in Digital Estimation Theory,” *Technometrics*, vol. 30, no. 1, p. 128, 1988.

[164] H. Durrant-Whyte, “Introduction to estimation and the Kalman filter,” *Australian Centre for Field Robotics*, 2001.

[165] R. Manish, “Linear and Non-linear Estimation Techniques: Theory and Comparison,” pp. 1–17, 2014.

[166] A. W. A. W. Nutbourne and R. R. R. R. Martin, *Differential geometry applied to curve and surface design*. E. Horwood, 1988.

[167] M. T. Froehler, “Comparison of Vacuum Pressures and Forces Generated by Different Catheters and Pumps for Aspiration Thrombectomy in Acute Ischemic Stroke,” *Interventional Neurology*, vol. 6, no. 3-4, pp. 199–206, 2017.

[168] T. D. Long, D. F. Kallmes, R. Hanel, T. Shigematsu, A. M. Halaszyn, J. Wolter, and A. Berenstein, “Novel aspiration catheter design for acute stroke thrombectomy,” *Journal of NeuroInterventional Surgery*, vol. 11, no. 2, pp. 179–183, 2019.

[169] S. Johnson, S. Duffy, G. Gunning, M. Gilvarry, J. P. McGarry, and P. E. McHugh, “Review of Mechanical Testing and Modelling of Thrombus Material for Vascular

Implant and Device Design," *Annals of Biomedical Engineering*, vol. 45, no. 11, pp. 2494–2508, 2017.

[170] C. Roffe, C. Tennuci, G. Pearce, J. Wong, S. Nayak, T. Jones, and F. Lally, "Comparison of the effectiveness of three methods of recanalization in a model of the middle cerebral artery: Thrombus aspiration via a 4F catheter, thrombus aspiration via the gp thromboaspiration device, and mechanical thrombectomy using the solitaire th," *Stroke Research and Treatment*, vol. 2011, 2011.

[171] S. Soize, L. Pierot, M. Mirza, G. Gunning, M. Gilvarry, M. Gawlitza, D. Vivien, M. Zuber, and E. Touzé, "Fast stent retrieval improves recanalization rates of thrombectomy: Experimental study on different thrombi," *American Journal of Neuroradiology*, vol. 41, no. 6, pp. 1049–1053, 2020.